DEPARTAMENTO DE ASTROFÍSICA

Universidad de La Laguna

GROWTH OF MASSIVE GALAXIES THROUGH COSMIC TIME

EL CRECIMIENTO DE LAS GALAXIAS MASIVAS CON EL TIEMPO COSMOLÓGICO

Thesis submitted by
Luis Peralta de Arriba
as a requirement for the degree of
Doctor by University of La Laguna

INSTITUTO Ð ASTROFÍSICA Ð CANARIAS
July 2016

Examination date: 27th July 2016
Thesis supervisors: Dr. Marc Balcells Comas & Dr. Ignacio Trujillo Cabrera

Some of the material included in this document has already been published in *Monthly Notices of the Royal Astronomical Society.*

A mi familia

Resumen
(Abstract in Spanish)

El descubrimiento de que las galaxias masivas son en promedio más compactas en el universo primitivo ha puesto de relieve la importancia de los procesos de crecimiento en tamaño de las galaxias con el tiempo cosmológico. Conocer mejor las características de estos objetos compactos dará claves para entender la naturaleza del mecanismo que hace crecer en tamaño a las galaxias masivas.

En la primera parte de esta tesis comenzamos investigando la discrepancia entre las masas dinámicas y estelares en las galaxias masivas compactas de tipo temprano. Para ello obtuvimos dispersiones de velocidades en distintos desplazamiento al rojo, usando nuestras propias observaciones con el telescopio GTC, así como espectros apilados de un cartografiado público realizado con el telescopio Keck II. Nuestros hallazgos indican que esta discrepancia escala con la compacidad de las galaxias, pero no encontramos correlación con el desplazamiento al rojo. Estos resultados nos conducen a interpretar la discrepancia entre estos dos estimadores de masa como una violación de la hipótesis de homología que se asume en el cálculo de las masas dinámicas, es decir, las galaxias masivas compactas no serían objetos auto-semejantes a las galaxias masivas de tamaños normales.

El siguiente paso de nuestra investigación fue averiguar cuáles son las restricciones que se pueden derivar para los mecanismos evolutivos de las galaxias masivas a partir de esta no-homología. Encontramos que las galaxias trazan un plano en el espacio masa estelar–radio efectivo–dispersión de velocidades, analizando las restricciones que esto implica sobre un mecanismo genérico. Además comprobamos que estas restricciones son compatibles con las simulaciones numéricas de galaxias que crecen a través de fusiones.

La última cuestión que abordamos es cuál es el mejor entorno para buscar galaxias reliquias, es decir, galaxias viejas que no han experimentado la evolución en tamaño. Encontramos que estas galaxias prefieren vivir en entornos densos. Comparando nuestros resultados observacionales con simulaciones, obtenemos un acuerdo entre ambos.

La manera más popular de explicar el crecimiento de las galaxias masivas es mediante la acreción de galaxias satélite a través de fusiones. La conclusión global de esta tesis es que todos nuestros resultados son compatibles con este mecanismo.

Códigos UNESCO: 2101.04, 2103.03.

Abstract

The discovery that massive galaxies are on average more compact in the primitive Universe has shown the importance of the mechanisms which are growing galaxies in size with cosmic time. A better understanding of the characteristics of these compact objects will give us clues about the nature of the mechanism which is contributing to the growth of massive galaxies.

In the first part of this thesis we investigated the discrepancy between dynamical and stellar masses in massive compact early-type galaxies. We obtained velocity dispersions at different redshifts using our own observations with the GTC telescope as well as stacked spectra from a public survey built with the Keck II telescope. Our findings indicate that this discrepancy scales with galaxy compactness, but it does not correlate with redshift. These results lead us to interpret the discrepancy between these two mass estimators as a violation of the homology hypothesis assumed in the computation of dynamical masses, i.e. massive compact galaxies are not self-similar objects to normal-sized massive galaxies.

The next step of our research was to guess what constraints on the evolutionary mechanisms of massive galaxies are implied by this non-homology. We find that galaxies populate a plane in the stellar mass–effective radius–velocity dispersion space, and we analyse the constraints that it means on a generic mechanism. Furthermore, we check that these constraints are compatible with simulations of the growth of early-type massive galaxies due to mergers.

Finally we addressed the question of which is the best environment for looking for relic galaxies, i.e. old galaxies which have not suffered the size evolution. We find that they prefer dense environments. Comparing our observational results with simulations, we obtain an agreement between both.

The most popular way to explain growth of massive galaxies is the accretion of galaxy satellites through mergers. The global conclusion of this thesis is that all our results are compatible with this mechanism.

UNESCO CODES: 2101.04, 2103.03.

Contents

List of figures

List of tables

1

Introduction

The existence of ‘island universes’ outside the Milky Way was established in the 1920s. In 1920, whether the so-called spiral nebulae were galaxies external to our own or gas clouds inside the Milky Way was highly controversial (see the so-called ‘Great Debate’; Shapley & Curtis 1921). A few years later, the discovery of Cepheid stars in M31 and M33 (Hubble 1925) clarified the external nature of these nebulae and may be considered the starting point of extragalactic astronomy.

Nowadays, these nebulae are called galaxies. With this term we refer to stellar aggregates of 10^4 to 10^{12} solar masses ($M_\odot$) which are kept together by the gravitational attraction of their constituents.

After nearly a century of study, our knowledge has progressed notably, thanks to an interplay of observational, theoretical and computational work. However, understanding galaxy formation and evolution remains a central unsolved question of modern astronomy.

In this thesis, we will address diagnostics obtained from the study of early-type massive galaxies from an observational point of view.

1.1 Galaxy morphologies

Taking into account the visual aspect of many galaxies, Hubble (1926, 1936) proposed to classify them into several types according to their morphology when they are observed in optical wavelengths. Subsequently, this classification has been refined with contributions from many authors (e.g. de Vaucouleurs 1959a). In Fig. 1.1, we show a modern version of the classification developed by Hubble (1936).

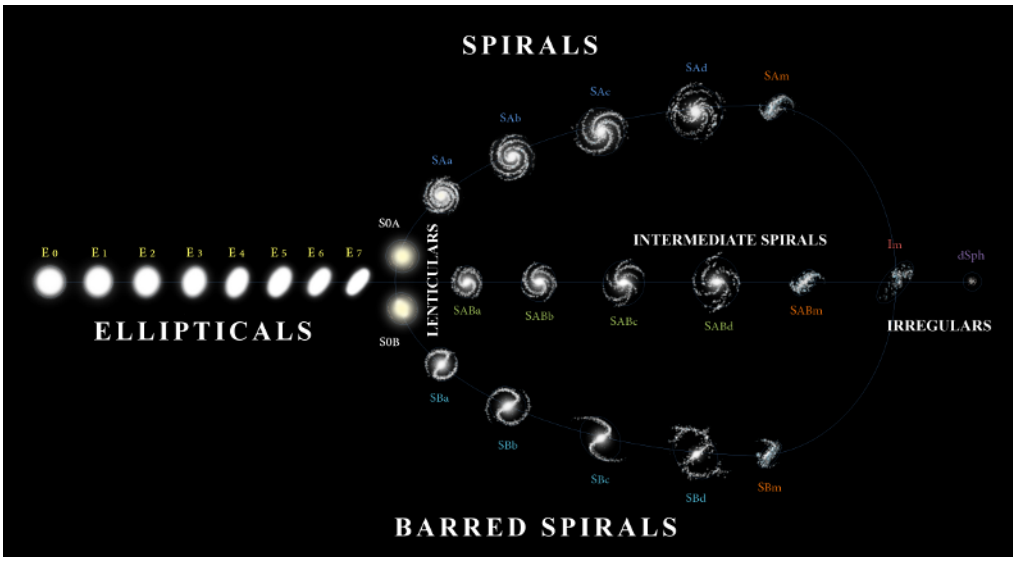

Figure 1.1. Tuning-fork-style diagram of the Hubble sequence. *Figure based on an image by Antonio Ciccolella and publicly available at* `https://commons.wikimedia.org/wiki/File:Hubble-Vaucouleurs.png` *under a license Creative Commons BY-SA 3.0.*

The first group of this classification would be the galaxies with elliptical shapes, which Hubble subclassified according to their ellipticities. The second group includes galaxies with spiral arms, which Hubble subclassified according to the opening of the spiral pattern and the prominence of the central light concentration (‘the bulge’). The third group contains a bar as well as spiral arms. Finally, a fourth class encompasses galaxies with irregular shapes.

Hubble thought that galaxies evolve through the diagram shown in Fig. 1.1 from left to right: they begin as ellipticals and end up being spirals (with or without bars). Consequently, Hubble named elliptical galaxies as early-type galaxies (ETGs), and spiral galaxies as late-type galaxies (LTGs). Although nowadays we know that galaxy evolution does not proceed this way, this nomenclature continues to be used.

1.2 Observational physical parameters of galaxies

In the following subsections we review the most relevant physical parameters that can be inferred from observations.

1.2.1 Mass

There are several methods with plenty of different details for estimating galaxy masses. We classify them into three groups according to the physical phenomena on which they are based:

- *Based on the amount of light that galaxy stars radiate.* From the stellar evolution theory, nowadays we know that the spectrum of a given star will be mainly determined by three properties: its mass, age and metallicity (e.g. Eddington 1926; Salaris & Cassisi 2006). In addition, from our surrounding environment (where individual stars can be identified), it has been reported that the distribution of masses in a star formation episode follows a specific functional form, referred to as the initial mass function (hereinafter IMF; e.g. Salpeter 1955; Kroupa 2002; Chabrier 2003). Making assumptions about the star formation history, IMF, metallicity and some other factors (for example, dust attenuation) of one galaxy, it is possible to fit its observed spectral energy distribution to a stellar population model and to give an estimate of the baryonic mass locked in stars (referred to as the galaxy's stellar mass).
- *Based on the movement of the stars.* Doppler shifts and Doppler broadening of spectral lines (Doppler & Studnica 1903) in the spectrum emitted by a galaxy provide information about motions along the line of sight (LOS). Such motions can be analysed to infer the mass which creates the gravitational potential where the stars are moving (e.g. Schwarzschild 1979; Satoh 1980). This mass is referred to as the dynamical mass, and includes all of its gravitational components (stars, dark matter, gas...).
- *Based on gravitational lensing.* When light passes through a gravitational potential well, it will experience a bending (c.f. Will 1988; Valls-Gabaud 2006). This gives the chance for observational astronomers to study the light from background sources in the LOS as a clue for estimating the mass of a galaxy. Obviously, this technique requires the existence of background sources, and consequently it cannot be employed in any galaxy.

The review by Courteau et al. (2014) gives a good account of the state-of-the-art techniques for measuring galaxy masses.

1.2.2 Size

For the layman, measuring the size of a galaxy could be seen as a straightforward process: measure the angular size of the galaxy in the sky, and then convert it to a physical size based on the distance from the galaxy to us.

However, many details have to be considered before measuring galaxy sizes. The most important one is to consider that galaxies do not finish abruptly. Their light profiles decrease asymptotically (e.g. Reynolds 1913; Hubble 1930), so a criterion of associating a size scale to the observed objects is necessary.

Due to this, a standard solution is to fit the data of the observed image with a light profile model (e.g. de Vaucouleurs 1948; Sérsic 1968), and then take as a size estimator the radius which contains half of the light of the considered model (called effective radius).

Another popular way is to estimate the Petrosian radius (Petrosian 1976). This radius is defined as the radius where the mean surface brightness within a radius is equal to the average of the local surface brightness along an annulus of the same radius multiplied by a constant factor.

The lack of atmospheric blurring in images from space-borne telescopes, such as the *Hubble Space Telescope*, makes them essential for size determination in galaxies with angular sizes of 1 arcsec such as high-redshift galaxies (e.g. van der Wel et al. 2014). For nearby, large-angular size galaxies, a sufficiently-large field of view is essential for the critical task of measuring the sky brightness background level.

1.2.3 Light profile shape

Light profiles of galaxies (the variation of surface brightness with projected distance from the galaxy centre) show a variety of shapes, ranging from shallow to strongly cuspy.

One procedure for measuring profile shapes is to compute a concentration index, i.e. the ratio between two radii which contain fixed fractions of the asymptotic total galaxy luminosity (e.g. Fraser 1972; de Vaucouleurs 1977).

Another procedure is to fit the galaxy light profile with a Sérsic model (Sérsic 1963; Sérsic 1968), characterising the intensity I as a function of the distance to the centre of the galaxy R with the equation

$$I(R) \propto \mathrm{e}^{-kR^{\frac{1}{n}}}, \tag{1.1}$$

where k and n are parameters to be determined. The last one (n) is named as the Sérsic index.

Both procedures are specially useful because they correlate with galaxy morphological types (e.g. Fraser 1972; Ravindranath et al. 2004). For example, for Sérsic indices $n = 1$ the Sérsic model reproduces the exponential profiles that late-type galaxies usually have (e.g. Patterson 1940; de Vaucouleurs 1959b).

Analogously, $n = 4$ leads to a de Vaucouleurs profile, which usually fits the light profiles of elliptical galaxies (e.g. de Vaucouleurs 1948, 1953).

1.2.4 Environment

Galaxies can be found either isolated or grouped in the Universe. In the first case astronomers say that they live in the field, while in the second case different names are used depending on the number of neighbours which belong to the group; below one hundred members, these sets are named galaxy groups, but we refer them as galaxy clusters when the number of members are typically hundreds or thousands (e.g. Abell 1958; Abell et al. 1989).

Most of the galaxies in the Universe do not live in rich clusters (e.g. Dekel & Ostriker 1999; Cebrián & Trujillo 2014). Also, depending on the environment that we are observing, we will find a higher fraction of elliptical or spiral galaxies (i.e. morphology–density relationship; Dressler 1980).

1.2.5 Internal dynamics

Thanks to the Doppler effect (Doppler & Studnica 1903) detected in the galaxy spectra, it is possible to measure some characteristics of their internal dynamics.

Sometimes random motions dominate the internal dynamics of galaxies. In this case they can be described thanks to the velocity dispersion inferred from the distribution of velocities. Typically, early-type galaxies are dominated by random motions and therefore their dynamics can be well characterised by this parameter (e.g. Emsellem et al. 2004). In many cases, galaxy internal dynamics are dominated by ordered motions that give a net rotation. This is typical of disc and irregular galaxies (e.g. Rubin & Ford 1970).

Nevertheless, it is worth noting that this is a schematic point of view. Only the most luminous elliptical galaxies show a complete absence of rotation; most ellipticals rotate to some degree (Emsellem et al. 2007). Other times their velocity distributions are more sophisticated and it is more convenient to characterise them using several terms of a Gauss-Hermite series (e.g. van der Marel & Franx 1993).

In addition, we should mention the utility of computing the angular momentum, which has showed to be useful in galaxy understanding (e.g. Prieto et al. 1989; Toloba et al. 2015).

1.2.6 Stellar population age

Following a similar approach to that explained in Section 1.2.1 for stellar mass estimation, a measurement of the average age of the stars which belong to a galaxy can be inferred. These are named stellar population ages to emphasize the fact that stars are not born randomly, but they appear in star forming episodes with a given IMF (as described also in Section 1.2.1).

When galaxies are formed in single fast star forming episodes, the stellar population age is not ambiguous. However, galaxies might have developed several star forming episodes during their lives. In that case, the average ages can be computed by weighting with mass or luminosity (e.g. Poggianti et al. 2013a). The mass-weighted ages will lead to older average ages than luminosity-weighted ages, because in this latter case the weight will be higher for young populations (as they will contain more luminous young stars).

1.2.7 Star formation rate

Another interesting observable of galaxies is the star formation rate. The idea behind all the proxies for estimating star formation rates is that most massive stars, which are also generally the bluest ones, are the stars with the shortest lives. Consequently, through the observables which are related to the amount of these stars, it is possible to infer the current star formation rate on galaxies. Some authors use the ultraviolet emission from the bluest stars for this goal (e.g. Donas & Deharveng 1984). In other works they detect indirect effects of the ultraviolet light of massive stars, such as recombination and forbidden emission lines (e.g. Kennicutt 1983; Gallagher et al. 1989), or the infrared flux whose origin is the absorption from dust (e.g. Calzetti et al. 2007).

1.2.8 Gas content

Although their stars are the essential part of a galaxy, extra components can be observed within galaxies, such as gas, dust, supermassive black holes. In the Introduction of this thesis we will only consider the gas, which is most relevant for the goals of our work.

It is known that the amount of gas within galaxies correlates with their morphological types. In particular, late-type galaxies usually contain gas, while early-type galaxies show a scarcity of this material (e.g. Mayall 1958).

The observational way of detecting gas depends on its ionization stage. For neutral gas, radio observations reveal clearly its presence (e.g. Stark et al. 1992). When ionised by massive stars, strong Hydrogen and Oxygen emission lines also indicate the existence of gas (e.g. Kennicutt 1979).

1.2.9 Dark matter

Another property which can be inferred from the observations is the amount of dark matter which a galaxy contains. Although its strange nature could lead to scepticism as to whether it is an *ad hoc* solution, its existence has been postulated based on much independent observational evidence.

The first firm evidence in favour of dark matter was reported by Zwicky (1933). He found that his measurement of the spread of velocities in the Coma cluster indicated a mass hundreds of times greater than mass derived from the luminous matter.

Other evidence is based on rotation curves of spiral galaxies. For example, Babcock (1939) studied the rotation curve of the Andromeda galaxy finding a flat profile, instead of a curve declining with distance (as should be expected from its light profile). However, he did not link his result with the existence of dark matter. We had to wait until the work performed by Rubin & Ford (1970) to identify connexion between rotation curves and dark matter.

Dark matter has also been inferred from the gravitational lensing produced by galaxy clusters (e.g. Gavazzi et al. 2007). And another independent clue for trusting in dark matter is the temperature and density of hot gas in clusters derived using X-ray emission (Vikhlinin et al. 2006). Finally, it is worth noting that dark matter is also an ingredient of the ΛCDM (lambda-cold dark matter, where lambda refers to the cosmological constant) model, whose success will be argued in the following section.

1.3 The current framework for galaxy formation

The current framework of our global view of the Universe is called the ΛCDM model. This model is based on a big bang cosmology and assumes that the Universe contains three ingredients: dark energy, dark matter and baryonic matter.

Although the big bang theories were initially discussed by the astronomical community, the discovery of cosmic microwave background by Penzias & Wilson (1965) radically changed this position.

After that starting point, much evidence has contributed to reinforce this model and/or to constrain its parameters, the most significant ones being:

- The expansion of the Universe measured through redshifts of supernovae (Riess et al. 1998; Perlmutter et al. 1999).
- The anisotropies from cosmic microwave background (Smoot et al. 1992).

- The sign of the baryonic acoustic oscillations in the distribution of galaxies (e.g. Eisenstein et al. 2005).
- The abundances in the primordial nucleosynthesis (e.g. Alpher et al. 1948; Gamow 1948a,b)

According to the ΛCDM model, in its first stages the Universe contained matter in thermal equilibrium. Thanks to the expansion of the Universe, the matter broke this equilibrium. In the assumption that dark matter is collisionless and does not interact with electromagnetic radiation, it is unstable under gravitational perturbations. For that reason, dark matter was the first one in forming overdensities. As the expansion increased, the baryonic matter broke from thermal equilibrium: light decoupled from the nuclei of the lightest atoms and isotopes. In that moment, already-formed overdensities of dark matter played a fundamental role, because they acted as the gravitational potential wells which conditioned the evolution of baryonic matter.

Thanks to numerical simulations we know that this evolution leads to a hierarchical (or bottom-up) scenario, i.e. the smaller structures of the Universe were formed first, and afterwards they were grouped by gravitational interaction in order to form the bigger structures.

However, the gravitational evolution of matter through the rest of the history of the Universe does not on its own correctly predict the baryonic structures. When one compares the predicted mass function of dark-matter simulations with an observed luminosity function of galaxies, an excess of low-mass and high-mass galaxies appears in the simulations. The way of reconciling both results is to consider baryonic physics (e.g. Bower et al. 2012). In particular, supernovae winds may explain the scarcity of low-mass galaxies, while active galactic nuclei may prevent the excess of high-mass galaxies. In the literature these processes are commonly referred to as the feedback.

1.4 Massive galaxies

1.4.1 Definition of massive galaxy

We name massive galaxies those objects which belong to the top tail of the stellar mass distribution of galaxies. The exact value for establishing the lower limit of their masses is not fixed. Often a $M_\star \gtrsim 10^{11}$ $\mathrm{M}_\odot$ is adopted, while the term is sometimes used to include galaxies down to $M_\star \gtrsim 10^{10}$ $\mathrm{M}_\odot$. The criterion is usually decided according to the sample which is being analysed. In this thesis we will use two limits: $M_\star \gtrsim 10^{11}$ $\mathrm{M}_\odot$ (for Chapters 3 and 4) and $M_\star \gtrsim 10^{10}$ $\mathrm{M}_\odot$ (for Chapter 5).

1.4.2 Usefulness of studying massive galaxies

Massive galaxies are interesting because they are the end-point of the galaxy growth process, where hierarchical merging makes specific predictions that can be observationally tested. We already noted that ΛCDM model in the absence of feedback predicts a higher abundance of massive galaxies than is observed. The cosmological evolution of the massive end of the galaxy mass function provides additional tests: did massive galaxies form before or after less-massive galaxies (e.g. Pérez-González et al. 2008)?

Studying galaxy evolution using the population of massive galaxies has two main advantages. First, these galaxies will be bright thanks to the amount of stars that they contain, and consequently can be observed to high redshift. Second, it is expected that most of these galaxies which become members of this population will remain massive throughout their lives (in contrast to other bright populations, such as active or star-forming galaxies). The reason is that the loss of a relevant fraction of mass from massive galaxies is not common. These two advantages mean that given two samples of massive galaxies at different cosmic times one can think that most of the descendants of the previous time should be contained in the later one (e.g. Trujillo et al. 2011). However, it is worth noting that new incorporations through mass growth can happen, and therefore some galaxies will not have massive progenitors (e.g. Khochfar & Silk 2006).

Thanks to these advantages massive galaxies are ideal as a laboratory for testing galaxy evolution, and in particular, for testing the hierarchical clustering.

1.4.3 Key observational properties relating to massive galaxies

Colour–magnitude diagram

The galaxy colour–magnitude diagram is a powerful astronomical tool because it establishes that more luminous galaxies tend to be redder (e.g. Visvanathan & Sandage 1977; Peletier et al. 1990). Redder colours may indicate older ages and/or higher metallicities. The study of the large galaxy database from the Sloan Digital Sky Survey (hereinafter SDSS; York et al. 2000) revealed that the distribution of galaxies in colour and luminosity space is bimodal (Kauffmann et al. 2003). The distribution of galaxies in the colour–magnitude is schematically shown in Fig. 1.2. This figure explains that red galaxies populate a tighter region of the diagram than blue galaxies. In addition, it shows that the highest-luminosity galaxies have red colours. As luminosity and colour traces mass and age respectively, this diagram indicates that massive galaxies are mainly old. This result would seem to support the idea of a monolithic collapse for the formation of massive galaxies (e.g. Eggen et al. 1962), challenging the framework

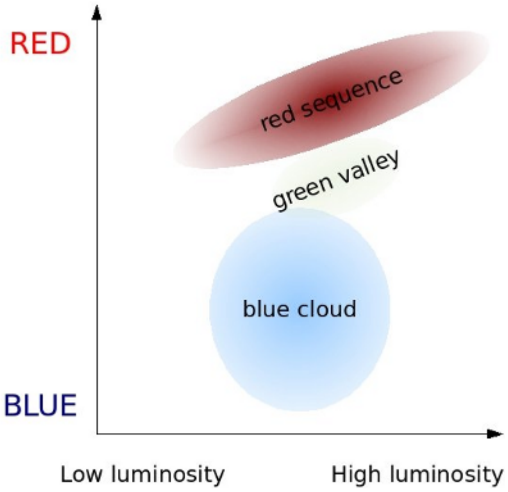

Figure 1.2. Galaxy colour–magnitude diagram showing the red sequence, green valley and blue cloud. *Image from Joshua Schroeder and publicly available at* `https://commons.wikimedia.org/wiki/File:Galaxy_color-magnitude_diagram.jpg` *under a license Creative Commons BY-SA 3.0.*

of the ΛCDM model (c.f. Section 1.3).

Downsizing

Another seeming paradox for the ΛCDM model is the downsizing phenomenon. In particular, we are referring to the fact that more massive galaxies appear older and complete star formation sooner than less massive systems (e.g. Cowie et al. 1996; Fontanot et al. 2009). However, in the ΛCDM model, structures grow monotonically in mass.

Nearby stellar mass–size relationship

The scaling relationship between the stellar mass and size gives us more information about the properties of massive galaxies. Focusing on early-type galaxies, we see that this relationship can be characterised using a straight line in log–log space with a slope around 0.6 (e.g. Shen et al. 2003). This slope is higher than $\frac{1}{3}$, which is the slope that these objects would follow if they were to have the same density. As they do not follow the constant-density slope, we know that more massive galaxies are less dense objects.

Growth of massive galaxies

Many studies have shown that massive galaxies have smaller sizes at higher redshift (e.g. Daddi et al. 2005; Trujillo et al. 2007; Buitrago et al. 2008). Furthermore, this size evolution is stronger for early-type galaxies than late-type galaxies (e.g. Trujillo et al. 2007; van der Wel et al. 2014). Another interesting fact reported by van der Wel et al. (2014) is that the slope of the stellar mass–size relationship is constant. This growth of massive galaxies seems to support a hierarchical scenario, as expected, for example, in the ΛCDM model.

1.5 Open questions on massive galaxies

1.5.1 Mass determinations: Comparison between stellar population techniques and estimations from virial theorem with the assumption of homology

The discovery that massive galaxies are more compact at higher redshifts was revealed using stellar masses from stellar population techniques (e.g. Daddi et al. 2005; Trujillo et al. 2007; Buitrago et al. 2008). The reason for selecting these masses is simple: they are easiest to observe because they only require spectral energy distributions from broad-band photometry.

Nevertheless, with the arrival of 10-m telescopes, access to velocity dispersions at higher redshifts is increasing (e.g. Newman et al. 2010; Martinez-Manso et al. 2011). These measurements, together with the virial theorem and the assumption of homology, allow us to estimate dynamical masses for early-type galaxies. In particular, the virial theorem (e.g. Binney & Tremaine 1987) states that there is an energy balance between potential and kinetic energy, which translates into the equation

$$\frac{GM_{\mathrm{dyn}}}{\langle r \rangle_\tau} = k_E \, \frac{\langle v^2 \rangle_\tau}{2}, \tag{1.2}$$

being M_{dyn} the dynamical mass, G the gravitational constant, $\langle r \rangle_\tau$ the mean of the stellar distances to the centre of the system at time τ, $\langle v^2 \rangle_\tau$ twice the kinetic energy of the system per unit mass at time τ and $k_E = 2$ the virialization constant.

Unfortunately, the magnitudes involved in the above equation are not directly observable. Assuming that early-type galaxies are self-similar objects, there will exist observables O_r and O_v such that $\langle r \rangle = k_r O_r$ and $\langle v^2 \rangle = k_v O_v^2$, where k_r and k_v are universal constants for all early-type galaxies (or at least their product). In this case, it will be possible to calibrate this equation in order to apply the following expression on any early-type galaxy:

$$M_{\rm dyn} = K \, \frac{O_v^2 O_r}{G}, \tag{1.3}$$

where $K \equiv \frac{k_E}{2} k_v k_r$.

This approach has been used for a long time and it is still very popular (e.g. Drory et al. 2004; Taylor et al. 2010b). For example, Cappellari et al. (2006) checked the validity of this method using the observables $r_{\rm e}$ and $\sigma_{\rm e}$ (the effective radius and the velocity dispersion within this radius, respectively), and found $K = 5.0$. However, several authors have reported that they find non-physical results when they compare their findings from this technique with stellar masses from stellar population techniques, that is, they find stellar masses greater than dynamical masses. Most of them reported this problem at high-redshift (Stockton et al. 2010; Martinez-Manso et al. 2011; Barro et al. 2014; Stockton et al. 2014), but also Ferré-Mateu et al. (2012) found it in the nearby Universe. Presently there is no clear consensus on what could be the explanation of this problem, and there is no prescription for predicting when this problem is going to appear.

Is this problem telling us something about the different nature of the compact objects? Or even could the stellar mass estimations be failing at high-redshift?

1.5.2 Evolutionary paths from high z massive galaxies to $z = 0$ massive ellipticals

The main question about massive galaxies is what are the evolutionary pathways that they have followed during the last 13.7 Gyr. In principle, there could be two ways of explaining the evolution of the stellar mass–size scaling relationship: either (i) the arrival of new massive galaxies which populate the top region of the stellar mass–size relationship (e.g. Khochfar & Silk 2006), or (ii) a mechanism which is evolving in size the already massive progenitors (e.g. Naab et al. 2007; Fan et al. 2008).

In any case, the strong size evolution of early-type massive galaxies (e.g. Trujillo et al. 2007; van der Wel et al. 2014) together with the decrease in the number density of massive compact galaxies (Poggianti et al. 2013b) imply that a mechanism which grows these objects is necessary.

For this part of the problem, two solutions have been proposed:

- Dry mergers (e.g. Naab et al. 2007, 2009; Hopkins et al. 2009). This solution requires low gas fraction, i.e. to avoid a high amount of star formation, in order to guarantee the old ages of the stellar population of nearby massive galaxies.

- Puffing up scenarios (e.g. Fan et al. 2008; Damjanov et al. 2009; Ragone-Figueroa & Granato 2011). The injection energy within the galaxy could modify the equilibrium between the kinetic and potential energies, leading to an expansion of the galaxy. Several sources have been proposed as the origins of this energy: active nuclei, stellar winds, supernova explosions…

Several works indicate that the most promising way is through dry mergers (e.g. Kaviraj et al. 2009; Shankar et al. 2010; Trujillo et al. 2011). For example, Trujillo et al. (2011) refuted some of the predictions from puffing-up scenarios, and that the scaling relationship seems to fulfil the predictions of dry mergers. However, an issue arises: the ratio of major mergers (i.e. the mergers between galaxies with similar masses) is not high enough to explain the size evolution (e.g. Bundy et al. 2009; López-Sanjuan et al. 2010). This is problematic because in that case we require the contribution of minor mergers, which are not directly verifiable through the observations. Consequently, adding new observational evidence for this mechanism will help to increase the reliability of this solution.

2

Aims and outline of this thesis

The discovery that massive galaxies are on average more compact in the primitive Universe has shown the importance of the understanding of the mechanisms which produce growth of galaxies in size with cosmic time. A better knowledge of the characteristics of these compact objects will give us clues about the nature of the mechanism which is contributing to the growth of massive galaxies.

In this thesis our aims will be to shed light on the following questions:

1. Are massive compact galaxies self-similar objects to the normal-sized galaxies? In particular, is it correct to apply the homologous hypothesis for computing the dynamical masses of these objects?
2. If we can or cannot apply the homologous hypothesis for massive compact galaxies, how does this fact constrain the mechanism which is increasing the size of massive galaxies?
3. If the mechanism which causes massive galaxies to grow is stochastic, such as mergers, relic galaxies will exist, that is, objects which are survivors of the action of this mechanism. In this case, what will be the preferred environment of these relics?

In Chapter 3 we used a sample of early-type galaxies with $M_\star \gtrsim 10^{11}$ M$_\odot$ from redshift 0 up to 2.5, including 11 stacked spectra built by ourselves, for answering the first question.

In Chapter 4 we study again the first question, but using two snapshot samples at redshifts 1 and 0. We start by obtaining spectroscopy of six $z \sim 1$

galaxies with GTC/OSIRIS and deriving velocity dispersions from the spectra. These two snapshots liberate us from potential redshift-dependent systematics in mass determinations which could be argued against the sample used in the previous chapter.

Furthermore, in Chapter 4 we address the second question considering the information from this chapter and the previous one.

The third question is studied in Chapter 5. For that we will use a catalogue of nearby galaxies with stellar masses above 10^{10} $M_{\odot}$.

In Chapter 6 we summarise the conclusions given in Chapters 3, 4 and 5 (Section 6.1), and describe various avenues of future research suggested by this thesis (Section 6.2).

3

The discrepancy between dynamical and stellar masses in massive compact galaxies traces non-homology

The material included in this chapter has already been published by Peralta de Arriba et al. (2014). This article has been accepted for publication in Monthly Notices of the Royal Astronomical Society ©: 2014 Luis Peralta de Arriba, Marc Balcells, Jesús Falcón-Barroso and Ignacio Trujillo. Published by Oxford University Press on behalf of the Royal Astronomical Society. All rights reserved.

DOI: 10.1093/mnras/stu317

The discrepancy between dynamical and stellar masses in massive compact galaxies traces non-homology

Luis Peralta de Arriba,[1,2★] Marc Balcells,[1,2,3] Jesús Falcón-Barroso[1,2]
and Ignacio Trujillo[1,2]
[1] *Instituto de Astrofísica de Canarias (IAC), E-38200 La Laguna, Tenerife, Spain*
[2] *Universidad de La Laguna, Department Astrofísica, E-38206 La Laguna, Tenerife, Spain*
[3] *Isaac Newton Group of Telescopes, E-38700 Santa Cruz de La Palma, La Palma, Spain*

Accepted 2014 February 14. Received 2014 February 14; in original form 2013 July 17

ABSTRACT

For many massive compact galaxies, their dynamical masses ($M_{\rm dyn} \propto \sigma^2 r_{\rm e}$) are lower than their stellar masses ($M_\star$). We analyse the unphysical mass discrepancy $M_\star/M_{\rm dyn} > 1$ on a stellar-mass-selected sample of early-type galaxies ($M_\star \gtrsim 10^{11}$ M$_\odot$) at redshifts $z \sim 0.2$ to $z \sim 1.1$. We build stacked spectra for bins of redshift, size and stellar mass, obtain velocity dispersions, and infer dynamical masses using the virial relation $M_{\rm dyn} \equiv K\,\sigma_{\rm e}^2 r_{\rm e}/G$ with $K = 5.0$; this assumes homology between our galaxies and nearby massive ellipticals. Our sample is completed using literature data, including individual objects up to $z \sim 2.5$ and a large local reference sample from the Sloan Digital Sky Survey (SDSS). We find that, at all redshifts, the discrepancy between $M_\star$ and $M_{\rm dyn}$ grows as galaxies depart from the present-day relation between stellar mass and size: the more compact a galaxy, the larger its $M_\star/M_{\rm dyn}$. Current uncertainties in stellar masses cannot account for values of $M_\star/M_{\rm dyn}$ above 1. Our results suggest that the homology hypothesis contained in the $M_{\rm dyn}$ formula above breaks down for compact galaxies. We provide an approximation to the virial coefficient $K \sim 6.0[r_{\rm e}/(3.185\,{\rm kpc})]^{-0.81}[M_\star/(10^{11}\,{\rm M}_\odot)]^{0.45}$, which solves the mass discrepancy problem. A rough approximation to the dynamical mass is given by $M_{\rm dyn} \sim [\sigma_{\rm e}/(200\,{\rm km\,s^{-1}})]^{3.6}[r_{\rm e}/(3\,{\rm kpc})]^{0.35} 2.1 \times 10^{11}\,{\rm M}_\odot$.

Key words: galaxies: elliptical and lenticular, cD – galaxies: evolution – galaxies: fundamental parameters – galaxies: high-redshift – galaxies: kinematics and dynamics – galaxies: structure.

1 INTRODUCTION

Observations in the last decade have shown that the mean size of massive ($M_\star \gtrsim 10^{11}$ M$_\odot$) galaxies evolves with redshift (z); that is, these galaxies have, at a fixed stellar mass, a smaller size at higher redshifts (e.g. Daddi et al. 2005; Trujillo et al. 2006; Longhetti et al. 2007; Toft et al. 2007; Zirm et al. 2007; Buitrago et al. 2008; Cimatti et al. 2008). The size evolution is more dramatic for early-type galaxies (ETGs) than for late-type galaxies (Trujillo et al. 2007, hereinafter T07). In fact, at $z \sim 2$ a large number of massive ETG galaxies have sizes, as parametrized by the effective radius, of ∼1 kpc. These objects have been termed massive compact galaxies in the literature. Only a few of these galaxies have been found in the nearby Universe (e.g. Trujillo et al. 2009; Taylor et al. 2010; Poggianti et al. 2013; Trujillo et al. 2014).

With the increasing availability of velocity dispersion measurements for massive compact galaxies, it has become apparent that dynamical masses, estimated using the virial relationship $M_{\rm dyn} \propto \sigma^2 r_{\rm e}$, often turn out to be lower than stellar masses. This occurs at low as well as at high redshifts. Stockton, Shih & Larson (2010) and Martinez-Manso et al. (2011) found this problem for two galaxies at $z \sim 0.5$ and for four galaxies at $z \sim 1$, respectively. Ferré-Mateu et al. (2012) report the same result for seven massive compact galaxies in the nearby Universe ($z \sim 0.14$).

As the inequality $M_\star > M_{\rm dyn}$ is unphysical, it follows that, for these objects, either the dynamical masses are underestimated or the stellar masses are overestimated. Both conditions could of course apply simultaneously.

Stellar mass determinations are based on the comparison of galaxy spectral energy distributions (SEDs) with synthetic spectra of stellar populations built using the current knowledge of stellar spectra, stellar evolution, the initial mass function (IMF), star formation history and dust attenuation. It is believed that the uncertainty in these parameters can lead to an error in the estimation

---

[★] E-mail: lperalta@iac.es

of the stellar mass by factors of up to 2–4 (Conroy, Gunn & White 2009; Muzzin et al. 2009). The comparison with stellar synthesis models can be carried out using broad-band photometric data, and hence this method provides an efficient means of estimating stellar masses for galaxies at high redshift.

Several techniques are available to derive dynamical masses. The most accurate methods are based on one of two approaches: the solution of Poisson and Jeans equations (e.g. Satoh 1980), or the description of the system using an orbit-superposition method (Schwarzschild 1979). These methods require high-quality two-dimensional spectroscopic data, making them expensive in observing time. A cheaper alternative, and the only one available today for high-redshift galaxies, is to use simpler mass estimators based on the virial theorem. Following the notation in Djorgovski, de Carvalho & Han (1988), we write the virial theorem as

$$\frac{GM_{\rm dyn}}{\langle r\rangle} = k_E\,\frac{\langle v^2\rangle}{2}, \tag{1}$$

where G is the gravitational constant, $\langle r\rangle$ is the gravitational radius of the system, $\langle v^2\rangle$ is twice the kinetic energy of the system per unit mass, and k_E is the virialization constant. k_E has the value $k_E = 2$ when the system is virialized. Unfortunately, $\langle r\rangle$ and $\langle v^2\rangle$ are not direct observables. For this reason, it is common to define two coefficients, k_r and k_v, which connect these magnitudes with direct observables that provide galactic length and velocity scales respectively (O_r and O_v). These coefficients are defined by the following equalities:

$$\langle r\rangle = k_r O_r, \tag{2}$$

$$\langle v^2\rangle = k_v O_v^2. \tag{3}$$

k_r and k_v are coefficients describing the spatial and dynamical structure of the objects, respectively. Using equations (2) and (3), it is straightforward to express the virial theorem (equation 1) in terms of observables:

$$M_{\rm dyn} = K\,\frac{O_v^2 O_r}{G}, \tag{4}$$

where we have defined K as

$$K \equiv \frac{k_E}{2} k_v k_r. \tag{5}$$

The coefficient K will be a universal constant only if the coefficients k_r and k_v are the same for all ETGs (or if their dependences disappear in their product). This hypothesis is known as homology, because it would be verified if all ETGs had the same mass density, and kinematic and luminosity structures. Following these ideas, Cappellari et al. (2006) selected the effective (half-light) radius $r_{\rm e}$ and the luminosity-weighted second moment $\sigma_{\rm e}$ of the line-of-sight velocity distribution (LOSVD) within $r_{\rm e}$ to play the role of observables O_r and O_v; that is, they used the following equation:

$$M_{\rm dyn} = K\,\frac{\sigma_{\rm e}^2 r_{\rm e}}{G}. \tag{6}$$

Using a sample of nearby and normal-sized ETGs, these authors found that K is approximately constant and they proposed the following calibration as a reliable estimator of the dynamical mass for an ETG:

$$M_{\rm dyn} = (5.0 \pm 0.1)\,\frac{\sigma_{\rm e}^2 r_{\rm e}}{G}. \tag{7}$$

This formula is used in the references mentioned above that lead to the reported discrepancy between dynamical and stellar masses. Hereinafter, we will always use the term dynamical mass to refer to the mass calculated using equation (7).

In this work we characterized the fraction $M_\star/M_{\rm dyn}$ at various redshifts and covering various regions of the mass–size space. We used this information to determine in which areas of this parameter space the mass predictions produce the impossible result $M_\star > M_{\rm dyn}$.

Our paper is structured as follows. In Section 2, we present a description of our sample and additional sources of data. We describe the processing of spectra and velocity dispersion measurements of our sample in Section 3. In Section 4, we show our results for $M_\star/M_{\rm dyn}$ and argue that $M_\star$ uncertainties alone cannot explain values of $M_\star/M_{\rm dyn} > 1$. We interpret the discrepancy as a non-homology effect in Section 5. In Section 6 we discuss our results. We summarize our conclusions in Section 7. We adopt a ΛCDM cosmology with $\Omega_{\rm m} = 0.3$, $\Omega_\Lambda = 0.7$ and $H_0 = 70$ km s^{-1} Mpc^{-1}. The stellar masses are obtained assuming a Salpeter IMF (we applied a conversion factor when necessary following the prescriptions from Longhetti & Saracco 2009).

2 DESCRIPTION OF THE DATA

2.1 Cross-matching T07 massive galaxies with the DEEP2 DR4 survey

Our targets belong to the catalogue of massive galaxies studied by T07. This catalogue contains 796 galaxies with redshifts between 0.2 and 2. The authors split their sample into two groups: one containing objects that have a Sérsic index $n < 2.5$ (disc-like galaxies) and the other containing galaxies that have $n > 2.5$ (spheroid-like galaxies). This criterion is based on the correlation between the Sérsic index n and the morphological type observed both in the nearby Universe (Ravindranath et al. 2004) and in the high-redshift Universe (see e.g. Buitrago et al. 2013b). In this work, we focus on the spheroid-like galaxies, which are the set with a stronger size evolution. Therefore, our initial catalogue contains the 463 massive galaxies with $n > 2.5$.

An extra requirement we apply to this subsample is the availability of a spectrum in the unique redshift DEEP2 DR4 catalogue (Davis et al. 2003, 2007; Newman et al. 2013). DEEP2 DR4 was designed to conduct a comprehensive census of massive galaxies, and their properties, environments and large-scale structure down to an absolute magnitude $M_B = -20$ at $z \sim 1$. The targets of this catalogue are located in four fields, which have a total area of 2.8 deg^2. One of these fields is the Extended Groth Strip (EGS, Davis et al. 2007). All the galaxies studied by T07 are located in the EGS field. This is relevant because the EGS is the only field of the DEEP2 DR4 survey in which colour pre-selection was not applied.

The cross-match between the DEEP2 DR4 catalogue and the spheroid-like T07 galaxies was performed using the *OBJNO* index on the first and the *galaxy identification* on the second. Both indices come from the sample defined by Coil et al. (2004). The number of matches is 260.

Other requirements were applied to this set in order to avoid contaminant objects. Two targets were rejected for being too small to be reliable (they had a semimajor axis equal to 0.01 arcsec and an effective radius ∼0.01 kpc). We also required our galaxies to have a secure redshift, namely galaxies with quality codes equal to 3 or 4 in the DEEP2 DR4 catalogue. Only in two cases was the difference between the redshift used by T07 ($z_{\rm T07}$) and the secure redshift published by DEEP2 DR4 (z) significant; that is, it was not the case that $|z_{\rm T07} - z|/(1+z) < 8$ per cent, $0.89 < z/z_{\rm T07} < 1.15$

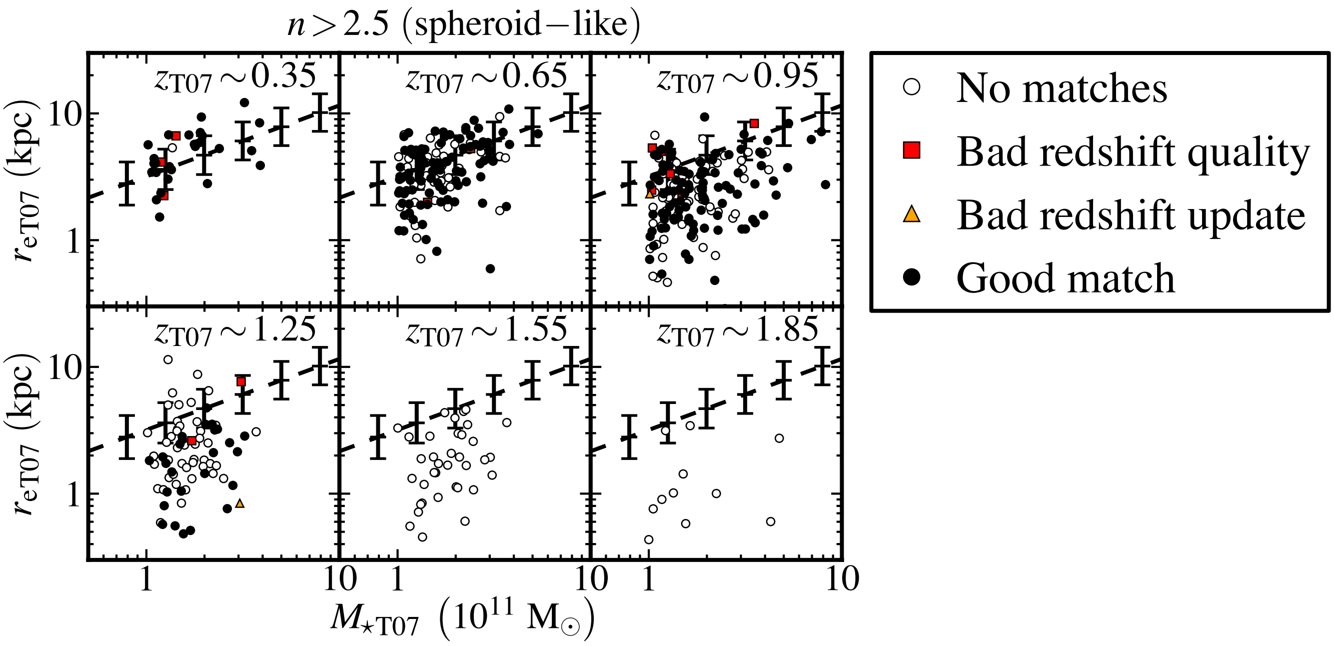

Figure 1. The stellar mass–size distribution of the spheroid-like galaxies ($n > 2.5$) of the T07 sample. The squares and triangles denote objects that are discarded because their DEEP2 DR4 redshifts are not secure, and the differences between the redshift used by T07 and the secure redshift published by DEEP2 DR4 are significant (see text for more details). The black circles represent the matches between T07 and DEEP2 DR4 that we have not rejected, while the white circles are T07 galaxies without available spectra in the DEEP2 DR4 sample. The dashed line shows the relationship that the early-type galaxies follow in the nearby Universe (Shen et al. 2003). Error bars over-plotted on the dashed line show the dispersion of this relationship. Stellar masses, radii and redshifts used in this figure are the same as those used in T07.

and $|z_{T07} - z|/z < 13$ per cent. These two targets were rejected. With these extra requirements, our final catalogue comprised 243 sources.

In Fig. 1 we plot the information from the cross-match between the two catalogues in the stellar mass–size diagram. It can be seen that our sample is restricted to $z_{T07} < 1.4$. In the three lower redshift bins, most of the points satisfy our requirements, but this is not the case in the $z_{T07} \sim 1.25$ bin. A relevant fact that we can check in Fig. 1 is that there are no biases affecting the stellar mass–size distribution in the three lower redshift bins.

2.2 Information taken from the T07 and DEEP2 DR4 catalogues

We summarize here the parameters that we will use throughout this work, detailing in each case whether the parameter was extracted from the DEEP2 DR4 or the T07 catalogue, or whether it was derived from a combination of parameters from both catalogues.

(i) Sérsic index n: taken from the T07 catalogue.

(ii) Redshift z: taken from the DEEP2 DR4 catalogue, so all values are spectroscopic.

(iii) Circularized effective radius r_e: effective radii in arcseconds were obtained from T07, and these quantities were then converted to kiloparsecs using the DEEP2 DR4 redshifts. We compared our effective radii in kiloparsecs with the T07 radii (r_{eT07}), and checked that they were very similar, namely that they satisfied $0.93 < r_e/r_{eT07} < 1.05$.

(iv) Stellar mass $M_\star$: this magnitude was recalculated based on the T07 stellar masses ($M_{\star T07}$) and considering the DEEP2 DR4 redshift (z) as a small correction of the T07 redshift (z_{T07}). Specifically, we considered that the luminosity of an object should be corrected using the equation $L/L_{T07} = [\mathrm{d}(z)/\mathrm{d}(z_{T07})]^2$, where L is the updated luminosity at redshift z, L_{T07} is the luminosity at T07 redshift z_{T07}, and $d(z)$ is the luminosity distance at redshift z. We also assumed that the stellar mass–luminosity ratio should be very similar to that considered by T07 for each galaxy; that is, we used that $M_\star/L = k = M_{\star T07}/L_{T07}$. These hypotheses imply that the mass correction formula is $M_\star = [d(z)/d(z_{T07})]^2 M_{\star T07}$. We compared the updated stellar masses with T07 stellar masses and found that the differences were small ($0.75 < M_\star/M_{\star T07} < 1.42$).

(v) Individual galaxy spectra: taken from the DEEP2 DR4 survey. These spectra were obtained using three exposures of 20 min each with the multislit spectrograph DEIMOS (Faber et al. 2003) on the Keck II telescope. The observations were performed under seeing conditions between 0.5 and 1.2 arcsec. Their spectral range is 6500–9300 Å, and their spectral resolution R is 5900 at 7800 Å. They have a ∼2-Å gap in the middle of the spectral range, owing to the multiCCD nature of the DEIMOS detector.

2.3 The T07-DEEP2 DR4 sample

Fig. 2 shows the mean rest-frame signal-to-noise ratio of the spectra available for each target selected in Section 2.1 over their stellar mass–size distribution. Most galaxies are located in the three lower redshift bins. As we will use these spectra to make stacked spectra later on and to measure their velocity dispersions, we limit our present sample to targets selected in Section 2.1 that (i) have spectra with a signal-to-noise ratio greater than 5 Å^{-1}, and (ii) have redshifts in the range $0.2 < z < 1.1$.

2.4 Additional data: from SDSS up to high-redshift galaxies

In Sections 4 and 5 we use additional data in the analysis of our results. We took some data of individual galaxies from the literature

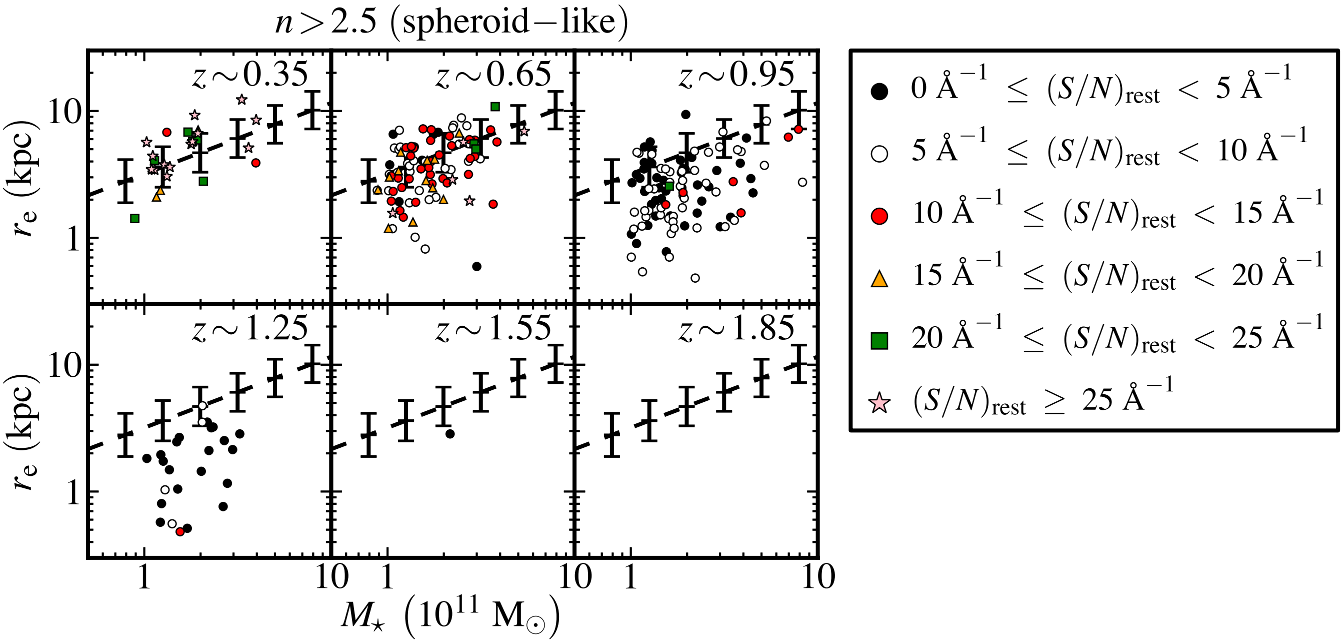

Figure 2. The stellar mass–size distribution of the spheroid-like galaxies ($n > 2.5$) with a good match between T07 and DEEP2 DR4 catalogues. The symbols represent the mean rest-frame signal-to-noise ratio of the DEEP2 DR4 spectra available for each object. The dashed line shows the relationship that the early-type galaxies follow in the nearby Universe (Shen et al. 2003). Error bars over-plotted on the dashed line show the dispersion of this relationship. Stellar masses, radii and redshifts used in this figure were determined as detailed in Section 2.2.

in order to explore whether our data are affected by potential biases arising from the stacking process employed in the T07-DEEP2 DR4 sample. All these individual galaxies are massive ($M_\star > 10^{11}$M$_\odot$) and spheroid-like ($n > 2.5$). We used six nearby massive compact galaxies from Ferré-Mateu et al. (2012), four galaxies from Stockton et al. (2014) at $z \sim 0.5$ (these galaxies include the two galaxies from Stockton et al. 2010), and the four galaxies from Martinez-Manso et al. (2011) at $z \sim 1$. As detailed in the Introduction, a discrepancy between $M_\star$ and $M_{\rm dyn}$ has been reported for all these galaxies. We have included dynamical and stellar masses from the compilation of masses and structural parameters for high-redshift individual galaxies carried out by van de Sande et al. (2013). This compilation was made using data from van der Wel et al. (2008), Blakeslee et al. (2006), Bezanson et al. (2013), Cappellari et al. (2009), Newman et al. (2010), van de Sande et al. (2013), Onodera et al. (2012), van Dokkum, Kriek & Franx (2009) and Toft et al. (2012), and it covers the redshift range from 0.9 to 2.2. We also took 32 massive spheroid-like galaxies from the recent work by Belli, Newman, & Ellis (2014) with redshifts between 1.0 and 1.6.

We also use data from Cenarro & Trujillo (2009), which include the results of the Sloan Digital Sky Survey NYU Value Added Galaxy Catalogue DR6 (Blanton et al. 2005; Blanton & Roweis 2007), van der Wel et al. (2005, 2008), di Serego Alighieri et al. (2005) and Cimatti et al. (2008). These authors have provided us with the mean values of individual stellar masses and redshifts. Furthermore, Cenarro & Trujillo (2009) kindly provided us with tabulated values of mean sizes, redshifts and velocity dispersions used in their paper (except for their highest-redshift data point, where the mean velocity dispersion is the velocity dispersion on a stacked spectra). In this case, we assigned a mean dynamical mass to each data value, introducing the mean values of radius and velocity dispersion in equation (7).

Finally, we added a sample of 53 571 galaxies from the NYU Value-Added Galaxy Catalog DR7 (hereinafter NYU SDSS sample, or the NYU sample of SDSS galaxies). These galaxies were selected using the following criteria: they are massive (10^{11} M$_\odot$ $< M_\star < 10^{12}$ M$_\odot$), spheroid-like ($n > 2.5$), and close to the peak of the redshift distribution of the SDSS catalogue ($0.05 < z < 0.11$). To avoid unreliable data, we applied extra restrictions to the SDSS sample: reliable velocity dispersions, physical radii and apparent sizes, namely $70\,{\rm km\,s^{-1}} < \sigma < 420\,{\rm km\,s^{-1}}$, $0.3\,{\rm kpc} < r_e < 30\,{\rm kpc}$, and $r_e > 1$ arcsec. The last condition is applied to ensure that the apparent sizes are larger than the average full width at half-maximum (FWHM) ground-based data. In addition, we applied the aperture correction for velocity dispersions given in equation (1) of Cappellari et al. (2006), although our results are insensitive to this change.

In Fig. 3 we show the distribution of these additional data in the stellar mass–size diagram.

3 PROCESSING OF SPECTRA AND VELOCITY DISPERSION MEASUREMENTS IN THE T07-DEEP2 DR4 SAMPLE

In order to obtain robust velocity dispersion measurements it is necessary to have a set of spectra with a high enough signal-to-noise ratio. This is achieved in our T07-DEEP2 DR4 sample by using the spectral stacking technique. The steps followed by us in the processing of the spectra can be classified into three categories, which were applied in the following order: corrections to the individual spectra, stacking of spectra, and, finally, velocity dispersion measurements. The following subsections provide the details of each step.

3.1 Corrections to the individual spectra

The corrections applied to the individual spectra were as follows.

(i) *Throughput correction.* The spectra available in the DEEP2 DR4 data base are not relative-flux-calibrated. To obtain this

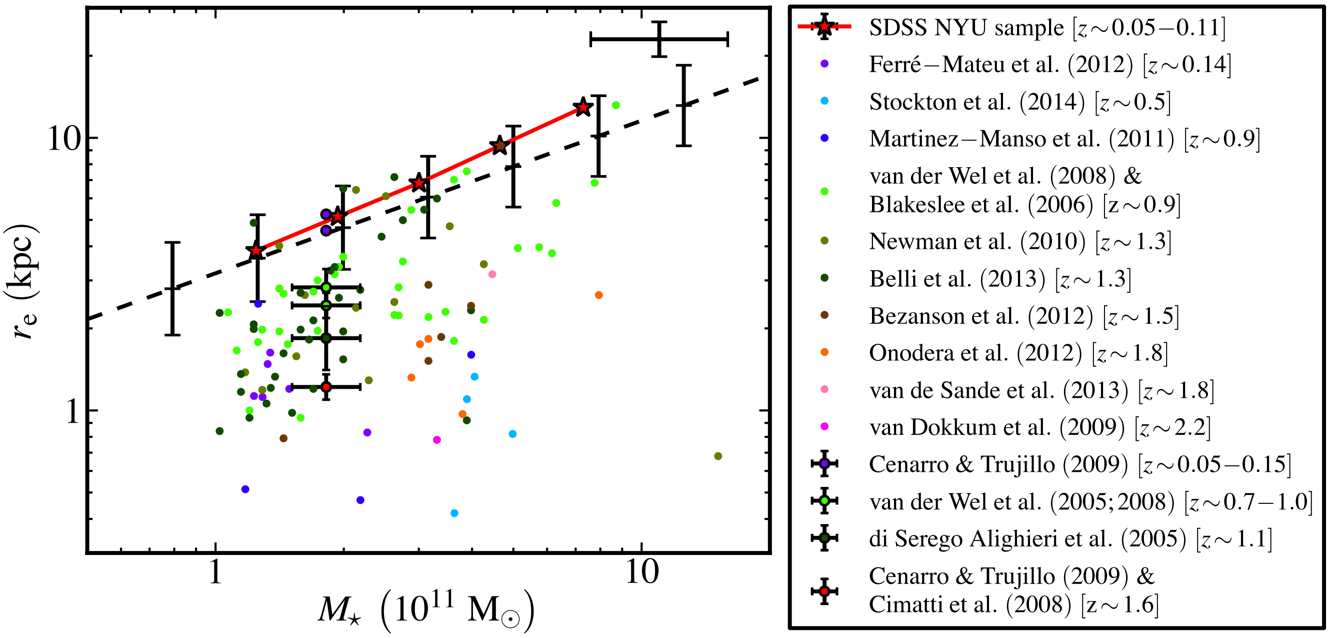

Figure 3. The stellar mass–size distribution of the additional data used in this paper described in Section 2.4. The symbols indicate the origin of each data set. Symbols with/without black edges represent the 'average'/individual galaxies. For clarity, the NYU sample of SDSS galaxies has been plotted to show the mean properties of SDSS galaxies after a stellar-mass binning. The dashed line shows the relationship that the early-type galaxies follow in the nearby Universe (Shen et al. 2003). Error bars over-plotted on the dashed line show the dispersion of this relationship. The error bar cross in the top right corner of the figure represents the mean error of the individual galaxies.

calibration, we divided each spectrum by the throughput of the DEIMOS spectrograph (see e.g. Schiavon et al. 2006). We used the data published for an instrumental configuration with the gold 1200 l/mm grating and the OG550 filter.[1] For the bluer regions of some spectra, the throughput data are not available, and hence we cut those parts of the spectra.

(ii) *CCD-level relative calibration.* A visual inspection of the spectra shows that about 30 per cent of the spectra have a calibration problem between the two CCDs of the spectrograph. We corrected for this by applying a scaling factor to the red region of the spectrum. The scaling factors ranged from 0.6 to 1.5.

(iii) *Pixel masking.* Some spectra have sharp variations at the CCD edges. Furthermore, two telluric absorption bands were identified (located at 6860–6922 and 7587–7714 Å). These bands belong to the O_2 absorption spectrum (Stevenson 1994). These pixels were masked during the stacking process.

(iv) *Flux normalization.* We carried out a flux normalization before the stacking process. For each redshift bin we used a different rest-frame wavelength region: 5500–5700 Å for $0.2 < z < 0.5$; 4500–4700 Å for $0.5 < z < 0.8$; and 4150–4250 Å for $0.8 < z < 1.1$.

3.2 Stacking of spectra

We stacked our spectra in order to reach a signal-to-noise level that enabled us to measure the velocity dispersions with confidence. The stacking process was carried out as follows.

(i) Redshift correction to each individual spectrum.

(ii) Interpolation of each spectrum to a common wavelength vector.

(iii) Averaging of spectra to be co-added. We used a non-weighted mean, but our essential results remain unchanged if we use a mean where weights are the mean signal-to-noise ratio per angstrom of each spectrum. We chose the non-weighted option because signal-to-noise weighting introduces biases towards the brightest galaxies.

We split our sample into three redshift bins ($0.2 < z < 0.5$, $0.5 < z < 0.8$ and $0.8 < z < 1.1$), and each redshift bin was further split into two stellar-mass bins and two effective radius bins. Boundaries were 1.5×10^{11} M$_\odot$ and 2.5 kpc for mass and size, respectively. A stacked spectrum was built for each bin. Applying this procedure, we obtained 11 stacked spectra (the high-mass, small-size, low-redshift bin is empty). In Fig. 4, we show the mean stellar masses and radii corresponding to these stacked spectra.

3.3 Velocity dispersion measurements

In order to compute the velocity dispersion of our stacked spectra, we used the penalized pixel-fitting (pPXF) method of Cappellari & Emsellem (2004). Details of the fitting procedure are as in Falcón-Barroso et al. (2011). A relevant pPXF input parameter is the spectral library used to fit each spectrum. We used a set of 82 stars taken from the ELODIE library (Prugniel et al. 2007) that cover a wide range of stellar parameters (T_{eff}, [Fe/H], $\log(g)$), which allowed us to minimize the impact of template mismatch. Table 1 lists the characteristics of the T07-DEEP2 DR4 stacked spectra, including the results from the velocity dispersion measurements.

In order to check the robustness of the error velocity dispersion errors, we performed a set of simulations, described in Appendix A. We checked that the error estimations in this simulation were on average 1.8 times higher than the errors of the velocity dispersion measured in the stacked spectra in Table 1, the ratios between these errors. As this simulation was developed based on an adverse single

---

[1] The throughput data for several configurations have been made public at http://www.ucolick.org/~ripisc/results.html.

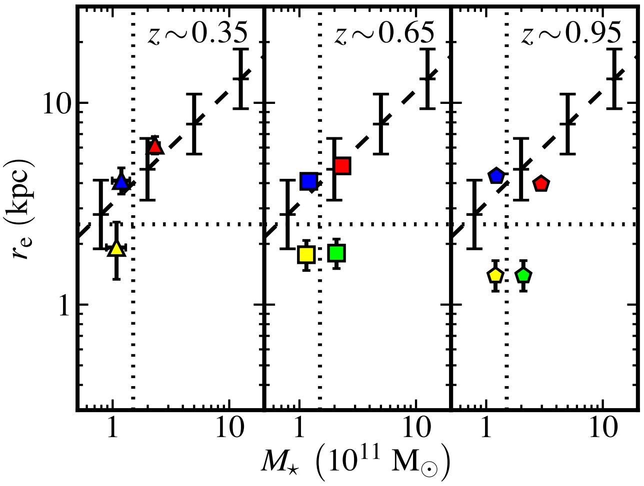

Figure 4. The stellar mass–size distribution of the stacked spectra described in Section 3.2. Symbol shapes indicate different redshift bins, while colours indicate stellar masses and sizes. Dotted lines show the boundaries used to define each group of stacked spectra. The dashed line shows the relationship that the early-type galaxies follow in the nearby Universe (Shen et al. 2003). Error bars over-plotted on the dashed line show the dispersion of this relationship.

stellar population (of 10 Gyr), we conclude that the error estimations in Table 1 represent acceptable values. Furthermore, it is worth noting that even if the errors were underestimated by this factor the conclusions of the present paper would be unaltered.

In Appendix B, we illustrate the PPXF fitting results for the stacked spectra to show the reliability of our spectral fits.

4 DISCREPANCY BETWEEN THE DYNAMICAL AND STELLAR MASSES

We start by comparing the dynamical masses computed using equation (7) with the stellar masses $M_\star$.

Most of the discrepancies between dynamical and stellar masses in the literature are reported in high-redshift studies. Thus, an immediate question arises: is this problem related to the redshift of the galaxies? Fig. 5 shows that there is not a clear trend between $M_\star/M_{\rm dyn}$ and redshift. This figure also shows that there are many galaxies in the forbidden region $M_\star/M_{\rm dyn} > 1$ (grey area in the figure). It is clearly seen that our compact galaxies (yellow and green triangles, squares and pentagons) have larger $M_\star/M_{\rm dyn}$ than our normal-sized galaxies (blue and red triangles, squares and

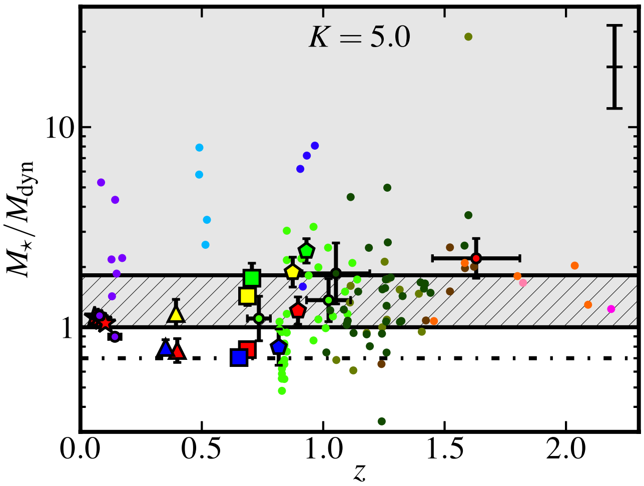

Figure 5. The $M_\star/M_{\rm dyn}$ ratio as a function of redshift. The grey region represents the unphysical area where $M_\star > M_{\rm dyn}$. The hatched region covers the sector where the discrepancy between the dynamical and stellar masses could be solved using a Chabrier IMF instead of a Salpeter IMF for the determination of the stellar masses. The dash–dotted line corresponds to a typical stellar/dynamical mass fraction (0.7, see Gavazzi et al. 2007). Symbols are as in Figs 3 and 4. For clarity, the SDSS NYU sample has been plotted to show the mean properties of SDSS galaxies after a redshift binning. The error bar in the top right corner of the figure represents the mean $M_\star/M_{\rm dyn}$ error of the individual galaxies. Redshift errors on individual galaxies are smaller than the symbols.

Table 1. Characteristics of the T07-DEEP2 DR4 stacked spectra.

ID (1)	$\langle z\rangle$ (2)	$\langle M_\star\rangle$ (10^{11} M$_\odot$) (3)	$\Delta\langle M_\star\rangle$ (dex) (4)	$\langle r_e\rangle$ (kpc) (5)	$\Delta\langle r_e\rangle$ (dex) (6)	$\langle n\rangle$ (7)	$N_{\rm stack}$ (8)	$(S/N)_{\rm rest}$ (Å^{-1}) (9)	$\sigma_{\rm e}$ (km s^{-1}) (10)	$\Delta\sigma_{\rm e}$ (km s^{-1}) (11)	$\sigma_{\rm e}^{\rm MC}$ (km s^{-1}) (12)	$\Delta\sigma_{\rm e}^{\rm MC}$ (km s^{-1}) (13)
z0.35MR	0.399	2.306	0.04	6.16	0.007	5.8	13	33.9	205	3	204	3
z0.35mR	0.351	1.188	0.012	4.11	0.009	6.0	10	26.6	177	4	180	3
z0.35mr	0.394	1.080	0.03	1.92	0.014	4.4	3	14.9	203	7	201	6
z0.65MR	0.688	2.316	0.02	4.87	0.006	5.5	42	23.9	230	3	230	3
z0.65Mr	0.706	2.080	0.05	1.80	0.010	4.7	7	10.3	238	5	238	6
z0.65mR	0.653	1.204	0.009	4.08	0.011	5.4	21	12.3	190	5	186	5
z0.65mr	0.688	1.147	0.02	1.77	0.015	5.3	16	14.8	198	7	199	6
z0.95MR	0.896	2.960	0.06	3.96	0.015	5.2	21	11.1	230	8	237	7
z0.95Mr	0.931	2.083	0.03	1.39	0.02	4.9	17	10.4	231	9	228	7
z0.95mR	0.817	1.223	0.03	4.33	0.04	4.2	4	5.6	175	17	209	20
z0.95mr	0.874	1.201	0.014	1.39	0.03	5.4	12	8.0	198	11	207	9

Notes to Table 1. (1) Identification associated with the stacked spectra. (2) Arithmetic mean redshift of the individual galaxies used in the stacked spectra. (3) Geometric mean stellar mass of the individual galaxies used in the stacked spectra. (4) Error of the geometric mean stellar mass. (5) Geometric mean effective (half-light) radius of the individual galaxies used in the stacked spectra. (6) Error of the geometric mean effective (half-light) radius. (7) Arithmetic mean Sérsic index of the individual galaxies used in the stacked spectra. (8) Number of stacked individual galaxies. (9) Mean rest-frame signal-to-noise ratio per angstrom of the stacked spectra in the region where the velocity dispersion was measured. (10) Velocity dispersion measured in the stacked spectra. (11) Error of the velocity dispersion measured in the stacked spectra. (12) Mean velocity dispersion measured in 100 Monte Carlo realizations of the stacked spectra. (13) Standard deviation of the velocity dispersion measured in 100 Monte Carlo realizations of the stacked spectra.

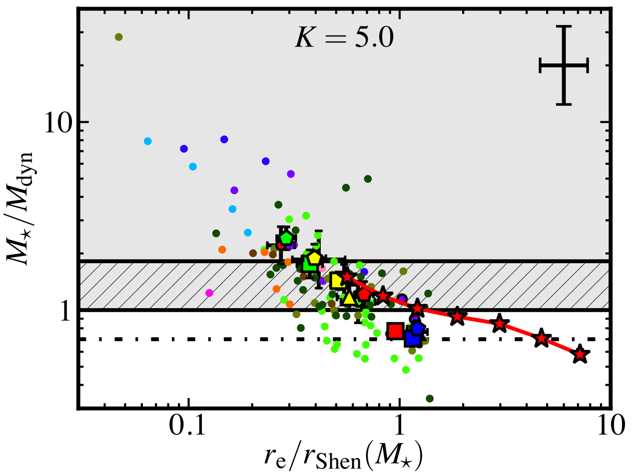

Figure 6. Correlation between the $M_\star/M_{\rm dyn}$ ratio and the compactness indicator $r_{\rm e}/r_{\rm Shen}(M_\star)$. The symbols, regions, dash–dotted line and cross in the top right corner are as in Fig. 5. For clarity, the SDSS NYU sample has been plotted to show the mean properties of SDSS galaxies after a binning in $r_{\rm e}/r_{\rm Shen}(M_\star)$.

pentagons). In addition, at low redshift the only conflicting values are the compact massive galaxies from Ferré-Mateu et al. (2012). Therefore, it is worthwhile to ask whether the $M_\star$–$M_{\rm dyn}$ problem is related to the compactness of the galaxies. This would explain why there is a trend to have more galaxies in the grey region at high redshifts in Fig. 5, as it could be connected with the strong size evolution of ETGs with redshift.

To check whether the source of the discrepancy between dynamical and stellar masses is the size of the objects, we need a criterion for measuring the compactness. In this work, we will employ the ratio $r_{\rm e}/r_{\rm Shen}(M_\star)$, where we define the function $r_{\rm Shen}(M_\star)$ as the mean effective (half-light) radius of an ETG in the nearby Universe. Specifically, $r_{\rm Shen}(M_\star)$ follows the equation

$$r_{\rm Shen}(M_\star) \equiv 2.88 \times 10^{-6}\ {\rm kpc} \left(\frac{0.62\ M_\star}{{\rm M}_\odot}\right)^{0.56}$$
$$= 3.185\ {\rm kpc} \left(\frac{M_\star}{10^{11}\ {\rm M}_\odot}\right)^{0.56}, \qquad (8)$$

where we have considered the fitting result from Shen et al. (2003), and have introduced the factor 0.62 to adapt the expression from these authors to a Salpeter IMF (Longhetti & Saracco 2009).

Fig. 6 plots the fraction $M_\star/M_{\rm dyn}$ versus the compactness indicator $r_{\rm e}/r_{\rm Shen}(M_\star)$. The correlation between the parameters represented in Fig. 6 is strong (the Spearman correlation coefficient is -0.75 for all data, and -0.85 for our data). To demonstrate the statistical significance of this correlation we performed two tests. First, we computed the two-tailed p-value for the Spearman correlation coefficient of all data and our data: 3×10^{-24} and 0.001 respectively. The second test was to calculate the probability of the null result, namely whether the distribution of the data is compatible with no relation. To estimate that, we calculated the minimum χ^2 value of a horizontal line fit to the data, and computed the probability of obtaining this or a higher χ^2 in an uncorrelated distribution with the same degrees of freedom. We did this for the individual data and for T07-DEEP2 DR4 data, obtaining values of 9×10^{-13} and 3×10^{-21} respectively. In addition, in this figure we can see that larger $M_\star/M_{\rm dyn}$ values are found in the most compact galaxies (with several points around a factor of 8 and an extreme data point at ∼30).

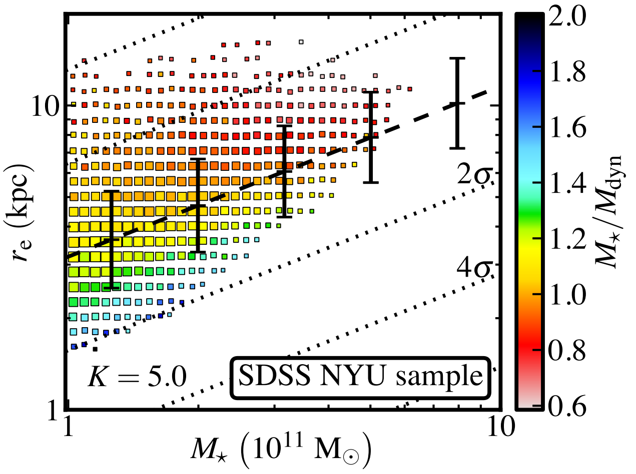

Figure 7. Dependence of the $M_\star/M_{\rm dyn}$ ratio on the position in the $M_\star$–$r_{\rm e}$ diagram for galaxies in the NYU sample of SDSS galaxies. The data have been binned depending on stellar mass and radius. The colour of each symbol indicates the $M_\star/M_{\rm dyn}$ ratio, while the size of each symbol scales with the number of galaxies in each bin. For clarity, bins with fewer than 10 galaxies have been omitted. The dashed line shows the relationship that the ETGs follow in the nearby Universe (Shen et al. 2003). Error bars over-plotted on the dashed line show the dispersion of this relationship. Dotted lines are parallels to the dashed line spaced by twice the mean dispersion of the relationship from Shen et al. (2003).

The large ratio between the two masses cannot be justified in terms of the weakest aspect of the stellar mass determination: the IMF. Many authors have argued that there is a systematic variation in the IMF in ETGs (Cappellari et al. 2012; Conroy & van Dokkum 2012; Ferreras et al. 2013). However, their results would enable us to apply a correction factor to each galaxy of between 0.5 and 2. This is clearly insufficient to reconcile the data with a physically interpretable result. Consequently, one can ask whether the determination of the dynamical mass is the origin of the discrepancy. At this point, note that the determination of $M_{\rm dyn}$ assumes the universality of the coefficient $K = 5.0$ of equation (7). This assumption is based on the homology hypothesis. However, several authors have convincingly argued that ETGs are non-homologous systems (see e.g. Bertin, Ciotti & Del Principe 2002; Cappellari et al. 2006).

We quantify non-homology effects in the next section. First, to reinforce our result that mass discrepancy correlates with compactness, we show in Fig. 7, using a large homogeneous sample of *nearby* galaxies, that the $M_\star/M_{\rm dyn}$ ratio increases as the galaxies become increasingly compact. Fig. 7 shows how the $M_\star/M_{\rm dyn}$ ratio varies with the position on the $M_\star$–$r_{\rm e}$ diagram using the data from the NYU sample of SDSS galaxies. We note that contours that share the same $M_\star/M_{\rm dyn}$ value tend to be parallel to the relationship that the ETGs follow in the nearby Universe (Shen et al. 2003) when $r_{\rm e}/r_{\rm Shen}(M_\star) < 1$. Above this relation, however, galaxies with similar $M_\star/M_{\rm dyn}$ values seem to depend only on the $r_{\rm e}$ value and not on the mass.

5 INTERPRETATION OF THE DISCREPANCY AS A NON-HOMOLOGY EFFECT

In this section, we interpret the discrepancy between $M_\star$ and $M_{\rm dyn}$ as a non-homology effect, and explain how the discrepancy can be solved using a variation of the K coefficient in equation (6).

The weak homology hypothesis proposes that deviations from homology are due to differences in the luminosity structure of

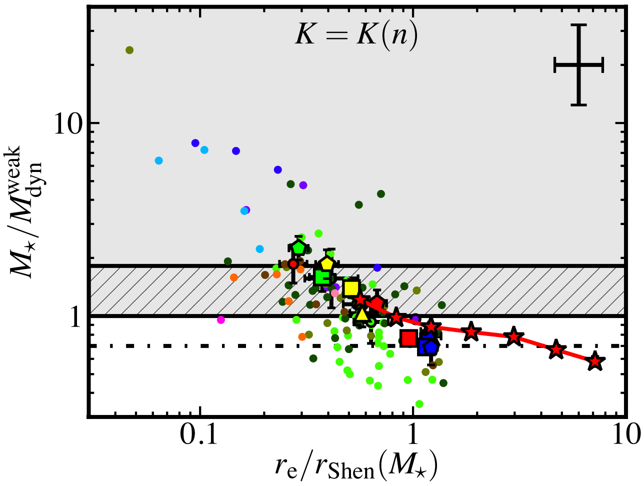

Figure 8. Correlation between the $M_\star/M_{\rm dyn}^{\rm weak}$ ratio and the compactness indicator $r_{\rm e}/r_{\rm Shen}(M_\star)$. $M_{\rm dyn}^{\rm weak}$ refers to the dynamical mass estimated with equation (6) and the weak homology hypothesis, namely a K coefficient that depends on the Sérsic index n. This figure uses the dependence of $K = K(n)$ measured by Cappellari et al. (2006). Symbols, regions, the dash–dotted line and the cross in the top right corner are as in Fig. 5. For clarity, the SDSS NYU sample has been plotted to show the mean properties of SDSS galaxies after a binning in $r_{\rm e}/r_{\rm Shen}(M_\star)$.

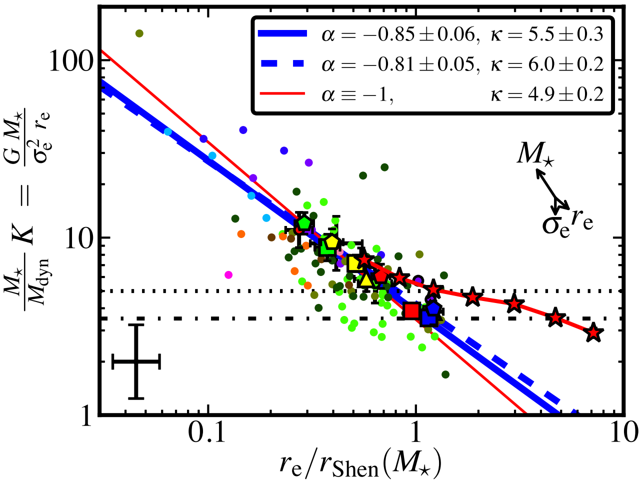

Figure 9. Dependence of $(M_\star/M_{\rm dyn})\,K$ on the compactness indicator $r_{\rm e}/r_{\rm Shen}(M_\star)$. The symbols are as in Figs 3 and 4. The dash–dotted black line corresponds to a typical stellar/dynamical mass fraction (0.7, see Gavazzi et al. 2007) and a K value of 5.0 (Cappellari et al. 2006). The dotted black line corresponds to $(M_\star/M_{\rm dyn})\,K = 5.0$. Assuming $K = 5.0$, above this line we have the unphysical situation $M_\star > M_{\rm dyn}$. The thick solid (dashed) blue line is a fit to all (our) data with the law $(M_\star/M_{\rm dyn})\,K = 0.7\,\kappa (r_{\rm e}/r_{\rm Shen}(M_\star))^\alpha$. The thin solid red line is a similar fit to all data on which the condition $\alpha \equiv -1$ has been imposed. For clarity, the SDSS NYU sample has been plotted to show the mean properties of SDSS galaxies after a binning in $r_{\rm e}/r_{\rm Shen}(M_\star)$. The error bar cross in the bottom left corner of the figure represents the mean error of the individual galaxies. The arrows in the right part of the figure indicate the shift that an individual point would have if we were to increase its $M_\star$, $r_{\rm e}$ or $\sigma_{\rm e}$ by the mean error on these variables of the individual galaxies.

galaxies. Indeed, different values of K are expected from galaxies with different Sérsic indices. Bertin et al. (2002) modelled this behaviour in their equation (11). Cappellari et al. (2006) quantified the dependence of K on n using their own sample (their equation 20):

$$K(n) = 8.87 - 0.831n + 0.0241n^2. \qquad (9)$$

The K values from Cappellari et al. (2006) are higher than those of Bertin et al. (2002), and hence come closer to resolving the mass discrepancy problem. We computed dynamical masses for our galaxies using equation (9), and in Fig. 8 plot $M_\star/M_{\rm dyn}$ against the compactness indicator $r_{\rm e}/r_{\rm Shen}(M_\star)$. Fig. 8 gives the mass discrepancy dependence assuming weak homology. Comparison with Fig. 6 shows that, while most points do shift down to lower values of $M_\star/M_{\rm dyn}$ (median drop of $\log(M_\star/M_{\rm dyn}) = 0.17$), the bulk of the galaxies remain in the unphysical region $M_\star/M_{\rm dyn} > 1$. Hence, weak homology does not resolve mass discrepancy.

Fig. 9 shows the dependence of $(M_\star/M_{\rm dyn})\,K$ on the compactness indicator $r_{\rm e}/r_{\rm Shen}(M_\star)$, where the first magnitude was calculated with the formula $(M_\star/M_{\rm dyn})\,K = (G\,M_\star)/(\sigma_{\rm e}^2\,r_{\rm e})$. Assuming $K = 5.0$, we drew two horizontal lines in Fig. 9 for the cases $(M_\star/M_{\rm dyn}) = 0.7$ (Gavazzi et al. 2007) and $(M_\star/M_{\rm dyn}) = 1$ (i.e. no dark matter within the luminous body). Many objects lie above the $(M_\star/M_{\rm dyn}) = 1$ boundary. This behaviour is not confined to high-redshift galaxies. Indeed, when $r_{\rm e}/r_{\rm Shen}(M_\star) < 1$, $M_\star > M_{\rm dyn}$ also for galaxies in the SDSS NYU sample if we assume $K = 5.0$. The range of variation of $(M_\star/M_{\rm dyn})\,K$ in Fig. 9 is ~1.5 dex, but an evolution from a stellar/dynamical mass fraction from 0.7 to 1 could only explain ~0.15 dex; in other words, the observed range of $(M_\star/M_{\rm dyn})\,K$ is far from being fully explained by an increase of $(M_\star/M_{\rm dyn})$ for compact galaxies. The correlation of Fig. 9 has to be dominated by a variation of K (its scatter may be given by galaxy-to-galaxy $M_\star/M_{\rm dyn}$ variations owing to, for example, orientation effects or differences in rotational support). The only alternative to the conclusion that K changes with compactness in Fig. 9 is that stellar mass determinations have large systematic errors *that scale with compactness*. In this section we assume that this is not the case, although we will return to discuss this possibility in our conclusions. Therefore, Fig. 9 indicates a variation in the structure or dynamics of galaxies with compactness, which translates into a K variation.

Can the so-called weak homology, where $K = K(n)$, explain the variation of K shown in Fig. 9? As shown in Fig. 8, this correction is much smaller than the value required to explain the range found in Fig. 9. This means that non-homology effects owing to compactness are prevailing over weak homology effects.

To characterize the dependence of K on galaxy compactness we fit a power law to the data in Fig. 9; that is,

$$\begin{aligned}\frac{M_\star}{M_{\rm dyn}}\,K &= 0.7\,\kappa \left(\frac{r_{\rm e}}{r_{\rm Shen}(M_\star)}\right)^{\alpha} \\ &= 0.7\,\kappa \left(\frac{r_{\rm e}}{3.185\ {\rm kpc}}\right)^{\alpha} \left(\frac{M_\star}{10^{11}\ {\rm M}_\odot}\right)^{-0.56\alpha}, \qquad (10)\end{aligned}$$

where α and κ are free parameters. α measures the logarithmic slope of K with the compactness, while κ is the value of K for a galaxy that is located in the $z = 0$ stellar mass–size relation with a typical stellar/dynamical mass fraction of 0.7. Making an orthogonal distance regression, all data are fitted with $\alpha = -0.85 \pm 0.06$ and $\kappa = 5.5 \pm 0.3$. The use of only our own data gives $\alpha = -0.81 \pm 0.05$ and $\kappa = 6.0 \pm 0.2$. We have plotted these two fits with solid and dashed thick blue lines, respectively, in Fig. 9. Given that the slope α in our fitting results is similar to -1, we also determined the κ parameter fixing $\alpha \equiv -1$, obtaining $\kappa = 4.9 \pm 0.2$ (this last fit is

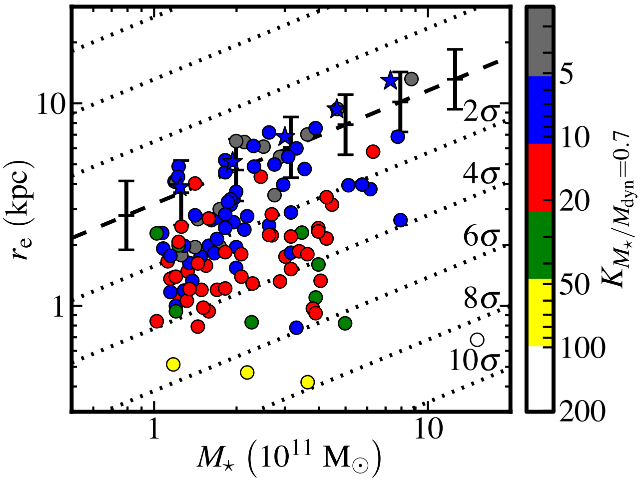

Figure 10. Variation of the K coefficient in the stellar mass–size plane. A typical stellar/dynamical mass fraction in the computation of K ($M_\star/M_\mathrm{dyn} = 0.7$) has been assumed. The dashed line shows the relationship that the early-type galaxies follow in the nearby Universe (Shen et al. 2003). Error bars over-plotted on the dashed line show the dispersion of this relationship. The dotted lines are parallels to the dashed line spaced by twice the mean dispersion of the relationship from Shen et al. (2003). For clarity, the SDSS NYU sample has been plotted to show the mean properties of SDSS galaxies after a stellar-mass binning and has been differentiated with star symbols.

plotted with a thin solid red line in Fig. 9). It is remarkable that all κ values are around the $K = 5.0$ value from Cappellari et al. (2006). This result is, however, expected because the galaxies employed by those authors in their K calibration were normal-sized ETGs in the $z = 0$ stellar mass–size relation.

Once we have assumed that the variation in Fig. 9 results mainly from a variation in K, Fig. 10 can be used to understand our results better. This figure shows the K value for each galaxy assuming a fiducial stellar/dynamical mass fraction equal to 0.7 over the stellar mass–size plane. The geometrical meaning of our compactness indicator $r_\mathrm{e}/r_\mathrm{Shen}(M_\star)$ and its relationship with K are clear in this figure: when the $M_\star$–M_dyn discrepancy is interpreted as a non-homology effect, it is the case that two galaxies are homologous (i.e. have the same K value) if and only if their stellar masses and sizes are in the same parallel line to the relationship that ETGs follow in the nearby Universe . In addition, this figure shows the growth of K as a power law of the departure from the $z = 0$ stellar mass–size relation. In the figure the departure from the $z = 0$ stellar mass–size relation is characterized using the dispersion of this relation (which has the value 0.154 dex on r_e axis). In addition, this figure emphasizes that the galaxies in the $z = 0$ stellar mass–size relation are characterized by having the same value of the structural parameter K ($K \sim 5$).

Another way of illustrating the departure from homology (i.e. the variation of K) as a function of the compactness is shown in Fig. 11. Using the NYU sample of SDSS galaxies, we plot the velocity dispersion of the galaxies versus their effective radii. We have split the sample into different stellar-mass bins. Fig. 11 shows that galaxies with a similar stellar mass do not follow the homology hypothesis (i.e. their σ_e is not proportional to $\sqrt{r_\mathrm{e}}$). Interestingly, the departure from homology is larger when the sizes of galaxies are smaller.

Finally, we provide a *rough* approximation to the K coefficient as a function of the compactness $r_\mathrm{e}/r_\mathrm{Shen}(M_\star)$ using the following expression:

$$\begin{aligned} K &\sim 6.0 \left(\frac{r_\mathrm{e}}{r_\mathrm{Shen}(M_\star)} \right)^{-0.81} \\ &= 6.0 \left(\frac{r_\mathrm{e}}{3.185\ \mathrm{kpc}} \right)^{-0.81} \left(\frac{M_\star}{10^{11}\ \mathrm{M}_\odot} \right)^{0.45}. \end{aligned} \tag{11}$$

This approximation is based on the fit to our data in Fig. 9, and assumes a fiducial stellar/dynamical mass fraction of approximately 0.7 and a Salpeter IMF. We note that equation (11) should be

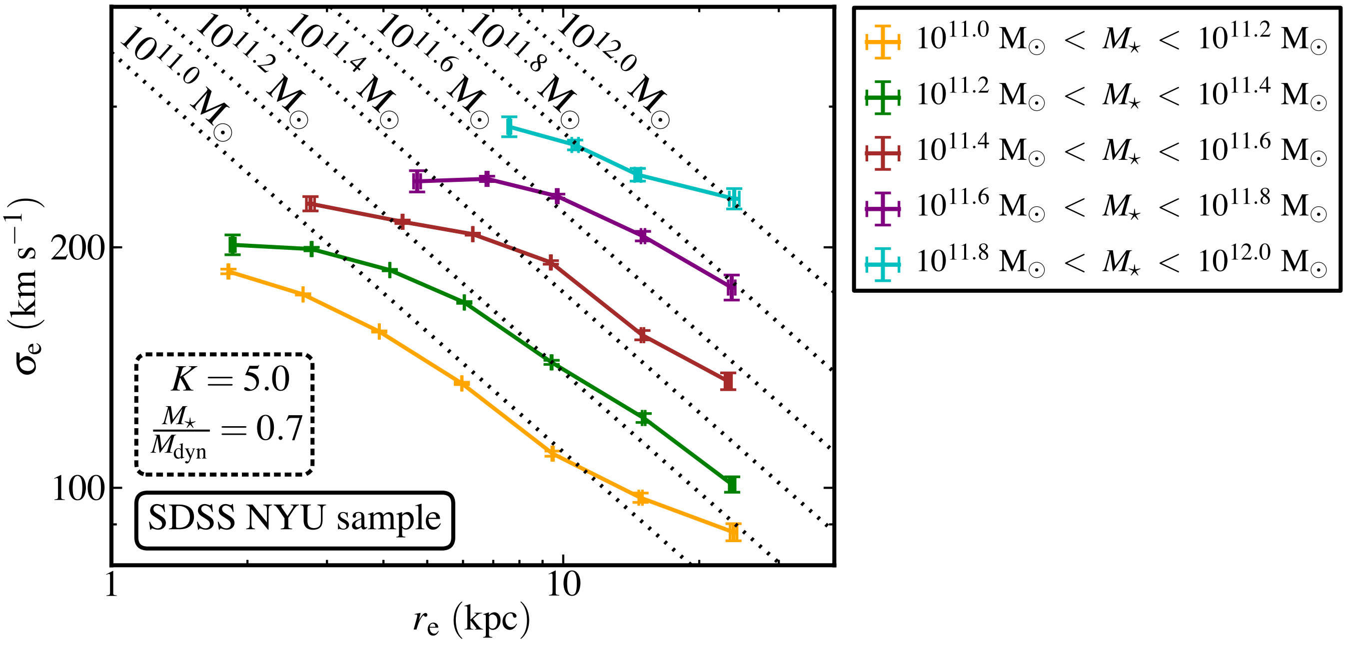

Figure 11. The relationship between σ_e and r_e the NYU sample of SDSS galaxies. The SDSS NYU data depart from the expectation of the virial theorem when the homology hypothesis is assumed (i.e. $\sigma_\mathrm{e} \propto \sqrt{r_\mathrm{e}}$). The dotted lines show the prediction for various stellar mass ranges. We have assumed $K = 5.0$ and $M_\star/M_\mathrm{dyn} = 0.7$ for this prediction.

used only as an estimation within a factor of a few of the K coefficient. If compact massive galaxies are strongly dominated by dark matter, namely if they have stellar/dynamical mass fractions lower than $\sim$0.3, equation (11) has to be interpreted as a lower limit to the K coefficient.

As a result of the dependence of K on $r_{\rm e}$ and $M_\star$ (equation 11) and using $M_\star = 0.7\,M_{\rm dyn}$, the dynamical mass adopts the following dependence on $r_{\rm e}$ and $\sigma_{\rm e}$:

$$M_{\rm dyn} \sim \left[7.5 \left(\frac{\sigma_{\rm e}}{200\ {\rm km\ s^{-1}}}\right)^{1.6} \left(\frac{r_{\rm e}}{3\ {\rm kpc}}\right)^{-0.65}\right] \frac{\sigma_{\rm e}^2 r_{\rm e}}{G}$$
$$= \left(\frac{\sigma_{\rm e}}{200\ {\rm km\ s^{-1}}}\right)^{3.6} \left(\frac{r_{\rm e}}{3\ {\rm kpc}}\right)^{0.35} 2.1 \times 10^{11}\ {\rm M_\odot}, \qquad (12)$$

which highlights that the dependence of $M_{\rm dyn}$ on $r_{\rm e}$ and $\sigma_{\rm e}$ strongly departs from the homology-virial theorem prediction (i.e. $M_{\rm dyn} \propto \sigma_{\rm e}^2 r_{\rm e}$, equation 6 with K independent of $\sigma_{\rm e}$ and $r_{\rm e}$). We emphasize again that equation (12) should only be used as an estimate within a factor of a few of the dynamical mass. Regarding the two factors contributing to the mass discrepancy shown in Fig. 9, equation (12) has corrected the dominant factor, namely compactness, by positing a shallow dependence of $M_{\rm dyn}$ on radius ($\propto r_{\rm e}^{0.35}$). However, our formula does not address the other factor contributing to mass discrepancy, namely $M_\star/M_{\rm dyn}$, because, by construction, equation (12) gives dynamical masses that fulfil $M_\star/M_{\rm dyn} \sim 0.7$. Still, equation (12) should be useful because the expected departures from $M_\star/M_{\rm dyn} = 0.7$ are small. Therefore, for a galaxy near to $M_\star/M_{\rm dyn} \sim 0.7$, equation (12) approximates the dynamical mass. Conversely, when the baryon density is significantly lower than the dark matter density ($M_\star/M_{\rm dyn} < 0.3$), equation (12) should be considered as a lower limit to the dynamical mass. It is possible to devise corrections to equation (12) if independent information on the behaviour of $M_\star/M_{\rm dyn}$ is available.

A question that arises is whether in massive compact galaxies the ratio $M_\star/M_{\rm dyn}$ (within $\sim$1 $r_{\rm e}$) significantly departs from the value $M_\star/M_{\rm dyn} = 0.7$ found by Gavazzi et al. (2007). Two-dimensional spectroscopy of compact galaxies, followed by dynamical modelling, will provide the answer to this question. Our guess is that, if anything, $M_\star/M_{\rm dyn}$ within the luminous effective radius is higher in an ultra-dense galaxy than in a normal galaxy, given the strongly dissipative processes that must occur in order for the galaxies to reach their high densities. Under this hypothesis, equation (12) should provide a good approximation to the dynamical mass.

6 DISCUSSION

The family of ETGs may depart from homology (non-constant K in equation 6) through differences in their internal structure, their internal dynamics and/or the contribution of dark matter to their gravitational potential. Structural non-homology is expected, given that the surface brightness profiles of ETGs show a range of Sérsic indices n; Bertin et al. (2002) provide the dependence of K on n. The internal dynamical structure of massive compact galaxies is also expected to differ from that of normal-sized massive galaxies: while the formation of massive compact galaxies must have involved a strongly dissipative collapse, normal-sized $z = 0$ massive ellipticals owe their internal dynamics to a history of dissipationless mergers (see e.g. Trujillo, Ferreras & de La Rosa 2011). Minor mergers, thought to be the dominant mechanism for the size evolution of massive compact galaxies, imply non-violent relaxation that leaves the remnant in a state far from equipartition per unit mass, whereas mixing is more pronounced in major mergers. A further clue that the internal dynamics of massive compact galaxies differs from that of normal-sized ellipticals is provided by the fact that these objects show elongated shapes (Ferré-Mateu et al. 2012; Trujillo et al. 2014); that is, they have disc-like shapes. At high redshifts, this has been confirmed by van der Wel et al. (2012) and Buitrago et al. (2013b) among others. This fact may suggest an increase of the rotational contribution to the dynamical structure of these objects (Buitrago et al. 2014).

We emphasize that our arguments leading to a conclusion of non-homology would be compromised if stellar mass estimates were shown to have large, systematic errors that scale with galaxy compactness. It remains, therefore, to seek clues on non-homology that are independent of stellar mass determinations, using deep two-dimensional spectroscopy of nearby massive compact galaxies to constrain Jeans or Schwarzschild modelling (for example, it would be interesting to undertake a detailed study of the objects in van den Bosch et al. 2012).

7 CONCLUSIONS

In what follows we summarize the main results of this paper.

First, the degree to which the ratio of stellar to dynamical masses is unphysical ($M_\star/M_{\rm dyn} > 1$) is related to the compactness of the galaxies, not to redshift (Figs 5 and 6). For most compact galaxies, the mass discrepancy is too large to be caused by the uncertainties in the IMF, arguably the weakest point in the determination of the total mass of a stellar population. Other uncertainties in the stellar mass determination cannot lead to a reconciliation of the two mass estimators either. The disagreement is too large to be explained by a variation in the dark matter fraction. Therefore, either (i) there exists an unknown large *systematic* error in stellar masses linked to galaxy compactness, or (ii) there is a violation of the homology hypothesis in massive compact galaxies.

Second, when we interpret the $M_\star$–$M_{\rm dyn}$ discrepancy in terms of non-homology, namely as a variation of the coefficient K from the virial theorem (equation 6), the value of K reaches up to $\sim$40 for several compact galaxies (eight times greater than the value found by Cappellari et al. 2006). This strong variation in K is well modelled as $K \propto (r_{\rm e}/r_{\rm Shen}(M_\star))^\alpha$ with $\alpha \simeq -0.8$.

Finally, owing to the dependence of K on $r_{\rm e}$ and $M_\star$, the dynamical mass scales with $\sigma_{\rm e}$ and $r_{\rm e}$ as $M_{\rm dyn} \propto \sigma_{\rm e}^{3.6} r_{\rm e}^{0.35}$, hence departing from homology and the virial theorem-based scaling $M_{\rm dyn} \propto \sigma_{\rm e}^2 r_{\rm e}$. Equation (12) provides an approximation to estimate $M_{\rm dyn}$ for galaxies with $M_\star/M_{\rm dyn} \sim 0.7$, and is a lower limit for galaxies strongly dominated by dark matter (i.e. $M_\star/M_{\rm dyn} < 0.3$).

ACKNOWLEDGEMENTS

We are grateful to the referee for his/her constructive comments, which helped to improve the manuscript. The authors thank A. Ferré-Mateu, A. Vazdekis, J. Sánchez Almeida, M. Cappellari, E. Mármol-Queraltó, I. G. de La Rosa, A. de Lorenzo-Cáceres, R. C. E. van den Bosch, F. Shankar, F. Buitrago, A. Stockton and the *Traces of Galaxy Formation* group (http://www.iac.es/project/traces) for their comments during the development of this paper. LPdA is supported by the FPI Program by the Spanish Ministry of Science and Innovation. LPdA would like to thank I. Martín-Navarro for fruitful discussions, and V. Alí-Lagoa, L. Toribio San Cipriano and B. González-Merino and C. López-Sanjuan for comments that helped to improve the presentation of our results. JF-B acknowledges support from the Ramón y Cajal Program from the Spanish Ministry of Science and Innovation, as well as from the FP7 Marie Curie Actions of the European Commission, via the Initial Training Network DAGAL under REA grant agreement number 289313. This work was supported by the Programa Nacional de Astronomía y Astrofísica of the Spanish Ministry of Science and Innovation under the grants AYA2009-11137 and AYA2010-21322-C03-02. This research made use of ASTROPY, a community-developed core PYTHON package for Astronomy (Astropy Collaboration et al. 2013). Funding for the DEEP2 Galaxy Redshift Survey was provided by NSF grants AST-95-09298, AST-0071048, AST-0507428 and AST-0507483 as well as by NASA LTSA grant NNG04GC89G. We acknowledge the usage in pPXF of the MPFIT routine from Markwardt (2009).

REFERENCES

Astropy Collaboration et al., 2013, A&A, 558, A33
Belli S., Newman A. B., Ellis R. S., 2014, ApJ, 783, 117
Bertin G., Ciotti L., Del Principe M., 2002, A&A, 386, 149
Bezanson R., van Dokkum P., van de Sande J., Franx M., Kriek M., 2013, ApJ, 764, L8
Blakeslee J. P. et al., 2006, ApJ, 644, 30
Blanton M. R., Roweis S., 2007, AJ, 133, 734
Blanton M. R. et al., 2005, AJ, 129, 2562
Buitrago F., Trujillo I., Conselice C. J., Bouwens R. J., Dickinson M., Yan H., 2008, ApJ, 687, L61
Buitrago F., Trujillo I., Conselice C. J., Häußler B., 2013, MNRAS, 428, 1460
Buitrago F., Conselice C. J., Epinat B., Bedregal A. G., Grutzbauch R., 2014, MNRAS, preprint (arXiv:1305.0268)
Cappellari M., Emsellem E., 2004, PASP, 116, 138
Cappellari M. et al., 2006, MNRAS, 366, 1126
Cappellari M. et al., 2009, ApJ, 704, L34
Cappellari M. et al., 2012, Nature, 484, 485
Cenarro A. J., Trujillo I., 2009, ApJ, 696, L43
Cimatti A. et al., 2008, A&A, 482, 21
Coil A. L., Newman J. A., Kaiser N., Davis M., Ma C.-P., Kocevski D. D., Koo D. C., 2004, ApJ, 617, 765
Conroy C., van Dokkum P. G., 2012, ApJ, 760, 71
Conroy C., Gunn J. E., White M., 2009, ApJ, 699, 486
Daddi E. et al., 2005, ApJ, 626, 680
Davis M. et al., 2003, SPIE, 4834, 161
Davis M. et al., 2007, ApJ, 660, L1
Djorgovski S., de Carvalho R., Han M.-S., 1988, in Pritchet C. J., van der Bergh S., eds, ASP Conf. Ser. Vol. 4, The extragalactic distance scale. Astron. Soc. Pac., San Francisco, p. 329
Faber S. M. et al., 2003, SPIE, 4841, 1657
Falcón-Barroso J. et al., 2011, MNRAS, 417, 1787
Ferré-Mateu A., Vazdekis A., Trujillo I., Sánchez-Blázquez P., Ricciardelli E., de la Rosa I. G., 2012, MNRAS, 423, 632
Ferreras I., La Barbera F., de la Rosa I. G., Vazdekis A., de Carvalho R. R., Falcón-Barroso J., Ricciardelli E., 2013, MNRAS, 429, L15
Gavazzi R., Treu T., Rhodes J. D., Koopmans L. V. E., Bolton A. S., Burles S., Massey R. J., Moustakas L. A., 2007, ApJ, 667, 176
Le Borgne D., Rocca-Volmerange B., Prugniel P., Lançon A., Fioc M., Soubiran C., 2004, A&A, 425, 881
Longhetti M., Saracco P., 2009, MNRAS, 394, 774
Longhetti M. et al., 2007, MNRAS, 374, 614
Markwardt C. B., 2009, in Bohlender D. A., Durand D., Dowler P., eds, ASP Conf. Ser. Vol. 411, Astronomical Data Analysis Software and Systems XVIII. Astron. Soc. Pac., San Francisco, p. 251
Martinez-Manso J. et al., 2011, ApJ, 738, L22
Muzzin A., Marchesini D., van Dokkum P. G., Labbé I., Kriek M., Franx M., 2009, ApJ, 701, 1839
Newman A. B., Ellis R. S., Treu T., Bundy K., 2010, ApJ, 717, L103
Newman J. A. et al., 2013, ApJS, 208, 5
Onodera M. et al., 2012, ApJ, 755, 26
Poggianti B. M. et al., 2013, ApJ, 762, 77
Prugniel P., Soubiran C., Koleva M., Le Borgne D., 2007, preprint (astro-ph/0703658)
Ravindranath S. et al., 2004, ApJ, 604, L9
Satoh C., 1980, PASJ, 32, 41
Schiavon R. P. et al., 2006, ApJ, 651, L93
Schwarzschild M., 1979, ApJ, 232, 236
di Serego Alighieri S. et al., 2005, A&A, 442, 125
Shen S., Mo H. J., White S. D. M., Blanton M. R., Kauffmann G., Voges W., Brinkmann J., Csabai I., 2003, MNRAS, 343, 978
Stevenson C. C., 1994, MNRAS, 267, 904
Stockton A., Shih H.-Y., Larson K., 2010, ApJ, 709, L58
Stockton A., Shih H.-Y., Larson K., Mann A. W., 2014, ApJ, 780, 134
Taylor E. N., Franx M., Glazebrook K., Brinchmann J., van der Wel A., van Dokkum P. G., 2010, ApJ, 720, 723
Toft S. et al., 2007, ApJ, 671, 285
Toft S., Gallazzi A., Zirm A., Wold M., Zibetti S., Grillo C., Man A., 2012, ApJ, 754, 3
Trujillo I. et al., 2006, MNRAS, 373, L36
Trujillo I., Conselice C. J., Bundy K., Cooper M. C., Eisenhardt P., Ellis R. S., 2007, MNRAS, 382, 109 (T07)
Trujillo I., Cenarro A. J., de Lorenzo-Cáceres A., Vazdekis A., de la Rosa I. G., Cava A., 2009, ApJ, 692, L118
Trujillo I., Ferreras I., de La Rosa I. G., 2011, MNRAS, 415, 3903
Trujillo I., Ferré-Mateu A., Balcells M., Vazdekis A., Sánchez-Blázquez P., 2014, ApJ, 780, L20
van de Sande J. et al., 2013, ApJ, 771, 85
van den Bosch R. C. E., Gebhardt K., Gültekin K., van de Ven G., van der Wel A., Walsh J. L., 2012, Nature, 491, 729
van der Wel A., Franx M., van Dokkum P. G., Rix H.-W., Illingworth G. D., Rosati P., 2005, ApJ, 631, 145
van der Wel A., Holden B. P., Zirm A. W., Franx M., Rettura A., Illingworth G. D., Ford H. C., 2008, ApJ, 688, 48
van der Wel A. et al., 2012, ApJS, 203, 24
van Dokkum P. G., Kriek M., Franx M., 2009, Nature, 460, 717
Zirm A. W. et al., 2007, ApJ, 656, 66

APPENDIX A: ROBUSTNESS OF THE ERROR DETERMINATION IN THE VELOCITY DISPERSION MEASUREMENTS OF THE STACKED SPECTRA

As an independent check of the accuracy of the velocity dispersion errors delivered by pPXF for our T07-DEEP2 DR4 spectra, we ran a set of simulations with synthetic spectra to directly measure errors and their dependence on the signal-to-noise ratio and on velocity dispersion.

We first generated a grid of synthetic spectra as follows. We selected a spectrum of a single stellar population of age 10 Gyr and solar metallicity from the PEGASE library (Le Borgne et al. 2004). We chose this age because deriving velocity dispersions from spectra of this age is particularly challenging, and chose the solar metallicity as a good approximation to the metallicities of the galaxies under study. We degraded its spectral resolution to $R = 5900$, the same as the DEEP2 DR4 spectra, and degraded its velocity scale to 13 km s^{-1} pixel^{-1}, a mean value of the T07-DEEP2 DR4 spectra at rest-frame. This adapted spectrum was convolved with Gaussian kernels to obtain 201 broadened versions of the spectrum corresponding to velocity dispersions from 140 to 260 km s^{-1} with a step of 0.6 km s^{-1}. With each one of these 201 spectra we built an additional 61 spectra, adding white noise to obtain spectra with a signal-to-noise ratio from 2.5 to 20.5 pixel^{-1} (separated by 0.3 pixel^{-1}). We finally limited their spectral range from 4100 to 5800 Å, a representative range of the T07-DEEP2 DR4 spectra at rest-frame. We thus obtained a grid of 12 261 spectra with 201 velocity dispersions and 61 signal-to-noise ratios.

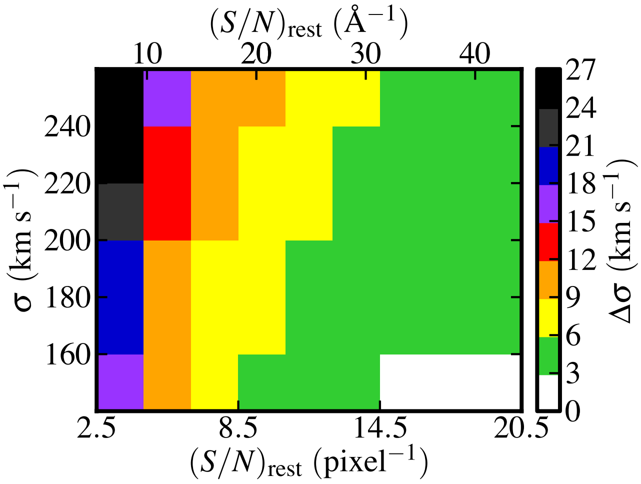

Figure A1. Grid of velocity dispersion deviations from the simulation described in Appendix A as a function of the signal-to-noise ratio and the input velocity dispersion. For clarity, we have binned the data according to their signal-to-noise ratio and σ and computed the standard deviation.

In the next step, we measured the velocity dispersion at each point of the spectral grid; that is, we ran pPXF over 100 Monte Carlo realizations of each spectrum. In the pPXF executions, we used as input parameter the same 82-star spectral library that we used in Section 3.3 for fitting the T07-DEEP2 DR4 stacked spectra. We computed the deviation at each point as the difference between the mean value of these measurements and the input velocity dispersion (known from the spectral grid generation step). We thus obtained a grid of velocity dispersion deviations at different velocity dispersions and signal-to-noise ratios. Fig. A1 summarizes our results for this grid.

Table A1. Comparison between different ways of estimating the velocity dispersion errors in the T07-DEEP2 DR4 stacked spectra.

ID (1)	$\Delta\sigma_{\rm e}$ (km s^{-1}) (2)	$\Delta\sigma_{\rm e}^{\rm MC}$ (km s^{-1}) (3)	$\Delta\sigma_{\rm simul}^{\rm MC}$ (km s^{-1}) (4)
z0.35MR	3	3	4
z0.35mR	4	3	5
z0.35mr	7	6	9
z0.65MR	3	3	7
z0.65Mr	5	6	17
z0.65mR	5	5	11
z0.65mr	7	6	9
z0.95MR	8	7	16
z0.95Mr	9	7	17
z0.95mR	17	20	25
z0.95mr	11	9	19

Notes to Table A1. (1) Identification associated with the stacked spectra (from Table 1). (2) Error of the velocity dispersion measured in the stacked spectra (from Table 1). (3) Standard deviation of the velocity dispersion measured in 100 Monte Carlo realizations of the stacked spectra (from Table 1). (4) Error of the velocity dispersion obtained from the simulation described in Appendix A.

In the last step, we estimated the velocity dispersion errors of each T07-DEEP2 DR4 spectrum. We computed these errors as the standard deviation of the grid velocity dispersion deviations inside a box of size 30 km s^{-1} × 2 pixel^{-1} around the centre of T07-DEEP2 DR4 spectral properties. In Table A1, we show the comparison between different ways of estimating the velocity dispersion errors in the T07-DEEP2 DR4 stacked spectra, including the results obtained in this last step.

APPENDIX B: FITTING RESULTS FOR THE STACKED SPECTRA

We illustrate in Figs B1, B2 and B3 the pPXF fitting results for the stacked spectra described in Section 3.3 to show the accuracy of the pPXF spectral fitting.

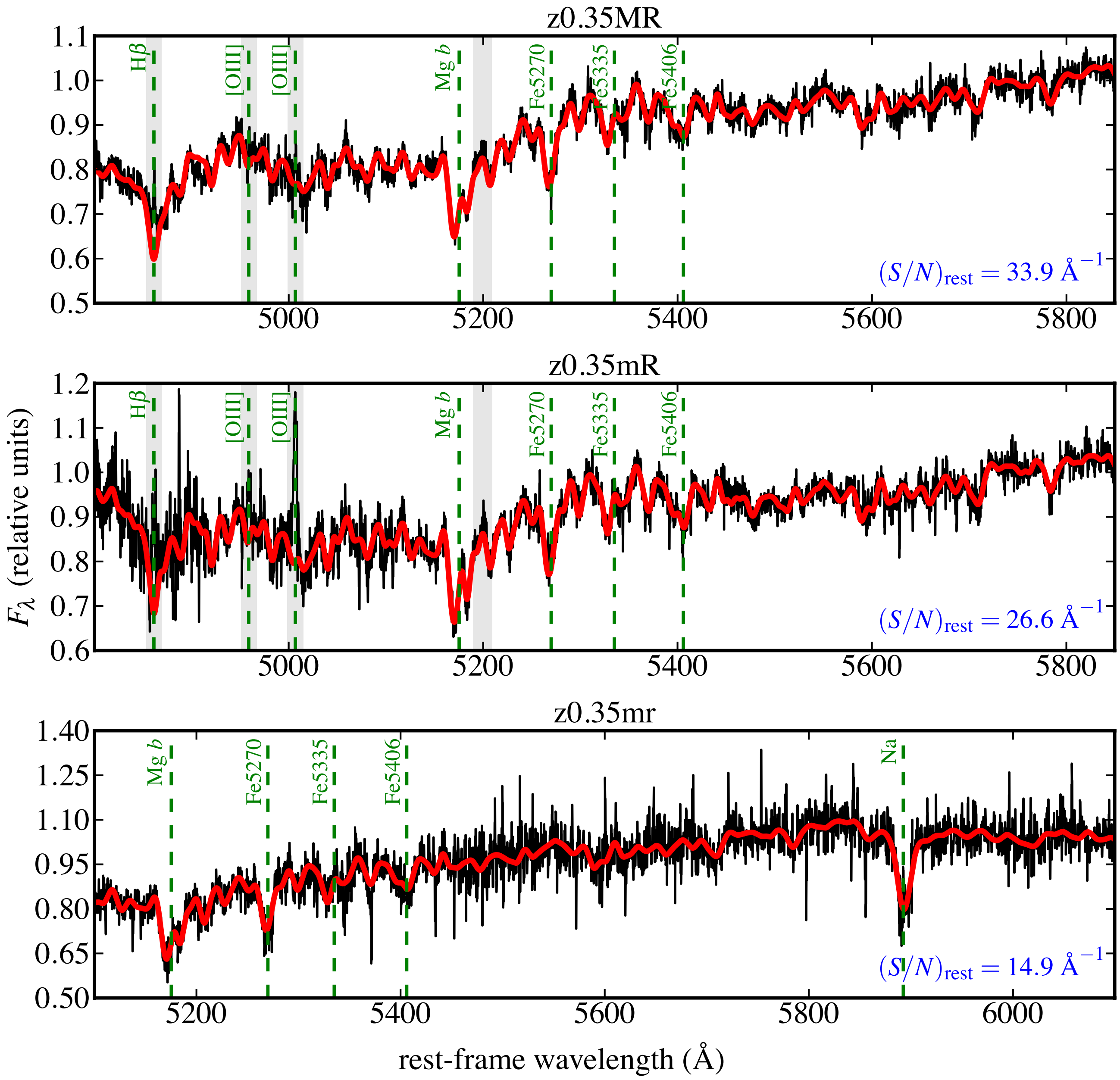

Figure B1. pPXF fitting results for the stacked spectra in the redshift bin $0.2 < z < 0.5$. The black solid lines represent our stacked spectra. Red thick solid lines are the pPXF fits. Masked regions in the pPXF fit are highlighted in grey. Some spectral features are marked with green dashed lines for visual clarity. Black labels above each panel are the stacked spectrum IDs from Table 1. Blue labels in the bottom right corner of each panel indicate the mean rest-frame signal-to-noise ratio per angstrom of the stacked spectra in the region where the velocity dispersion was measured.

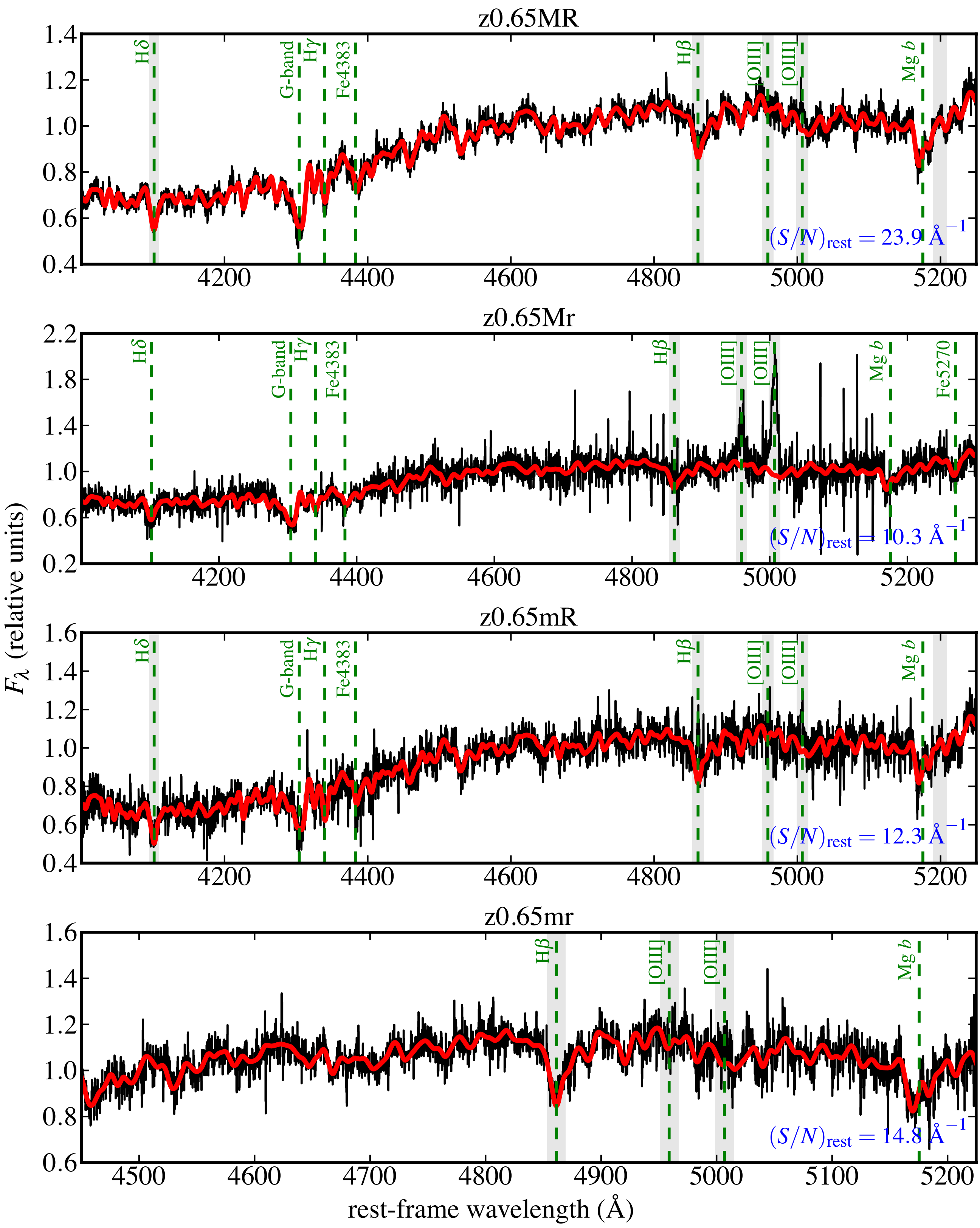

Figure B2. pPXF fitting results for the stacked spectra in the redshift bin $0.5 < z < 0.8$. The black solid lines represent our stacked spectra. Red thick solid lines are the pPXF fits. Masked regions in the pPXF fit are highlighted in grey. Some spectral features are marked with green dashed lines for visual clarity. Black labels above each panel are the stacked spectrum IDs from Table 1. Blue labels in the bottom right corner of each panel indicate the mean rest-frame signal-to-noise ratio per angstrom of the stacked spectra in the region where the velocity dispersion was measured.

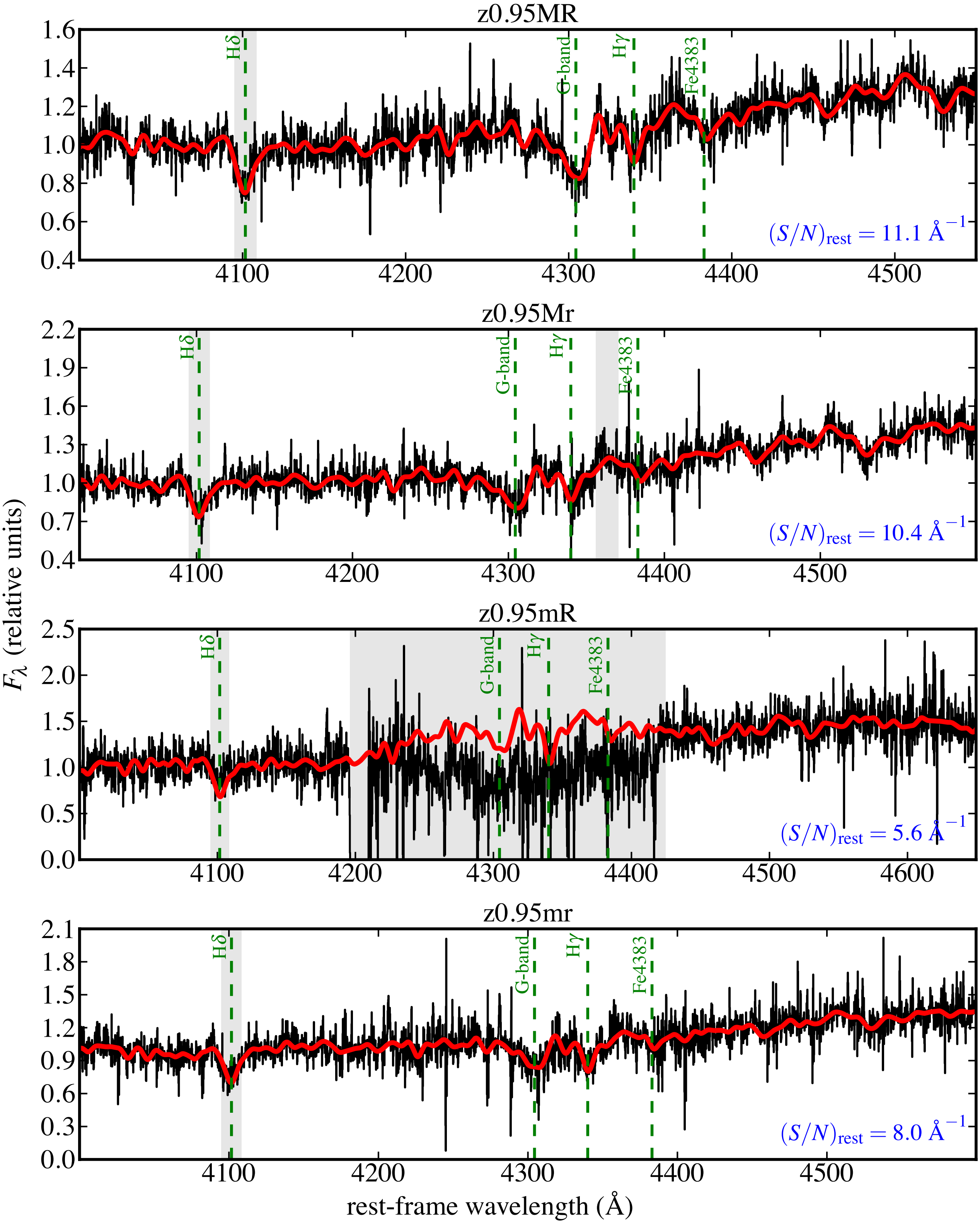

Figure B3. pPXF fitting results for the stacked spectra in the redshift bin $0.8 < z < 1.1$. The black solid lines represent our stacked spectra. Red thick solid lines are the pPXF fits. Masked regions in the pPXF fit are highlighted in grey. Some spectral features are marked with green dashed lines for visual clarity. Black labels above each panel are the stacked spectrum IDs from Table 1. Blue labels in the bottom right corner of each panel indicate the mean rest-frame signal-to-noise ratio per angstrom of the stacked spectra in the region where the velocity dispersion was measured.

This paper has been typeset from a TEX/LATEX file prepared by the author.

4

Constraints on the evolutionary mechanisms of massive galaxies since $z \sim 1$ from their velocity dispersions

The material included in this chapter has already been published by Peralta de Arriba et al. (2015). This article has been accepted for publication in Monthly Notices of the Royal Astronomical Society ©: 2015 L. Peralta de Arriba, M. Balcells, I. Trujillo, J. Falcón-Barroso, T. Tapia, N. Cardiel, J. Gallego, R. Guzmán, A. Hempel, I. Martín-Navarro, P. G. Pérez-González and P. Sánchez-Bláquez. Published by Oxford University Press on behalf of the Royal Astronomical Society. All rights reserved.

DOI: 10.1093/mnras/stv1579

Constraints on the evolutionary mechanisms of massive galaxies since $z \sim 1$ from their velocity dispersions

L. Peralta de Arriba,[1,2⋆] M. Balcells,[1,2,3] I. Trujillo,[1,2] J. Falcón-Barroso,[1,2] T. Tapia,[4]
N. Cardiel,[5] J. Gallego,[5] R. Guzmán,[6] A. Hempel,[7] I. Martín-Navarro,[1,2]
P. G. Pérez-González[5] and P. Sánchez-Bláquez[8]

[1] *Instituto de Astrofísica de Canarias (IAC), E-38205 La Laguna, Tenerife, Spain*
[2] *Universidad de La Laguna, Departamento de Astrofísica, E-38206 La Laguna, Tenerife, Spain*
[3] *Isaac Newton Group of Telescopes, E-38700 Santa Cruz de La Palma, La Palma, Spain*
[4] *Instituto de Astronomía, Universidad Nacional Autónoma de México, Apdo. 877, Ensenada BC 22800, Mexico*
[5] *Departamento de Astrofísica y Ciencias de la Atmósfera, Universidad Complutense de Madrid, E-28040 Madrid, Spain*
[6] *Department of Astronomy, University of Florida, PO Box 112055, Gainesville, FL 32611, USA*
[7] *Departamento de Ciencias Físicas, Universidad Andrés Bello, Av. República 252, Santiago, Chile*
[8] *Departamento de Física Teórica, Universidad Autónoma de Madrid, E-28049 Cantoblanco, Madrid, Spain*

Accepted 2015 July 13. Received 2015 July 9; in original form 2015 April 1

ABSTRACT

Several authors have reported that the dynamical masses of massive compact galaxies ($M_\star \gtrsim 10^{11}$ M$_\odot$, $r_\mathrm{e} \sim 1$ kpc), computed as $M_\mathrm{dyn} = 5.0\,\sigma_\mathrm{e}^2 r_\mathrm{e}/G$, are lower than their stellar masses $M_\star$. In a previous study from our group, the discrepancy is interpreted as a breakdown of the assumption of homology that underlie the M_dyn determinations. Here, we present new spectroscopy of six redshift $z \approx 1.0$ massive compact ellipticals from the Extended Groth Strip, obtained with the 10.4 m Gran Telescopio Canarias. We obtain velocity dispersions in the range 161–340 km s^{-1}. As found by previous studies of massive compact galaxies, our velocity dispersions are lower than the virial expectation, and all of our galaxies show $M_\mathrm{dyn} < M_\star$ (assuming a Salpeter initial mass function). Adding data from the literature, we build a sample covering a range of stellar masses and compactness *in a narrow redshift range $z \approx 1.0$*. This allows us to exclude systematic effects on the data and evolutionary effects on the galaxy population, which could have affected previous studies. We confirm that mass discrepancy scales with galaxy compactness. We use the stellar mass plane ($M_\star$, σ_e, r_e) populated by our sample to constrain a generic evolution mechanism. We find that the simulations of the growth of massive ellipticals due to mergers agree with our constraints and discard the assumption of homology.

Key words: galaxies: elliptical and lenticular, cD – galaxies: evolution – galaxies: fundamental parameters – galaxies: high-redshift – galaxies: kinematics and dynamics – galaxies: structure.

1 INTRODUCTION

The vast majority of early-type galaxies (ETGs) can safely be assumed to be in a steady stationary state. For these systems, the virial theorem holds, hence total potential and kinetic energies are balanced, such that

$$\frac{GM}{\langle r\rangle_\tau} = k_E\,\frac{\langle v^2\rangle_\tau}{2}, \tag{1}$$

where M is the dynamical mass, G is the gravitational constant, $\langle r\rangle_\tau$ is the mean of the stellar distances to the centre of the system at time τ, $\langle v^2\rangle_\tau$ is twice the kinetic energy of the system per unit mass at time τ and $k_E = 2$ is the virialization constant.

Under the condition of structural and kinematical homology, we have $\langle r\rangle_\tau \propto r_\mathrm{e}$ and $\langle v^2\rangle_\tau \propto \sigma_\mathrm{e}^2$; we then expect that ETGs verify relationships such as $M \propto \sigma_\mathrm{e}^2 r_\mathrm{e}$ and, wherever stellar mass dominates over dark matter, $M_\star \propto \sigma_\mathrm{e}^2 r_\mathrm{e}$; here $M_\star$ is the stellar mass (computed from population synthesis modelling), r_e is the effective (projected half-light) radius and σ_e is the luminosity-weighted second moment of the line-of-sight velocity distribution (LOSVD; hereafter, velocity dispersion).

⋆ E-mail: lperalta@iac.es

Cappellari et al. (2006, 2013) used Jeans and Schwarzschild modelling to provide a calibration of the dynamical mass for massive elliptical and lenticular galaxies in the nearby Universe, such that

$$M_{\rm dyn} \equiv 2 \times M_{1/2} = 5.0\,\frac{\sigma_{\rm e}^2 r_{\rm e}}{G}. \tag{2}$$

Here $M_{\rm dyn}$ is defined as twice $M_{1/2}$, the mass enclosed in the isosurface where half the light is emitted. Therefore, the ratio $M_{\rm dyn}$ to $M_\star$ provides a rigorous comparison of dynamical and stellar masses *within the effective radius* (because $M_{\rm dyn}$ and $M_\star$ are, respectively, twice the dynamical and stellar masses within the isosurface where half the light is emitted).

Dynamical masses of high-redshift galaxies, using equation (2), have often led to the unphysical result $M_{\rm dyn} < M_\star$ (e.g. Stockton, Shih & Larson 2010; Martinez-Manso et al. 2011; Barro et al. 2014; Hsu, Stockton & Shih 2014; Stockton et al. 2014). Significantly, the mass discrepancy is also found in nearby massive *compact* ellipticals (Ferré-Mateu et al. 2012).

Addressing the mass discrepancy problem, Peralta de Arriba et al. (2014, hereinafter PdA14) demonstrated that mass discrepancy does not depend on redshift, and instead scales with galaxy compactness, defined as the $r_{\rm e}$ offset from the stellar mass–size distribution of ETGs in the nearby Universe. PdA14 derived an empirical scaling of $M_{\rm dyn}$ with $\sigma_{\rm e}$ and $r_{\rm e}$ such that

$$M_{\rm dyn} \propto \sigma_{\rm e}^{3.6} r_{\rm e}^{0.35}, \tag{3}$$

which implies a breakdown of homology.

The galaxies analysed by PdA14 cover a wide redshift range ($0 < z < 2.5$) and come from diverse, heterogeneous sources. In this work, we analyse the $M_{\rm dyn}$–$M_\star$ relationship over a narrow redshift range around $z \approx 1.0$. Hence, we exclude systematic effects on the data and evolutionary effects on the galaxy population, which could plausibly have affected previous work.

The core data set are 10 velocity dispersion measurements of 9 extremely compact massive ellipticals at $z \sim 1$, taken with the 10.4 m Gran Telescopio Canarias (GTC), 6 of which are new measurements that we describe in detail. We combine these data with velocity dispersions from the literature and draw a sample that covers stellar masses 10^{11} M$_\odot \lesssim M_\star < 10^{12}$ M$_\odot$ and effective radii ranging from 'normal' to the most compact massive galaxies. This sample is ideal to show whether, at a narrow, cosmologically distant epoch, the deviation between dynamical and stellar mass follows the scaling relationship proposed by PdA14. We use a large $z \sim 0$ sample of massive galaxies to further test the predictions by comparing two snapshots in cosmic time.

The paper is organized as follows. In Section 2, we describe the samples used in the paper: massive compact galaxies at $z \sim 1$ (Section 2.1), the additional data at $z \sim 1$ (Section 2.2) and the nearby reference at $z \sim 0$ (Section 2.3). In Section 2.1.1, we also report the recent $M_\star$ values for our new six massive compact galaxies, extracted from the Rainbow Cosmological Surveys data base (see Pérez-González et al. 2008; Barro et al. 2011a,b); while in Section 2.1.2 we describe the aperture correction for the velocity dispersions. In Section 3, we explain the spectroscopic observations (Section 3.1), data reduction (Section 3.2) and velocity dispersion measurements (Section 3.3). Accurate sky subtraction, done by implementing the method of Kelson (2003) within the REDUCEME package[1] (Cardiel 1999), is demonstrated in Appendix A, while the robustness of our velocity dispersion measurements is shown in Appendix B. In Appendix C, the reduced spectra and the fits are plotted. Appendix D gathers the structural parameters for the $z \sim 1$ sample. We compare dynamical and stellar masses in Section 4, confirming the dependence on compactness. In Section 5, we study the relationship between $M_\star$, $r_{\rm e}$ and $\sigma_{\rm e}$ (the stellar mass plane), and use this information to constrain a generic evolution mechanism in Section 5.1. In Section 5.2, we compare our results with numerical simulations of dry mergers. The discussion is presented in Section 6, while the conclusions are given in Section 7. We adopt the concordance Λ cold dark matter cosmology ($\Omega_{\rm m}$=0.3, Ω_Λ=0.7, $H_0 = 70$ km s^{-1} Mpc^{-1}); at $z = 1$, 1 arcsec corresponds to 8.01 kpc. The stellar masses assume a Salpeter initial mass function (IMF); where necessary, we have used the relationships in Longhetti & Saracco (2009) to convert stellar masses from the literature to this IMF.

2 SAMPLES

The core sample for this study is a set of nine massive compact galaxies at $z \sim 1$ for which our group obtained spectroscopy on two runs with the Optical System for Imaging and low-Intermediate-Resolution Integrated Spectroscopy[2] on the 10.4 m GTC. Data for four galaxies obtained in the first run are described in Martinez-Manso et al. (2011, hereinafter MM11). The present paper fully describes the data from the second run, including sample selection and characterization (Section 2.1), spectroscopy and velocity dispersion determination (Section 3).

We expand this massive compact galaxy sample with data from the literature to create a $z \sim 1$ sample with a broad coverage of the $M_\star$–$r_{\rm e}$ plane (Section 2.2).

We also devise a reference $z \sim 0$ sample (Section 2.3). Galaxies from both samples are similarly massive ($M_\star \gtrsim 10^{11}$ M$_\odot$) and have spheroid-like surface brightness profiles (Sérsic index $n > 2.5$).

2.1 Massive compact galaxies at $z \sim 1$

Target selection for both runs was similar. We selected pairs of galaxies from the catalogue of spheroid-like ($n > 2.5$), massive ($M_\star \gtrsim 10^{11}$ M$_\odot$) galaxies in the Extended Groth Strip (EGS; Davis et al. 2007), built by Trujillo et al. (2007, hereinafter T07). This catalogue covers a redshift range from 0.2 to 2.0 and is complete in stellar mass down to 10^{11} M$_\odot$ (the details of its stellar mass estimations are presented in Bundy et al. 2006 and Conselice et al. 2007). Galaxies were selected in pairs given that we would use the long-slit mode of OSIRIS, and would follow the strategy of placing two targets in each slit.

The selection criteria were:

(i) To have a Sérsic index $n > 4.0$.

(ii) To be closer than 4 arcmin on the sky, to allow simultaneous observation with the long slit of OSIRIS.

(iii) To have a spectroscopic redshift $z \approx 1.0$.

(iv) To be near the compact end of the size distribution at each stellar mass.

(v) To have apparent magnitude $I_{\rm AB} < 22.2$.

Out of the sample, four galaxies were observed in the first run and they are described in MM11. In the second run, we observed six galaxies. We chose to have one galaxy (ID 12024790) in common with the sample of MM11, to allow comparison of the velocity dispersions.

---

[1] http://guaix.fis.ucm.es/~ncl/reduceme

[2] http://www.gtc.iac.es/instruments/osiris

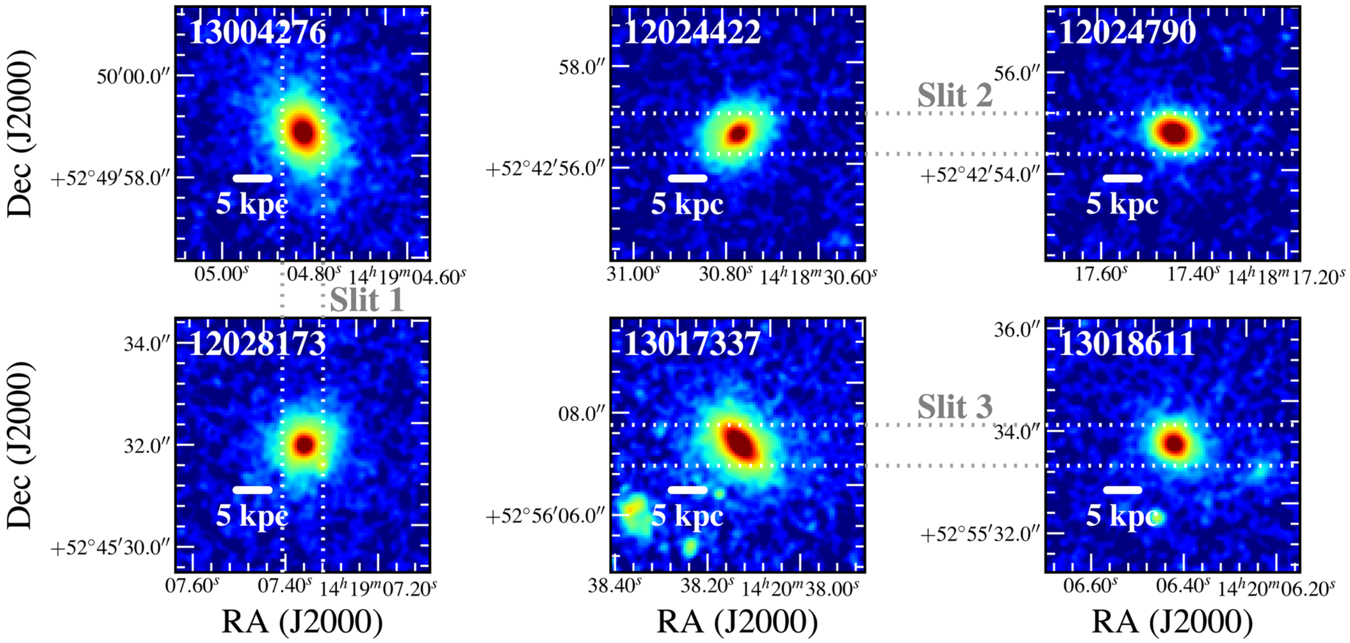

Figure 1. Images of the six massive compact galaxies at $z \sim 1$, from the Hubble Legacy Archive. These images were taken with ACS through the F814W filter (I band). They are combined images and were smoothed using a Gaussian filter with a standard deviation of 1 pixel. Each panel shows a galaxy at its centre and covers 5 arcsec on a side. Galaxy identifications are shown in the top left corner of each panel. A scale bar of 5 kpc is shown in each panel. Dotted lines represent the slits used in the spectroscopic observations.

Table 1. Observed properties of our sample of six massive compact galaxies at redshift ∼1. (1) Galaxy identifications from the DEEP-2 Galaxy Redshift Survey (Davis et al. 2003, 2007; Newman et al. 2013). (2) Right ascensions. (3) Declinations. (4) Apparent I-band magnitudes in the AB system from Trujillo et al. (2007, hereinafter T07). (5) Apparent K_s-band magnitudes in the AB system from T07. (6) Effective (half-light) radii along the semimajor axis from T07. (7) Ellipticities from T07. (8) Spectroscopic redshifts from the DEEP-2 Galaxy Redshift Survey (their absolute errors are $\lesssim 10^{-5}$). (9) Slit identifications of the spectroscopic observations. (10) Exposure times on target of the observations. (11) Rest-frame signal-to-noise ratios per angstrom in the spectra in the region of Ca II H and K (i.e. 3900–4000 Å).

ID (1)	RA (J2000) (2)	Dec. (J2000) (3)	I (AB mag) (4)	K_s (AB mag) (5)	a_e (arcsec) (6)	ϵ (7)	z (8)	Slit (9)	t_{exp} (h) (10)	$(S/N)_{\mathrm{rest}}$ (Å $^{-1}$) (11)
13004276	$14^{\mathrm{h}}19^{\mathrm{m}}04^{\mathrm{s}}.81$	$+52^\circ49'58''.64$	21.55	19.21	0.24	0.42	0.97533	1	6	14
12028173	$14^{\mathrm{h}}19^{\mathrm{m}}07^{\mathrm{s}}.34$	$+52^\circ45'31''.59$	22.06	19.59	0.20	0.20	0.95764	1	6	13
12024790	$14^{\mathrm{h}}18^{\mathrm{m}}17^{\mathrm{s}}.42$	$+52^\circ42'54''.89$	21.89	20.00	0.09	0.43	0.96572	2	4	19
12024422	$14^{\mathrm{h}}18^{\mathrm{m}}30^{\mathrm{s}}.79$	$+52^\circ42'56''.65$	22.19	19.82	0.26	0.44	1.02874	2	4	14
13017337	$14^{\mathrm{h}}20^{\mathrm{m}}38^{\mathrm{s}}.08$	$+52^\circ56'07''.27$	21.20	19.08	0.31	0.69	0.97242	3	3	15
13018611	$14^{\mathrm{h}}20^{\mathrm{m}}06^{\mathrm{s}}.37$	$+52^\circ55'33''.61$	22.15	19.99	0.17	0.26	1.07939	3	3	12

In Fig. 1, we show *Hubble Space Telescope*/Advanced Camera for Surveys (ACS) images of the six galaxies of the second run. Their observed properties, as well as parameters for their spectroscopic observations, are listed in Table 1. For the remaining of this paper, our sample will refer to the galaxies of the second run.

2.1.1 Stellar masses

For the galaxies of the second run, we upgraded the stellar masses from the T07 values to the data available in the Rainbow Cosmological Surveys data base (see Pérez-González et al. 2008; Barro et al. 2011a,b). We chose the masses from Rainbow Cosmological Surveys data base because they have been computed using photometry with a broader spectral range (UV–FIR), while T07 used only *BRIJK*. We used stellar masses computed with spectroscopic redshifts. These masses assume a Salpeter (1955) IMF, models from PÉGASE 2.0 (Fioc & Rocca-Volmerange 1997) and a Calzetti et al. (2000) extinction law. The upgraded values for these galaxies are on average 0.14 dex lower than the T07 values. This difference can be explained due to the usage of different models in their computation (see Muzzin et al. 2009). Differences are less than 1σ for each individual galaxy.

These upgraded values for the galaxies of the second run have been included in Table 2, which summarizes derived properties of our sample of six compact galaxies.

For the galaxies of the first run, MM11 report stellar masses assuming a Chabrier IMF; we have converted their values to a Salpeter IMF. After this conversion, the stellar mass determinations in MM11 and Rainbow Cosmological Surveys data base are nearly but not completely identical: MM11 assume a solar metallicity, while the metallicity is not constrained in the stellar masses from the Rainbow Cosmological Surveys data base. MM11 values are on

Table 2. Derived properties of our sample of six massive compact galaxies at redshift ∼1. (1) Galaxy identifications from the DEEP-2 Galaxy Redshift Survey. (2) Sérsic indices from T07. (3) Circular effective (half-light) radii computed using the apparent effective radii along the semimajor axis (from T07), the ellipticities (from T07) and the redshifts (from the DEEP-2 Galaxy Redshift Survey); their uncertainties are 10 per cent. (4) Stellar masses from T07; their uncertainties are ∼0.2 dex. (5) Stellar masses from Rainbow Cosmological Surveys data base (see Pérez-González et al. 2008; Barro et al. 2011a,b); in particular, the masses with the tag *ZSPEC* of this data base, which improve the fits using spectroscopic redshifts. (6) Statistical errors of the stellar masses from Rainbow Cosmological Surveys data base. (7) Mean velocity dispersions inside the slit aperture measured in 100 Monte Carlo realizations of each spectrum (errors are estimated with their standard deviations). (8) Aperture correction factor (computed following the prescriptions in the appendix B of van de Sande et al. 2013). (9) Velocity dispersions within the effective (half-light) radius.

ID (1)	n (2)	r_e (kpc) (3)	$M_\star^{\rm T07}$ (10^{11} M$_\odot$) (4)	$M_\star$ (10^{11} M$_\odot$) (5)	$\Delta M_\star$ (dex) (6)	σ (km s^{-1}) (7)	σ/σ_e (8)	σ_e (km s^{-1}) (9)
13004276	5.19	1.46	3.5	2.0	0.09	320 ± 15	0.94	340 ± 16
12028173	5.99	1.42	1.6	1.2	0.06	214 ± 16	0.94	228 ± 17
12024790	4.47	0.54	1.2	0.9	0.03	241 ± 14	0.92	261 ± 15
12024422	4.84	1.57	2.3	1.2	0.02	225 ± 17	0.94	239 ± 18
13017337	4.33	1.37	3.6	1.8	0.5	274 ± 23	0.94	291 ± 25
13018611	4.76	1.19	1.7	3.0	0.05	151 ± 15	0.94	161 ± 16

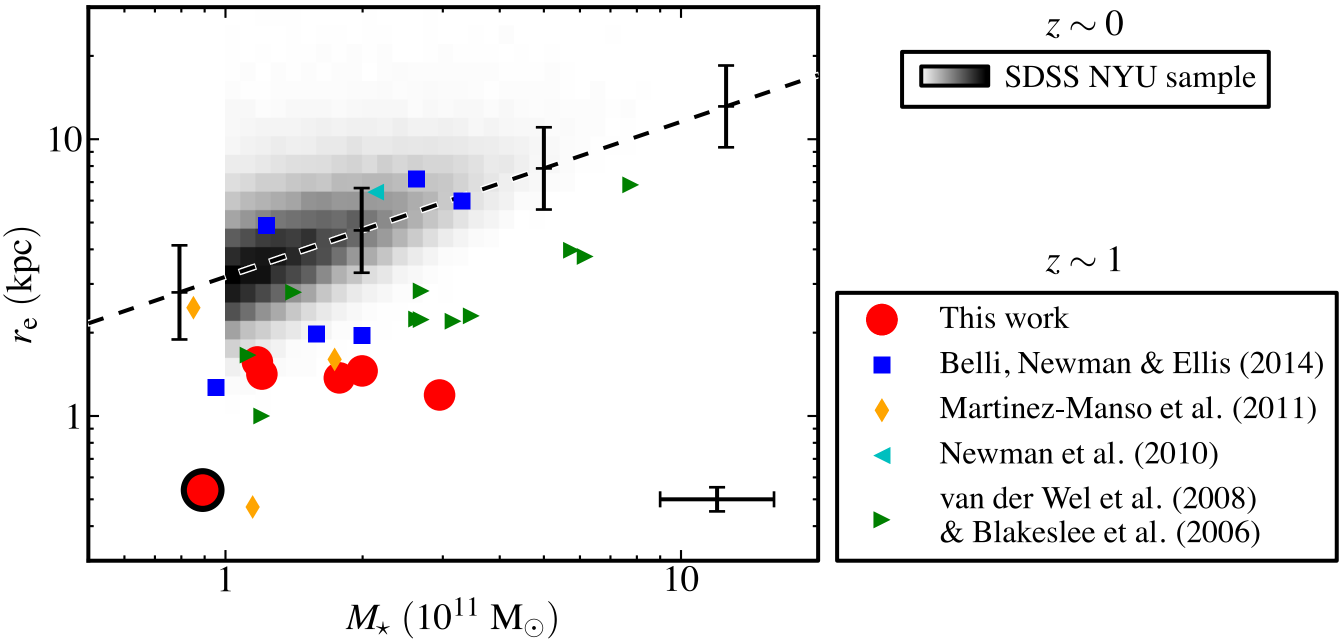

Figure 2. The stellar mass–size distribution of the spheroid-like galaxies used in this work. The sources of the $z \sim 1$ sample are given in the legend. The data point with a black edge represents the galaxy ID 12024790 also studied by Martinez-Manso et al. (2011, hereinafter MM11). The error bar cross on the bottom right corner represents the mean errors of our six compact galaxies at $z \sim 1$. The $z \sim 0$ sample is represented with a grey-scale giving the density of galaxies in the $M_\star$–r_e plane. The dashed line shows the relationship that spheroid-like galaxies follow in the nearby Universe (Shen et al. 2003), while its error bars show the dispersion of this relationship.

average 0.11 dex lower than the values from Rainbow Cosmological Surveys data base. Nevertheless, the differences fall well within the uncertainties of each determination. We will use the stellar mass values from MM11 for the galaxies of the first run in the remaining of the paper (except for the galaxy in common with the second run).

In Fig. 2, we show the stellar mass–size distribution for the nine compact galaxies, together with that from the additional data described in Sections 2.2 and 2.3. Appendix D gathers the structural parameters for the $z \sim 1$ sample, including the stellar masses from the two runs of the core sample.

2.1.2 Aperture correction of velocity dispersions

In this paper, we will work with velocity dispersions integrated over an aperture of one effective radius. For the galaxies of the first run, MM11 report velocity dispersions corrected to an aperture diameter of 1.19 kpc. We have taken their uncorrected values (around 6 per cent lower than the 1.19 kpc aperture-corrected values) and performed a correction to one effective radius following the prescriptions in the appendix B of van de Sande et al. (2013). These prescriptions take into account the effect of the point-spread function (PSF). To consider this fact is key due to the small apparent size of the galaxies at redshift 1. Also it is important to note that this correction can be used for apertures bigger than effective radius; while this does not occur for the aperture correction equations proposed by Jorgensen, Franx & Kjaergaard (1995) and Cappellari et al. (2006) (see appendix B of van de Sande et al. (2013) for a detailed explanation). This correction increases around 7 per cent their uncorrected values, i.e. the final values are similar to the 1.19 kpc aperture-corrected values. Appendix D gathers the structural parameters for the $z \sim 1$ sample, including the velocity dispersions from the first run of the core sample.

2.2 Additional galaxies at $z \sim 1$

We have obtained from the literature a sample of 18 massive ETGs at $z \sim 1$ ($M_\star \gtrsim 10^{11}$ M$_\odot$, $n > 2.5$ and $0.9 < z < 1.1$) with published effective radii, spectroscopic redshifts and velocity dispersions. The sources of these data are:

(i) Belli, Newman & Ellis (2014): six galaxies.

(ii) Newman et al. (2010): one galaxy (extracted from the compilation made by van de Sande et al. 2013).

(iii) van der Wel et al. (2008) and Blakeslee et al. (2006): 11 galaxies (also extracted from the compilation made by van de Sande et al. 2013).

These publications offer the velocity dispersion values corrected to an aperture of one effective radius. They also follow the prescriptions in the appendix B of van de Sande et al. (2013).

The stellar mass–size distribution of these $z \sim 1$ data is shown in Fig. 2. All authors use our cosmology so no further corrections were needed.

2.3 The nearby reference: massive galaxies from the SDSS NYU sample

We have selected a sample of 53 889 galaxies from the New York University Value-Added Galaxy Catalogue (Blanton et al. 2005), which is based in the Sloan Digital Sky Survey (hereinafter SDSS; York et al. 2000). In what follows, we will refer this data set as SDSS NYU sample. The criteria for the selection of these galaxies were: (i) they have to be massive (10^{11} M$_\odot$ $< M_\star <$ 10^{12} M$_\odot$), (ii) they are spheroid like ($n > 2.5$ in the r band), (iii) they have redshifts around the peak of the SDSS redshift distribution ($0.05 < z < 0.11$), (iv) they have reliable velocity dispersions ($70\,\mathrm{km\,s^{-1}} < \sigma < 420\,\mathrm{km\,s^{-1}}$) and (v) their physical sizes are reliable ($0.3\,\mathrm{kpc} < r_\mathrm{e} < 30\,\mathrm{kpc}$ in the r band).

Using equation 1 of Cappellari et al. (2006), we have corrected the velocity dispersions from the fixed aperture (3 arcsec) of the SDSS fibres to the expected within one effective radius.

The stellar mass–size distribution of these data is shown in Fig. 2.

3 DATA

In this section, we explain the spectroscopic observations, data reduction and velocity dispersion measurements for the second run of six massive compact galaxies described in Section 2.1.

3.1 Spectroscopic observations

Long-slit spectra for the six galaxies were obtained using the OSIRIS instrument at the 10.4 m GTC telescope. Observations were carried out in queue-scheduled service mode in 10 nights between 2012 April and August. We used the grating R2500I, which covers wavelengths from 7330 to 10 000 Å, corresponding rest-frame wavelengths at $z = 1.0$ are $3665\,\text{Å} < \lambda_\mathrm{rest} < 5000\,\text{Å}$. The slit width was 0.8 arcsec, which delivered a resolving power of $R = 2050$ at $\lambda = 8000\,\text{Å}$ as measured from the width of the arc lines, which translates into an instrumental resolution of $\sigma_\mathrm{inst} \sim 64\,\mathrm{km\,s^{-1}}$. We binned the CCD 2×2, yielding a sampling of 0.254 arcsec and 1.36 Å in the spatial and spectral directions, respectively. Hence, we sampled the spectral resolution element with 2.9 pixels. Observations were carried out in dark time with seeing $\lesssim$0.9 arcsec FWHM (full width at half-maximum).

Observations were broken in observing blocks of 1 h, each containing two 30 min exposures dithered by 7 arcsec along the slit. Total on-source integration for the three slits was 16.5 h, but 3.5 h yielded low counts, probably due to high clouds, and were unused. Exposure times on target for slits 1, 2 and 3 were 6, 4 and 3 h, respectively. Spectrophotometric standards from the Isaac Newton Group of Telescopes library[3] were observed each night.

3.2 Data reduction

We reduced our data following the standard steps (bias subtraction, flat-field correction, sky subtraction, cosmic ray removal, wavelength calibration, C-distortion correction, extinction correction, S-distortion correction, extraction and relative-flux calibration) using REDUCEME (Cardiel 1999), a reduction package for long-slit spectra. Sky subtraction in spectra redwards of 7000 Å is particularly difficult because the profiles of strong OH telluric lines, sampled by a few pixels only, get affected by spectral rectification yielding strong sky-subtraction residuals. We implemented in REDUCEME the algorithm proposed by Kelson (2003); taking advantage of the gradual shift of the wavelength solution along the slit, we build a grossly oversampled sky spectrum, which we then rebin using appropriate shifts for each CCD row. In Appendix A, we describe the software tools developed to use this method and show examples of its effectiveness. Source extraction was carried out via straight sum within an aperture of 9 pixels (2.286 arcsec). Signal-to-noise ratios measured in the 3900–4000 Å rest-frame wavelength range from 12 to 19 per angstrom; they are listed in column 11 of Table 1. Relative-flux calibration and correction for telluric absorption was carried out by using the spectrophotometric standard stars.

The reduced spectra of the six galaxies are plotted in Appendix C, together with the spectral fits described in Section 3.3. The spectra cover the rest-frame range 3800–4500 Å. Ca II H and K, the G band and several Balmer lines feature prominently, with varying relative intensities, indicating a mixture of old and intermediate-age stars. In addition, Mg I 3829, 3838 Å is visible in some of the spectra. The type of spectral features is similar to that found by MM11. Given the blue cut-off of our spectra, the presence of the forbidden emission line [O II] 3727 Å can only be checked on two of our galaxies; no firm evidence is found on any of the two galaxies (IDs 12024422 and 13018611).

3.3 Velocity dispersion measurements

We computed velocity dispersions using the penalized pixel fitting (pPXF) method of Cappellari & Emsellem (2004). This method characterizes the LOSVD by decomposing a spectrum as a linear

---

[3] http://catserver.ing.iac.es/landscape/tn065-100/workflux.php

superposition of templates which have been shifted considering the Doppler effect. We followed the steps described in Falcón-Barroso et al. (2011), fitting the LOSVD with the first two Gauss–Hermite moments and including the computation of uncertainties using Monte Carlo realizations.

Our spectral template library comprised simple stellar populations (SSPs) from the PÉGASE-HR library (Le Borgne et al. 2004). This library was selected because its high spectral resolution (0.55 Å FWHM) allows us to take advantage of the quality of our spectra (which have a resolution of ∼2 Å FWHM at rest frame). We restricted the choice of templates to SSP ages younger than age of the Universe at $z = 1$.

The use of SSPs was selected by the fact that SSPs have a more physically motivated combination of line strengths than combinations of stellar templates obtained by minimizing χ^2. This is important given that Ca II H and K can bias velocity dispersion determinations because their intrinsic width varies with stellar atmospheric temperature (Gebhardt et al. 2003). Because our spectra (Appendix C) show prominent Balmer lines in addition to Ca II H and K, the use of SSPs prevents the fitting programme against giving a solution that depends strongly on the relative weights of the stellar template mix. We show in Appendix B that the spectral fits are particularly sensitive to the choice of stellar templates.

The final fits are shown in Appendix C. Although the faintest targets have higher relative sky-subtraction residuals, the main spectral features can be detected by visual inspection, and properly identified by the fitting programme.

The velocity dispersions are listed in Table 2, together with derived properties of our sample of six massive compact galaxies. The robustness of these results is explained in Appendix B. Table 2 also provides the velocity dispersions corrected to one r_e apertures. This correction follows the prescriptions in appendix B of van de Sande et al. (2013), which adapts the corrections proposed by Jorgensen et al. (1995) and Cappellari et al. (2006) to higher apertures and takes into account the PSF effects.

4 DYNAMICAL VERSUS STELLAR MASS: DISCREPANCY GROWS WITH COMPACTNESS

In this section, we compare the dynamical mass computed as $M_{\rm dyn} = K\sigma_e^2 r_e/G$ with $K = 5.0$ (Cappellari et al. 2006) with the stellar masses derived using stellar population techniques.

In Fig. 3, we plot dynamical mass versus the stellar mass for our two redshift samples. We extract two results from this figure. First, in both panels we find galaxies below the dashed line. This indicates that the unphysical result $M_\star > M_{\rm dyn}$ occurs not only at $z \sim 1$ but also at $z \sim 0$.

Our second result relates to the dependence on galaxy compactness. The colour of each symbol in Fig. 3 has been used to indicate the compactness indicator defined as $r_e/r_{\rm Shen}(M_\star)$, where $r_{\rm Shen}(M_\star)$ is the mass–size relationship for galaxies in the nearby Universe from Shen et al. (2003), written as

$$r_{\rm Shen}(M_\star) = r^0_{\rm Shen}\left(\frac{M_\star}{10^{11}\ {\rm M}_\odot}\right)^{\eta}, \quad (4)$$

where $r^0_{\rm Shen} = 3.185$ kpc and $\eta = 0.56$. These values come from adapting the relationship in Shen et al. (2003) to a Salpeter IMF following the equations from Longhetti & Saracco (2009). The compactness indicator measures the r_e offset from the stellar mass–size distribution of ETGs in the nearby Universe.

In the left-hand panel of Fig. 3, which shows the $z \sim 0$ galaxies from the SDSS NYU sample, we can see that red colours (low $r_e/r_{\rm Shen}(M_\star)$) populate the area below the dashed line. This indicates that mass discrepancy in the nearby Universe grows with compactness. Observational errors in r_e (15 per cent; Cebrián & Trujillo 2014) translate into a 15 per cent scatter in $M_{\rm dyn}$ at a constant $M_\star$, which is only one third of the observed scatter of $M_{\rm dyn}$ at a constant

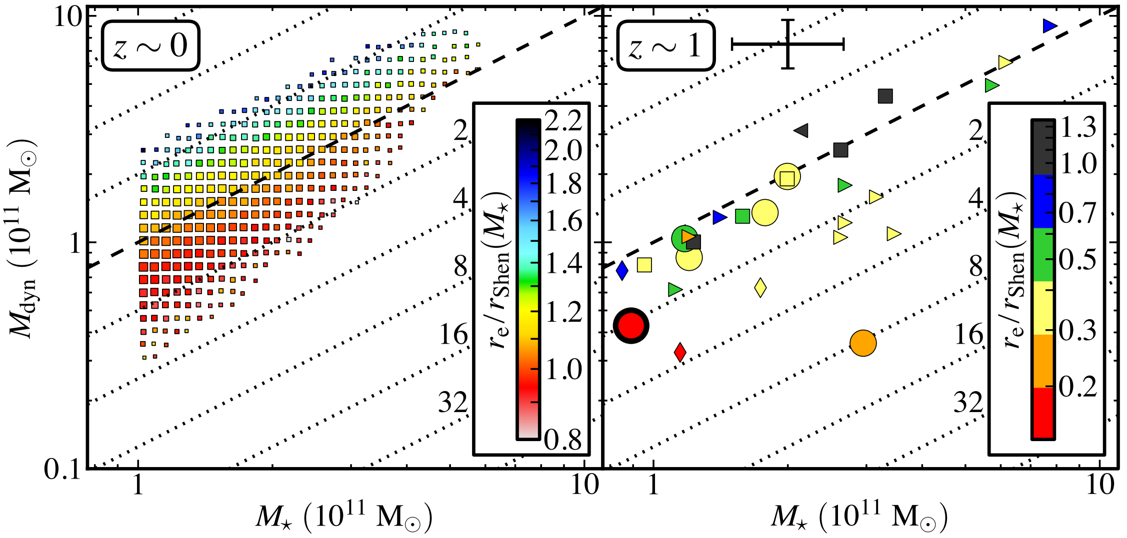

Figure 3. Stellar versus dynamical masses for the two redshift samples. Dashed line shows the identity relationship ($M_\star = M_{\rm dyn}$). Dotted lines below/above the dashed line indicate how many times (in powers of 2) the stellar mass is greater/smaller than dynamical mass (i.e. $M_\star = 2^i M_{\rm dyn}$ where i is an integer). Left-hand panel shows the $z \sim 0$ sample. For this sample, the data have been binned depending on their dynamical and stellar masses. The size of each symbol in the left-hand panel scales with the number of galaxies in each bin. For clarity, bins with fewer than 10 galaxies have been omitted. In the right-hand panel, which contains galaxies with $z \sim 1$, symbol shapes as in Fig. 2. In both panels, the colour of each symbol represents the compactness indicator $r_e/r_{\rm Shen}(M_\star)$, defined as the r_e offset from the stellar mass–size distribution of ETGs in the nearby Universe. The error bar cross on the top of the right-hand panel represents the mean errors of our six compact galaxies at $z \sim 1$.

$M_\star$. This corroborates that the trend of low $M_{\rm dyn}$ with compactness in Fig. 3 is real and not a result of error propagation.

At $z \sim 1$ (right-hand panel of Fig. 3), again, the distribution of the symbol colours follows a pattern such that more compact galaxies show stronger mass discrepancies. It is worth noting that in this redshift we find higher discrepant values due to the strong size evolution of this type of galaxies (e.g. Daddi et al. 2005; Trujillo et al. 2006; Longhetti et al. 2007; Toft et al. 2007, T07; Zirm et al. 2007; Cimatti et al. 2008; Buitrago et al. 2008).

Hence, our two samples covering narrow redshift ranges, and, therefore, largely free from redshift-dependent systematics in the mass determinations, confirm the result from PdA14, namely, that mass discrepancy grows with galaxy compactness.

We emphasize that, had we chosen a different IMF such as Chabrier, we would have alleviated the problem of galaxies showing $M_{\rm dyn} < M_\star$, but would not have solved it. The range of IMF variations proposed by authors such as Treu et al. (2010), Cappellari et al. (2012) or Ferreras et al. (2013) would reduce our stellar masses by at most a factor of 2. We would still have several galaxies at the low-redshift panel showing the mass anomaly. However, at high redshift, selecting other IMF will be insufficient to solve the problem. Furthermore, the authors mentioned above associate bottom-heavy IMFs with massive (high-velocity-dispersion) galaxies, which supports the choice of a Salpeter IMF made in this paper. This expectation agrees with the results from Martín-Navarro et al. (2015), which found a bottom-heavy IMF for massive ETGs at $z \sim 1$.

4.1 Weak homology: non-homology from differences in light profiles

Several authors have proposed that a deviation from a constant value for K could be originated by the different light profiles that galaxies show. Using one-component, spherical, non-rotating and isotropic models, Bertin, Ciotti & Del Principe (2002) derived an equation where K depends on Sérsic index n (from 6.6 to 2.2 in the interval $n \epsilon$ (2.5, 8)). Cappellari et al. (2006) found also a similar expression assuming spherical isotropic models with Sérsic profile (from 6.9 to 3.8 when n varies from 2.5 to 8). Nevertheless, these authors found a quite constant value for their observed galaxies (5.0 ± 0.1). Taylor et al. (2010), comparing also stellar masses from stellar population techniques with virial mass estimators, reported that following the prescriptions of Bertin et al. (2002) improved the correspondence between stellar and dynamical masses.

Could this effect remove the trend between $M_\star/M_{\rm dyn}$ and $r_{\rm e}/r_{\rm Shen}(M_\star)$ reported in Section 4? Fig. 4 addresses this question showing the relation between $M_\star/M_{\rm dyn}^{\rm weak}$ and $r_{\rm e}/r_{\rm Shen}(M_\star)$, being $M_{\rm dyn}^{\rm weak}$ the dynamical mass computed with a K which follows the dependence on n modelled by Cappellari et al. (2006), i.e.

$$K(n) = 8.87 - 0.831n + 0.0241n^2. \tag{5}$$

Thanks to this figure, we can check that the trend between $M_\star/M_{\rm dyn}^{\rm weak}$ and $r_{\rm e}/r_{\rm Shen}(M_\star)$ remains. The trend also remains if we use the expression proposed by Bertin et al. (2002).

5 STELLAR MASS PLANE

In this section, we study the relationship between $M_\star$, $r_{\rm e}$ and $\sigma_{\rm e}$. We fit a plane of the form $M_\star \propto \sigma_{\rm e}^a r_{\rm e}^b$, with a and b real numbers, to the $z \sim 1$ sample. The hypotheses of virial equilibrium and homology imply a plane of the form

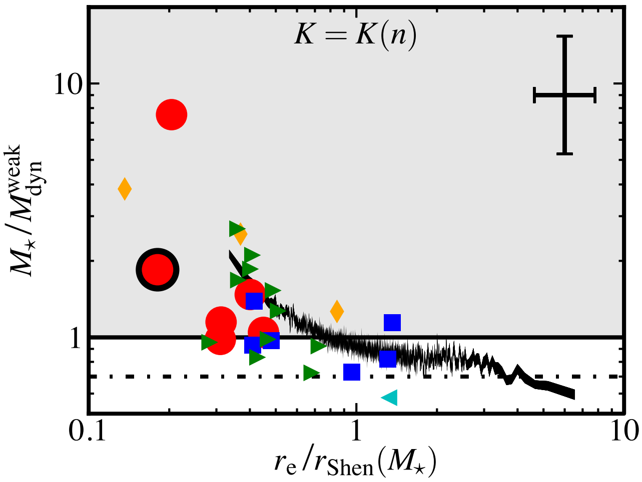

Figure 4. Correlation between $M_\star/M_{\rm dyn}^{\rm weak}$ and the compactness indicator $r_{\rm e}/r_{\rm Shen}(M_\star)$, being $M_{\rm dyn}^{\rm weak}$ the dynamical mass computed with the dependence of K on Sérsic index n given by equation (5). Symbols for the $z \sim 1$ sample as in Fig. 2. The solid black line shows the data from the $z \sim 0$ sample after grouping them in their 1000-quantiles of their $r_{\rm e}/r_{\rm Shen}(M_\star)$ distribution; the width of this line shows the error of the mean in each 1000-quantile. The grey area shows the unphysical region where $M_\star > M_{\rm dyn}$. The dash–dotted line corresponds to a stellar-to-dynamical mass ratio of 0.7, derived from lensing of nearby massive ellipticals by Gavazzi et al. (2007).

$$M_\star = f_{\rm dyn}^\star \; K \; \frac{\sigma_{\rm e}^2 r_{\rm e}}{G}, \tag{6}$$

where

$$K \text{ is a constant} \tag{7}$$

and $f_{\rm dyn}^\star \equiv M_\star/M_{\rm dyn}$ may also be considered as constant, due to a random or weak dependence on $M_\star$, $r_{\rm e}$ or $\sigma_{\rm e}$. In the following, we assume $f_{\rm dyn}^\star = 0.7$ (Gavazzi et al. 2007). This assumption agrees with the results reported by Taylor et al. (2010), which found that $f_{\rm dyn}^\star$ depends very weakly on stellar mass at fixed Sérsic index n and varies little for the range of n of our sample (~0.1 dex). As noted in Section 1, several works have found that equation (6) applies to nearby, massive ellipticals and lenticulars (e.g. Cappellari et al. 2006). Because equation (6) leads to unphysical dynamical masses, PdA14 proposed a modification of equation (6), where K is allowed to vary with the compactness indicator $r_{\rm e}/r_{\rm Shen}(M_\star)$, such that

$$K = \left(\frac{r_{\rm e}}{r_{\rm Shen}(M_\star)}\right)^\alpha \kappa, \tag{8}$$

where κ is a constant. It is worth noting that this parametrization allows also the variation of $f_{\rm dyn}^\star$with the compactness indicator $r_{\rm e}/r_{\rm Shen}(M_\star)$, but including it as part of the K variation. These authors choose this option because they argued that the deviation from homology cannot be produced mainly by the variation of $f_{\rm dyn}^\star$(cf. fig. 9 of PdA14).

Our six compact galaxies add essential data to test for variations of K with compactness. In Fig. 5, we show the K value versus the compactness indicator $r_{\rm e}/r_{\rm Shen}(M_\star)$. The red solid line represents the predictions of virial theorem with homology (equation 7) using the value $K = 5.0$ found by Cappellari et al. (2006), while we used the green dotted line to plot the predictions of PdA14 (equation 8), which proposed $\alpha = -0.81 \pm 0.05$ and $\kappa = 6.0 \pm 0.2$.

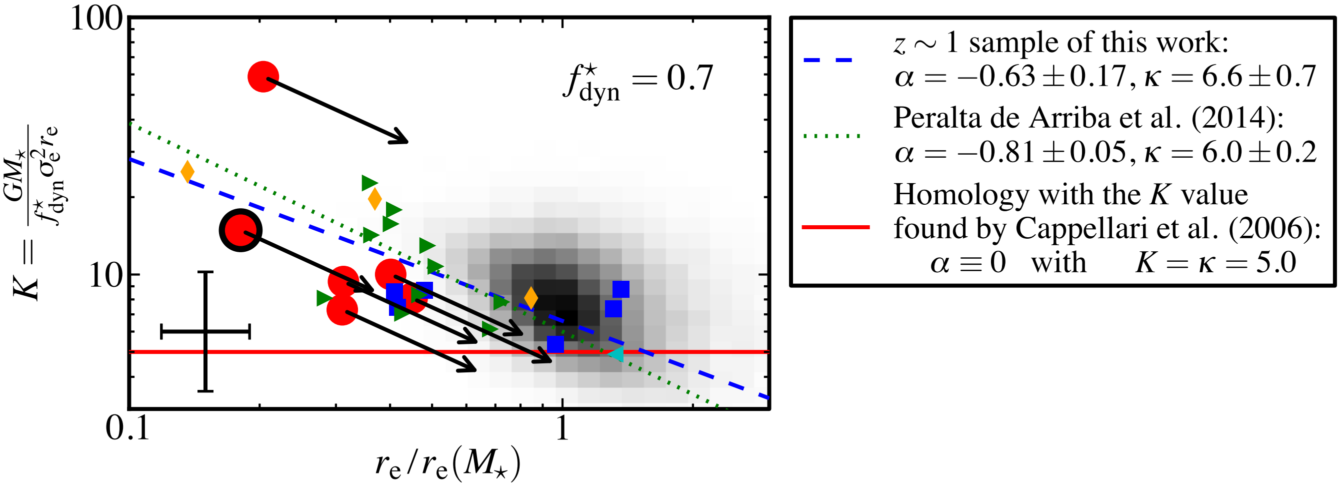

Figure 5. K value versus the compactness indicator $r_{\rm e}/r_{\rm Shen}(M_\star)$ (i.e. the distance to nearby stellar mass–size scaling relationship). Symbols as in Fig. 2. Red solid and green dotted lines show the prediction of virial theorem with homology (considering the value $K = 5.0$ found by Cappellari et al. 2006), and the prediction of PdA14. The blue dashed line shows the fit of the $z \sim 1$ sample. Black arrows show expected evolution up to $z = 0$ of the six massive compact galaxies if they would follow the equations proposed by Tapia et al. (2015, see Section 5.2). The error bar cross on the bottom left corner represents the mean errors of our six compact galaxies at $z \sim 1$.

All of our massive compact galaxies except one follow the predictions of PdA14, while one of them shows a higher value of K than both predictions. Its extreme K value is caused by a low $\sigma_{\rm e}$ ($161 \pm 16\,{\rm km\,s^{-1}}$); K drops slightly ($K = 40.3$) but remains well above the PdA14 relation, if we use the velocity dispersion from Fernández Lorenzo et al. (2011, $\sigma_{\rm e} = 196 \pm 6\,{\rm km\,s^{-1}}$).

Fitting equation (8) to all of our objects at $z \sim 1$, we obtain

$$\alpha = -0.63 \pm 0.17 \tag{9}$$

and

$$\kappa = 6.6 \pm 0.7, \tag{10}$$

where the errors have been computed using the bootstrap resampling technique. This is 1σ compatible with the results from PdA14, but it is inconsistent with the prediction of equation (7) (α is 4σ from 0). This fit has been represented in Fig. 5 with a blue dashed line. Note that in Fig. 5 the regression to $z \sim 1$ (equations 9 and 10) matches the $z \sim 0$ sample despite the latter being excluded from the fit.

5.1 Evolutionary constraints of stellar mass plane

In this section, we study the constraints that the stellar mass plane implies for the mechanisms which drive size evolution in this type of galaxies.

We focus on a generic mechanism in which the changes of $r_{\rm e}$ and $\sigma_{\rm e}$ scale as power laws of the mass growth:

$$\frac{r_{\rm e}^{\rm f}}{r_{\rm e}^{\rm i}} = \left(\frac{M_\star^{\rm f}}{M_\star^{\rm i}}\right)^{\rho} \tag{11}$$

and

$$\frac{\sigma_{\rm e}^{\rm f}}{\sigma_{\rm e}^{\rm i}} = \left(\frac{M_\star^{\rm f}}{M_\star^{\rm i}}\right)^{\Sigma}, \tag{12}$$

where $M_\star^{\rm i}$, $r_{\rm e}^{\rm i}$ and $\sigma_{\rm e}^{\rm i}$ denote the initial stage of an individual galaxy before the interaction of the mechanism, and the superindex 'f' is analogously used to indicate the final stage. We choose such scaling relations because of their simplicity and because we expect the changes of $r_{\rm e}$ and $\sigma_{\rm e}$ to be strongly affected by the changes in mass.

The geometric interpretation of the above equations is that the mechanism driving size evolution moves galaxies in a well-defined direction in the three-dimensional space ($\log M_\star$, $\log \sigma_{\rm e}$, $\log r_{\rm e}$).

If we consider that this movement has to happen inside a plane of the type defined by equations (6) and (8), we obtain a relationship between the exponents:

$$\alpha = \frac{\rho + 2\Sigma - 1}{\eta - \rho}, \tag{13}$$

where η is the slope of the mass–size relation for early types in the nearby Universe (equation 4). Under the virial theorem and homology (i.e. $\alpha \equiv 0$) a simpler relationship holds:

$$\Sigma = \frac{1 - \rho}{2}. \tag{14}$$

Additionally, relaxing the hypothesis of homology to allow a dependence of $f^\star_{\rm dyn}$ on $M_\star$ (i.e. $f^\star_{\rm dyn} \propto M_\star^{\delta}$), it leads to a shifted analogous relationship:

$$\Sigma = \frac{1 - \rho - \delta}{2}. \tag{15}$$

In the following, when we consider this last case, we will assume the value $\delta \sim -0.2$ (which comes from parametrizing the variation of $f^\star_{\rm dyn}$ reported by Taylor et al. (2010) with $M_\star$).

In Fig. 6, we show the restrictions on the ρ–Σ space that several stellar mass planes imply: (i) the plane predicted by virial theorem and homology (red solid line), (ii) the plane predicted by virial theorem and a *relaxed* homology where $f^\star_{\rm dyn} \propto M_\star^{-0.2}$ (red dash–dotted line), (iii) the plane proposed by PdA14 (green dotted line) and (iv) the plane obtained fitting the $z \sim 1$ sample of this work.

5.2 Numerical simulations of dry mergers

For massive compact galaxies, the cosmological evolution on the ($M_\star$, $\sigma_{\rm e}$, $r_{\rm e}$) space due to their merger history can be extracted from numerical merger simulations. Tapia et al. (2015) extracted merger histories from cosmological hydrodynamical simulations and reproduced them from $z = 2.5$ to $z = 0$ at high resolution, using N-body techniques. Initial primary galaxies had $M_\star \sim 10^{11}\,{\rm M_\odot}$ and

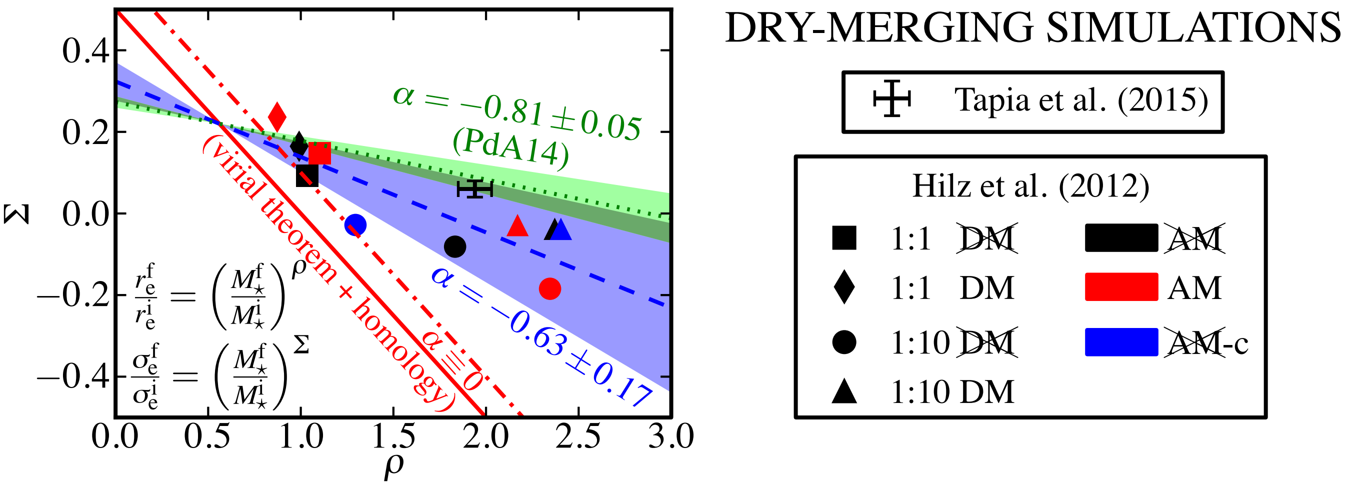

Figure 6. Stellar mass plane constraints on exponents ρ and Σ for a generic mechanism of evolution of the type $r_e^f/r_e^i = \left(M_\star^f/M_\star^i\right)^\rho$, $\sigma_e^f/\sigma_e^i = \left(M_\star^f/M_\star^i\right)^\Sigma$. Blue dashed and green dotted lines show the constraints from α exponents obtained from the stellar mass plane proposed in Section 5 of this work and in PdA14. The shadow regions around these lines cover the 1σ errors of these exponents. The red solid line shows the constraints from virial theorem and homology prediction. The red dash–dotted line shows the constraints from virial theorem and a *relaxed* homology where stellar-to-dynamical mass ratio depends on stellar mass ($f_{\rm dyn}^\star \propto M_\star^{-0.2}$). Black data cross is the result found in the simulations of Tapia et al. (2015). The results from the simulations of Hilz et al. (2012) are represented as indicated in the legend: 1:1/1:10 label corresponds to simulations of major/minor mergers, the label 'DM' indicates the galaxies are embedded in matter haloes (or not if it is crossed out), the label 'AM' refers to an orbit with angular momentum (or without angular momentum if it is crossed out), and the presence of the suffix '-c' means that the merging satellites were compact (i.e. satellites sizes were 50 per cent of the sizes assumed in the other simulations).

$r_e = 1$ kpc, while the merging secondaries had radii following the observational mass–size relationship at the epoch of the merger. Their simulations show that typically, a massive compact galaxy grows by a factor ∼2 in mass and a factor ∼4 in r_e from $z = 2.5$ to $z = 0$.

The changes of r_e and σ_e with mass growth measured in the simulations, fitted with equations (11) and (12), yield $\rho = 1.94 \pm 0.09$ and $\Sigma = 0.06 \pm 0.02$. These values are plotted in Fig. 6. There is a close agreement of the results of merger simulations with the stellar mass planes of PdA14 and that found in this work (equations 9 and 10). In contrast, the results of the merger simulations fall far from the prediction of the virial theorem and homology (even when this last assumption is relaxed to allow variations of $f_{\rm dyn}^\star$ as function of $M_\star$).

Hilz et al. (2012) simulated 10 series of mergers with mass ratios of 1:1 and 1:10, for a range of galaxy models (with or without dark matter haloes; varying the internal densities of the secondaries) and galaxy orbits (with or without orbital angular momentum). We have modelled the effects of these simulations with equations (11) and (12). This allows to include the results of 10 simulations from Hilz et al. (2012) in Fig. 6. This figure shows that the action of major or minor mergers gives movements in the space ($M_\star$, σ_e, r_e) which disagree with the homologous virial predictions, although major mergers and one of the minor-merger cases (mass ratio 1:10 without dark matter and with compact satellites which orbits do not have angular momentum) could be fitted with a deviation from homology where $f_{\rm dyn}^\star \propto M_\star^\delta$. We can check also that most of the simulations (8 out of 10) fall within the 1σ error of the stellar mass plane proposed in this work.

The comparisons with N-body mergers described here show that the evolution of r_e and σ_e as $M_\star$ grows due to mergers moves massive galaxies out of the homology plane, along the mass plane proposed here. Nevertheless, a deviation from homology varying stellar-to-dynamical mass ratio with stellar mass can match the major-merger simulations and a particular case of minor mergers.

6 DISCUSSION

It has been amply recognized that velocity dispersions contain key information to constrain the evolutionary processes linking massive compact galaxies at high redshift with nearby massive ellipticals: a simple transformation between equilibrium states by injection of dynamical energy predicts velocity dispersions around 500 km s^{-1} for galaxy masses ∼10^{11} M$_\odot$, while galaxy growth via mergers predicts velocity dispersions to hardly evolve (Hopkins et al. 2010). Our measurements add to the growing body of data that shows velocity dispersions (σ_e in the range 200–350 km s^{-1}) for massive compact ellipticals. To our knowledge, there remains one single case of a massive passive galaxy with reported velocity dispersion above 500 km s^{-1}, namely, a $z = 2.186$ galaxy with $M_\star = 3.2 \times 10^{11}$ M$_\odot$ and $r_e = 0.78$ kpc, for which van Dokkum, Kriek & Franx (2009) reported a value of 510^{+165}_{-95} km s^{-1}.

The comparison of our velocity dispersion measurements with those from other authors (see Appendix B) indicates that uncertainties in velocity dispersions could be underestimated. de Bruyne et al. (2003) advised that the usage of Monte Carlo simulations with white noise for estimating the errors can lead to values which are almost a factor of 2 lower than realistic errors. Although we have tried to improve our errors rejecting the strong sky residuals in the fits and in the amplitude of the white noise for Monte Carlo simulations, the dependence between pixels introduced in the reduction steps should be the dominant factor for the underestimation of the errors.

The explanation of the tilt of Fundamental Plane is a classic debate of extragalactic astronomy (e.g. Trujillo, Burkert & Bell 2004; Renzini 2006). Two options (or a combination of both) are possible: stellar population effects, or deviation from homology (where we include also variations of dark matter fractions). The stellar mass plane used in this work has the advantage of replacing the luminosity by the stellar mass (from stellar population techniques). This allows to address the problem in a space where the three variables are dynamically connected. Therefore, the existence of a tilt in this space implies the violation of homology.

The comparison with numerical simulations of dry mergers has worried us about some interpretation issues. For example, in the simulations from Hilz et al. (2012), although the break of homology happens in our observables ($M_\star$, σ_e, r_e), it does not occur in a 'theoretical' space where the variables are total bound mass, mean square speed and gravitational radius. This can be seen as an obviousness, because it only means that the equilibrium of energies predicted by virial theorem is satisfied. However, this advises that the assumption of homology is not possible for translating dry-merger simulation results from theoretical variables to observables (or even between different observables).

We have also compared our results with numerical simulations of puffing-up model. The simulations of Ragone-Figueroa & Granato (2011) predict that the three-dimensional stellar velocity dispersion and the half-mass radius are related by $\sigma_\mathrm{3D} \propto r_{1/2}^{\beta}$, with β varying from -0.49 to -0.83 depending on the mass loss from gas ejection and the ejection time chosen in the simulation. As β is not always $-1/2$, this indicates that homology can also be violated in puffing-up simulations. Our stellar mass plane predicts a law $\sigma_\mathrm{e} \propto r_\mathrm{e}^{-0.19\pm0.09}$ at fixed stellar mass, while the plane from PdA14 gives $\sigma_\mathrm{e} \propto r_\mathrm{e}^{-0.10\pm0.03}$. Assuming an 'ad hoc homology', i.e. $r_\mathrm{e} \propto r_{1/2}$ and $\sigma_\mathrm{e} \propto \sigma_\mathrm{3D}$, we could conclude that our stellar mass plane rejects a big contribution of puffing-up to the size evolution of ETGs. Nevertheless, when the break of homology is detected, this type of assumptions can lead to wrong results. Therefore, a puffing-up simulation which results where given in terms of observables would be useful to reject definitely the puffing-up mechanism.

Fig. 6 shows the importance of constraining observationally the stellar mass plane. The predictions from minor-merger evolution (Hilz et al. 2012) fall well within the stellar mass plane presented in this paper, while they deviate from the mass plane derived in PdA14. While the set of merger models with which we compare are quite restricted, Fig. 6 shows that this type of analysis has the potential of allowing to distinguish between major and minor mergers as the dominant channel for the mass and size growth histories of today's giant galaxies. While minor mergers have often been claimed for the growth of massive compact galaxies (Hopkins et al. 2009; Hilz et al. 2012; Tapia et al. 2015), a growth based on 1:1 to 1:5 mergers is in fact suggested by observations of the satellite distribution around massive galaxies at different redshifts (e.g. Ferreras et al. 2014; Ruiz, Trujillo & Mármol-Queraltó 2014).

7 CONCLUSIONS

The main conclusions of this paper are:

(i) Our measurements of velocity dispersions for six massive compact galaxies do not reveal the high values expected from a law $M_\star \propto \sigma_\mathrm{e}^2 r_\mathrm{e}$.

(ii) The discrepancy between stellar and dynamical masses computed as $M_\mathrm{dyn} = K\sigma_\mathrm{e}^2 r_\mathrm{e}/G$ with $K = 5.0$ follows the predictions of PdA14, i.e. it scales with galaxy compactness. This implies a breakdown of homology.

(iii) For our sample of massive galaxies at $z \sim 1$ which includes our six compact galaxies, we find a relationship between $M_\star$, σ_e and r_e compatible with the alternative scaling law proposed by PdA14. This result is compatible with a snapshot at $z \sim 0$ with galaxies from SDSS.

(iv) The relationship between $M_\star$, σ_e and r_e is compatible with numerical studies of the growth of massive ellipticals due to a mixture of minor and major mergers that have a cosmological framework like the one realized by Tapia et al. (2015). The numerical simulations of dry mergers from Hilz et al. (2012) also predict a break of homology in the same direction that our stellar mass plane constrains.

ACKNOWLEDGEMENTS

The authors are grateful to the referee for his/her insightful and constructive review. The authors also thank J. Martínez-Manso, G. Barro, A. J. Cenarro, L. Domínguez-Palmero, M. Fernández-Lorenzo, C. López-Sanjuan, M. Prieto, M. Cappellari, A. Cimatti, L. Ciotti, C. J. Conselice and the *Traces of galaxy formation* group (http://www.iac.es/project/traces) for their collaboration during the development of this paper. LPdA was partially supported by the FPI Program by Spanish Ministry of Science and Innovation. JF-B acknowledges the support from the FP7 Marie Curie Actions of the European Commission, via the Initial Training Network DAGAL under REA grant agreement number 289313. This work has been supported by the Programa Nacional de Astronomía y Astrofísica of the Spanish Ministry of Science and Innovation under the grants AYA2009-11137, AYA2012-30717, AYA2012-31277 and AYA2013-48226-C3-1-P. Based on observations made with the Gran Telescopio Canarias (GTC), installed at the Spanish Observatorio del Roque de los Muchachos of the Instituto de Astrofísica de Canarias (IAC), in the island of La Palma. This work has made use of the Rainbow Cosmological Surveys data base, which is operated by the Universidad Complutense de Madrid (UCM), partnered with the University of California Observatories at Santa Cruz (UCO/Lick, UCSC). Based on observations made with the NASA/ESA Hubble Space Telescope, and obtained from the Hubble Legacy Archive, which is a collaboration between the Space Telescope Science Institute (STScI/NASA), the Space Telescope European Coordinating Facility (ST-ECF/ESA) and the Canadian Astronomy Data Centre (CADC/NRC/CSA). This research made use of ASTROPY, a community-developed core PYTHON package for Astronomy (Astropy Collaboration 2013). This research made use of APLPY, an open-source plotting package for PYTHON hosted at http://aplpy.github.com.

REFERENCES

Astropy Collaboration, 2013, A&A, 558, A33
Barro G. et al., 2011a, ApJS, 193, 13
Barro G. et al., 2011b, ApJS, 193, 30
Barro G. et al., 2014, ApJ, 795, 145
Belli S., Newman A. B., Ellis R. S., 2014, ApJ, 783, 117
Bertin G., Ciotti L., Del Principe M., 2002, A&A, 386, 149
Blakeslee J. P. et al., 2006, ApJ, 644, 30
Blanton M. R. et al., 2005, AJ, 129, 2562
Buitrago F., Trujillo I., Conselice C. J., Bouwens R. J., Dickinson M., Yan H., 2008, ApJ, 687, L61
Bundy K. et al., 2006, ApJ, 651, 120
Calzetti D., Armus L., Bohlin R. C., Kinney A. L., Koornneef J., Storchi-Bergmann T., 2000, ApJ, 533, 682
Cappellari M., Emsellem E., 2004, PASP, 116, 138
Cappellari M. et al., 2006, MNRAS, 366, 1126
Cappellari M. et al., 2012, Nature, 484, 485
Cappellari M. et al., 2013, MNRAS, 432, 1709
Cardiel N., 1999, PhD thesis, Univ. Complutense de Madrid, Spain
Cebrián M., Trujillo I., 2014, MNRAS, 444, 682
Cimatti A. et al., 2008, A&A, 482, 21

Conselice C. J. et al., 2007, MNRAS, 381, 962
Daddi E. et al., 2005, ApJ, 626, 680
Davis M. et al., 2003, Proc. SPIE, 4834, 161
Davis M. et al., 2007, ApJ, 660, L1
de Bruyne V., Vauterin P., de Rijcke S., Dejonghe H., 2003, MNRAS, 339, 215
Falcón-Barroso J. et al., 2011, MNRAS, 417, 1787
Fernández Lorenzo M., Cepa J., Bongiovanni A., Pérez García A. M., Ederoclite A., Lara-López M. A., Pović M., Sánchez-Portal M., 2011, A&A, 526, AA72
Ferré-Mateu A., Vazdekis A., Trujillo I., Sánchez-Blázquez P., Ricciardelli E., de la Rosa I. G., 2012, MNRAS, 423, 632
Ferreras I., La Barbera F., de la Rosa I. G., Vazdekis A., de Carvalho R. R., Falcón-Barroso J., Ricciardelli E., 2013, MNRAS, 429, L15
Ferreras I. et al., 2014, MNRAS, 444, 906
Fioc M., Rocca-Volmerange B., 1997, A&A, 326, 950
Gavazzi R., Treu T., Rhodes J. D., Koopmans L. V. E., Bolton A. S., Burles S., Massey R. J., Moustakas L. A., 2007, ApJ, 667, 176
Gebhardt K. et al., 2003, ApJ, 597, 239
Hilz M., Naab T., Ostriker J. P., Thomas J., Burkert A., Jesseit R., 2012, MNRAS, 425, 3119
Hopkins P. F., Bundy K., Murray N., Quataert E., Lauer T. R., Ma C.-P., 2009, MNRAS, 398, 898
Hopkins P. F., Bundy K., Hernquist L., Wuyts S., Cox T. J., 2010, MNRAS, 401, 1099
Hsu L.-Y., Stockton A., Shih H.-Y., 2014, ApJ, 796, 92
Jorgensen I., Franx M., Kjaergaard P., 1995, MNRAS, 276, 1341
Kelson D. D., 2003, PASP, 115, 688
Le Borgne D., Rocca-Volmerange B., Prugniel P., Lançon A., Fioc M., Soubiran C., 2004, A&A, 425, 881
Longhetti M., Saracco P., 2009, MNRAS, 394, 774
Longhetti M. et al., 2007, MNRAS, 374, 614
Martín-Navarro I. et al., 2015, ApJ, 798, L4
Martinez-Manso J. et al., 2011, ApJ, 738, L22 (MM11)
Muzzin A., Marchesini D., van Dokkum P. G., Labbé I., Kriek M., Franx M., 2009, ApJ, 701, 1839
Newman A. B., Ellis R. S., Treu T., Bundy K., 2010, ApJ, 717, L103
Newman J. A. et al., 2013, ApJS, 208, 5
Peralta de Arriba L., Balcells M., Falcón-Barroso J., Trujillo I., 2014, MNRAS, 440, 1634 (PdA14)
Pérez-González P. G. et al., 2008, ApJ, 675, 234
Ragone-Figueroa C., Granato G. L., 2011, MNRAS, 414, 3690
Renzini A., 2006, ARA&A, 44, 141
Ruiz P., Trujillo I., Mármol-Queraltó E., 2014, MNRAS, 442, 347
Salpeter E. E., 1955, ApJ, 121, 161
Shen S., Mo H. J., White S. D. M., Blanton M. R., Kauffmann G., Voges W., Brinkmann J., Csabai I., 2003, MNRAS, 343, 978
Stockton A., Shih H.-Y., Larson K., 2010, ApJ, 709, L58
Stockton A., Shih H.-Y., Larson K., Mann A. W., 2014, ApJ, 780, 134
Tapia T. et al., 2015, submitted
Taylor E. N., Franx M., Brinchmann J., van der Wel A., van Dokkum P. G., 2010, ApJ, 722, 1
Toft S. et al., 2007, ApJ, 671, 285
Treu T., Auger M. W., Koopmans L. V. E., Gavazzi R., Marshall P. J., Bolton A. S., 2010, ApJ, 709, 1195
Trujillo I., Burkert A., Bell E. F., 2004, ApJ, 600, L39
Trujillo I. et al., 2006, MNRAS, 373, L36
Trujillo I., Conselice C. J., Bundy K., Cooper M. C., Eisenhardt P., Ellis R. S., 2007, MNRAS, 382, 109 (T07)
Valdes F., Gupta R., Rose J. A., Singh H. P., Bell D. J., 2004, ApJS, 152, 251
van de Sande J. et al., 2013, ApJ, 771, 85
van der Wel A., Holden B. P., Zirm A. W., Franx M., Rettura A., Illingworth G. D., Ford H. C., 2008, ApJ, 688, 48
van Dokkum P. G., Kriek M., Franx M., 2009, Nature, 460, 717
York D. G. et al., 2000, AJ, 120, 1579
Zirm A. W. et al., 2007, ApJ, 656, 66

APPENDIX A: SKY SUBTRACTION IN THE DATA REDUCTION

The most critical step of our data reduction was the sky subtraction. The reason of this trouble is based on the presence of many narrow lines of sky emission on the near-infrared. In order to try to get the best possible results on this step, we developed the new software tool PYKELSAME, which implements the sky-subtraction method proposed by Kelson (2003) in the environment of REDUCEME.

In addition, in the development of PYKELSAME we found the necessity of coding other two auxiliary tools: REDUCIO and PYSDISTOR. REDUCIO is a simple module which allows to read and write files with the format of REDUCEME in a PYTHON environment (REDUCEME has its own format because it was designed in the 90s and then the speed of reading and writing the data played an important role). The function of PYSDISTOR is to trace the spectrum of faint targets (or any) in the CCD. The algorithm of this last tool is simple: to trace the spectrum adding several channels (i.e. pixels along the spectral direction) to make easier to detect a faint object.

Once we developed these two auxiliary tools, we implemented the sky-subtraction method proposed by Kelson (2003). Fig. A1 illustrates the idea of this method: once we have characterized the C-distortion of the CCD (but not corrected it), we can use all the rows of the CCD to build a high-resolution spectrum of the sky. Fig. A1 shows how by using every pixel of the image without rebinning (left-hand panel) we can build a high-resolution spectrum (black thin line on the right-hand panel) compared with the spectrum extracted from a single row (red thick line on the right-hand panel). It is worth noting the presence a cosmic ray in the high-resolution spectrum of this figure: it is an example of an issue which has to be solved in the construction of the sky model.

Fig. A2 illustrates the process of the construction of the sky model. In top panel, we show the first step: the CCD region to be considered in the modelling. We checked that our results improve selecting a CCD region around the target but excluding the region affected by the target spectrum (we detected the target spectrum using PYSDISTOR); the dashed lines in the top panel show the excluded region. The middle panel shows the high-resolution spectrum built from the CCD region using the technique explained in the previous paragraph. It is worth noting the existence of cosmic rays in this spectrum. To reject these points, the sky model is constructed as follows: we clean the high-resolution spectrum using a median filter (or any other percentile if it was desired), and we used this clean spectrum to interpolate linearly at a desired wavelength (the clean spectrum is highly sampled, so it is not necessary a higher order interpolation). This sky model has been plotted in the bottom panel.

Fig. A3 illustrates process of the sky subtraction. The top panel is the raw CCD subsection used to build the sky model. The middle panel is the evaluation of the sky model in the pixels of the raw CCD. We can check how to the cosmic rays and the target spectrum have disappeared (as it was desired). The bottom panel shows the sky-subtracted CCD. Notice that the cosmic rays are still present in the CCD, but as the sky lines have been removed, it is easier to detect them (so afterwards it will be easier to remove them).

Fig. A4 compares the sky-subtraction method used in this paper with the traditional technique. Both of them have been performed in the environment of REDUCEME (using PYKELSAME and SKYSUBM programs, respectively). According to the above descriptions, the key difference between these methods is the order of subtracting sky and correcting C-distortion. For better comparison, we have

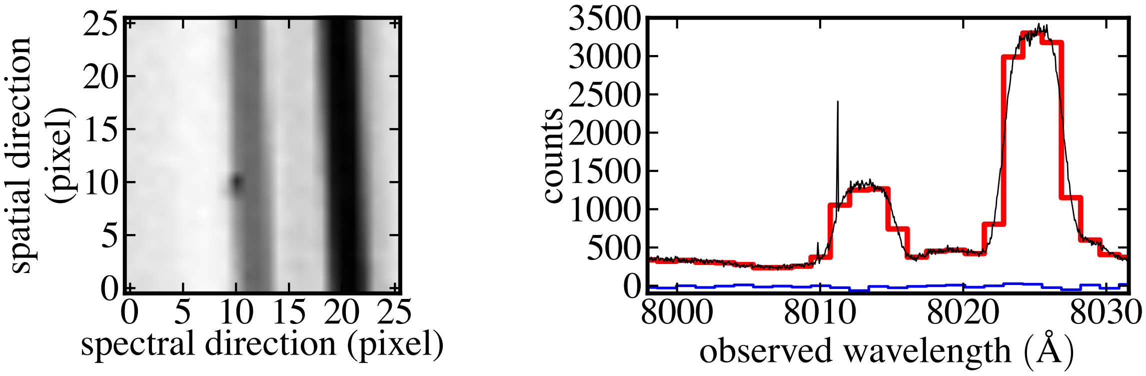

Figure A1. In the left-hand panel, we show a CCD subsection with two night-sky emission lines. In the right-hand panel, we show two spectra for these lines: one from a single CCD row (red thick line), and other using all the rows of the CCD subsection (black thin line). Note that the spectrum from all the rows of the CCD subsection takes advantage of the C-distortion for getting a spectrum more sampled than the other from single CCD row. Bottom blue medium-width line shows the residuals in the CCD row of the red thick line after the subtraction of sky model constructed from all the rows of the CCD subsection.

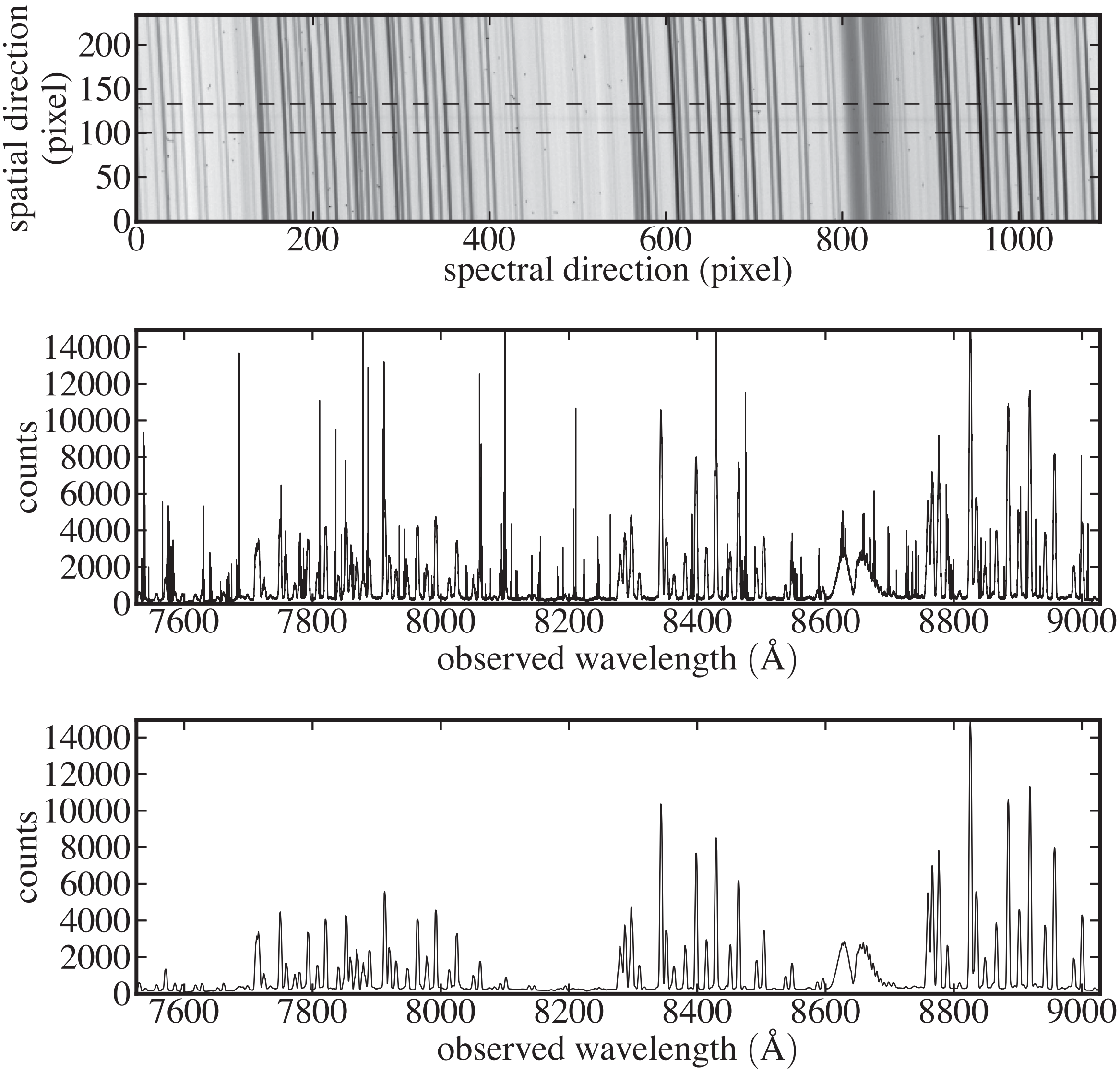

Figure A2. Top panel shows a CCD subsection; the two dashed lines indicate the region excluded for the sky modelling due to the presence of the target spectrum. Middle panel shows the spectrum build from the CCD subsection of the top panel taking advantage of the C-distortion. In bottom panel, we plot the sky model derived from the spectrum of the middle panel.

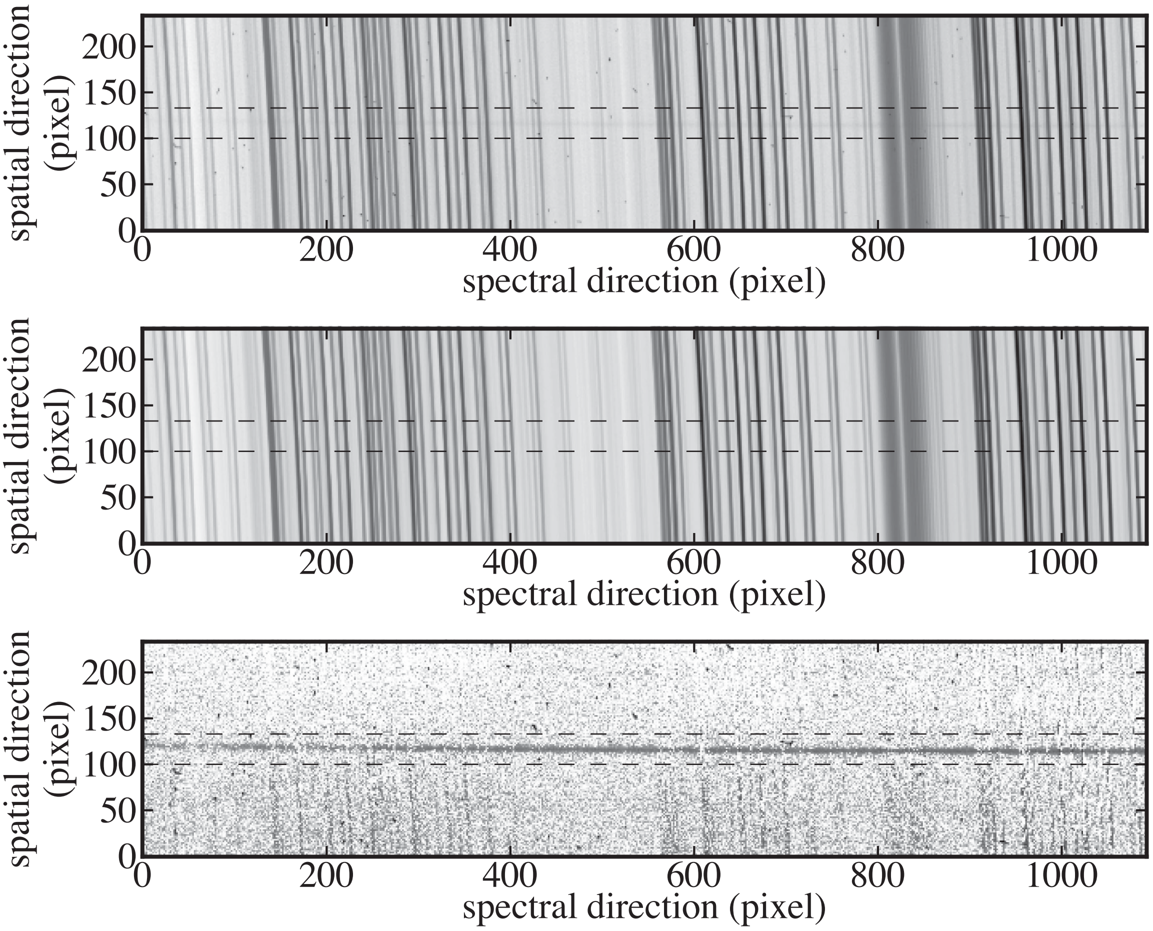

Figure A3. Top panel shows a raw CCD subsection. Middle panel shows the sky model for the CCD subsection. Bottom panel shows the CCD subsection after the sky subtraction. In each panel, dashed lines indicate the region near to the target excluded for building the sky model. Top and middle panels share the same colour bar (from 55 to 14 409 counts), while another colour bar used for bottom panel (from 0.1 to 1000 counts).

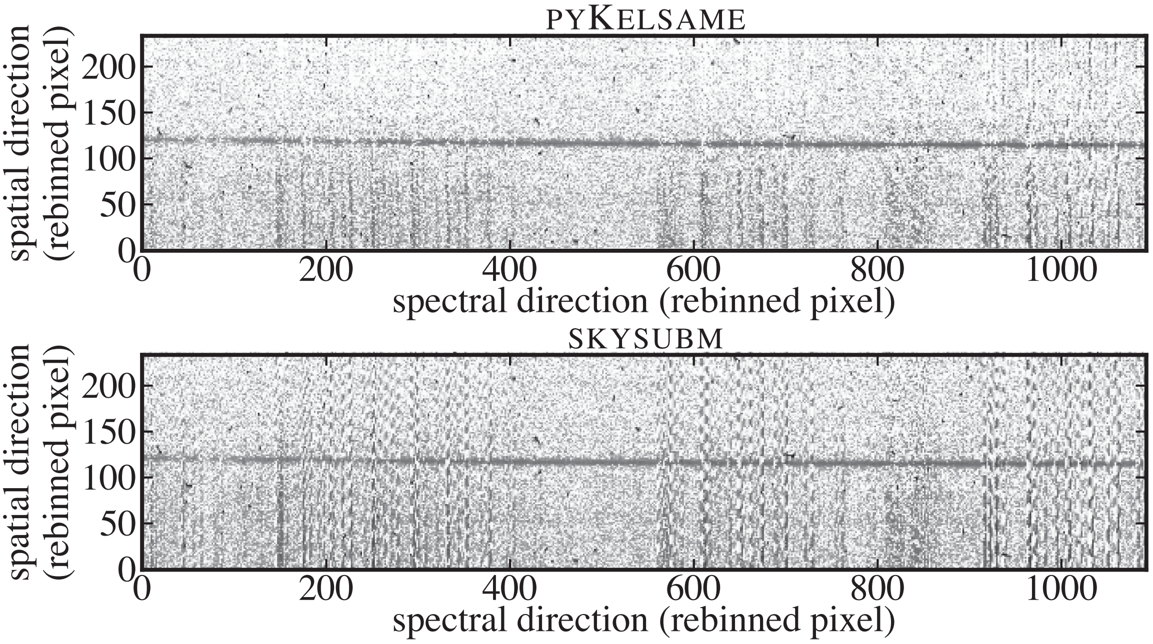

Figure A4. Top/bottom panel shows a CCD subsection where the sky subtraction was performed before/after correcting the C-distortion and using the pyKelsame/skysubm program. Both panels share the same colour bar (from 0.1 to 1000 counts).

also corrected the C-distortion in the panel of Fig. A4 which shows the sky subtraction with pyKelsame: this allows that both panels display rebinned data. Checking the intensity of residuals after sky subtraction, Fig. A4 confirms that the method explained in this appendix reports better results than the traditional technique.

APPENDIX B: ROBUSTNESS OF THE VELOCITY DISPERSION MEASUREMENTS

A number of tests indicate that the velocity dispersions and their errors are robust.

We obtained velocity dispersions for different combinations of SSP templates. In particular, we repeated the pPXF fits:

(i) Using the SSPs from the library with ages younger than age of the Universe at $z = 1$.

(ii) Using the SSPs from the library with ages younger than age of the Universe at $z = 1$ and the option of regularization of pPXF.

(iii) Using the whole SSP library.

(iv) Using the whole SSP library, and masking H γ and H δ lines.

(v) Using the single SSP which alone best fits each spectrum.

For all galaxies, the results from all the tests were in agreement with each other within their errors, being the mean standard deviation 9 $\mathrm{km\,s^{-1}}$. In the case (iii), we tested for the possibility that residual emission might be partially filling the H γ and H δ lines; because most of our spectra do not reach the [O II] 3727 Å line, star formation could easily go unnoticed and affect the velocity dispersion measurements. We therefore compared our results with those from fits in which these lines were masked out.

We further tested out velocity dispersion results by carrying out the pPXF fits using a stellar library instead of SSPs. We used a library with 193 stars from the Indo-US Library of Coudé Feed Stellar Spectra (Valdes et al. 2004). The selection of stars was performed to cover a wide range of effective temperatures, metallicities and surface gravities. This library was chosen because its high spectral resolution (1.36 Å FWHM) allows us to take advantage of the quality of our spectra (~2 Å FWHM at rest frame). The stellar library has the disadvantage of being less physical motivated, but, on the other hand, it provides wider spectral coverage by reaching down to 3460 Å, as compared to the PÉGASE-HR SSP library, which cuts at 3900 Å. These fits were carried out masking and without masking H γ and H δ lines. In all these cases, we obtain similar results: the mean of the differences is 0 and their standard deviation is 7 $\mathrm{km\,s^{-1}}$.

The results from fitting stellar templates are very similar to those from SSPs for four of the galaxies. For the other two, the fits with stellar templates give lower, marginally inconsistent dispersions. Specifically, for the galaxy ID 13018611, we obtained $\sigma = 118 \pm 22\,\mathrm{km\,s^{-1}}$ using the stellar library and $\sigma = 151 \pm 15\,\mathrm{km\,s^{-1}}$ using SSPs (not masking the H γ and H δ lines in both cases). Similarly, for the galaxy ID 12028173, using the stellar library we obtained 180 ± 8 and 214 ± 16 $\mathrm{km\,s^{-1}}$ using SSPs (bootstrap errors). As discussed in Section 3.3, we believe the fits to stellar templates are more uncertain given the intrinsic width of the Ca II H and K lines for some stellar temperatures, and hence we choose the solutions given by SSP fits. Nevertheless, adopting the dispersions obtained with stellar templates would not change the conclusions from this work.

Finally, we have compared our results with those from other authors. We have the galaxy ID 12024790 in common with MM11. That authors reports $\sigma_\mathrm{e} = 160 \pm 10\,\mathrm{km\,s^{-1}}$, which is significantly lower than our value, $\sigma_\mathrm{e} = 261 \pm 15\,\mathrm{km\,s^{-1}}$. Applying the masking they use to exclude regions affected by telluric absorption, and cutting the redder part of our spectrum to their red cut-off we could not reproduce their result: we obtained $\sigma_\mathrm{e} = 258 \pm 22\,\mathrm{km\,s^{-1}}$. In order to explore the origin of the difference, we repeated the measurement over the MM11 spectrum (albeit without relative-flux calibration) using pPXF and the above libraries (PÉGASE-HR and Indo-US). Using the PÉGASE-HR library, we performed the fit for a wide range (1–13) of degrees of the Legendre polynomial used to correct the continuum shape and found a strong dependence with this parameter obtaining values from 198 to 310 $\mathrm{km\,s^{-1}}$. Doing the same exercise with the Indo-US library, we did not find a clear dependence with the polynomial degree and the results cover a narrower range: 227–259 $\mathrm{km\,s^{-1}}$. We also performed these tests in our spectrum for this galaxy (using the same wavelength ranges and masking the same regions), and obtained the ranges 250–264 and 239–277 $\mathrm{km\,s^{-1}}$ for PÉGASE-HR and Indo-US libraries, respectively. All these tests except one produce stable results similar to our measurement, while the unstable test corresponds to a similar situation to the published by MM11: their spectrum and SSP templates. Additional checks on our own spectra included a verification of the instrumental dispersion and its variation from night to night: measurement of the width of the telluric lines in the region of the kinematic signatures shows a very stable configuration (3.88 ± 0.06 Å FWHMs). We conclude that the origin of the difference with MM11 is unclear, and might be related to the use of different velocity dispersion algorithms; we have used our measurement in the paper.

We share the galaxy ID 13018611 with the sample of Fernández Lorenzo et al. (2011). For this galaxy, they report $\sigma_\mathrm{e} = 196 \pm 6\,\mathrm{km\,s^{-1}}$, while we find $\sigma_\mathrm{e} = 161 \pm 16\,\mathrm{km\,s^{-1}}$. Their velocity dispersion measurement shows a dependence on the spectral range of the fit: 173 $\mathrm{km\,s^{-1}}$ for the range 3829–4129 Å, 184 $\mathrm{km\,s^{-1}}$ for 3775–4178 Å and 195 $\mathrm{km\,s^{-1}}$ for 3725–4227 Å (Fernández Lorenzo, private communication). The first of these three ranges is the closest to the one used by us, and, for that fitting range, the two determinations agree within the errors. In any case, the differences found show that the true uncertainties in the velocity dispersion determinations can be underestimated using the standard techniques (Monte Carlo simulations with white noise); this fact has been already proven by de Bruyne et al. (2003). We have used our value in the paper for consistency, and emphasize that using their value would not modify the conclusions of this work.

APPENDIX C: pPXF FITTING RESULTS

We show in Figs C1–C3 the spectra obtained after the data reduction explained in Section 3.2, together with the spectral fit obtained from pPXF detailed in Section 3.3.

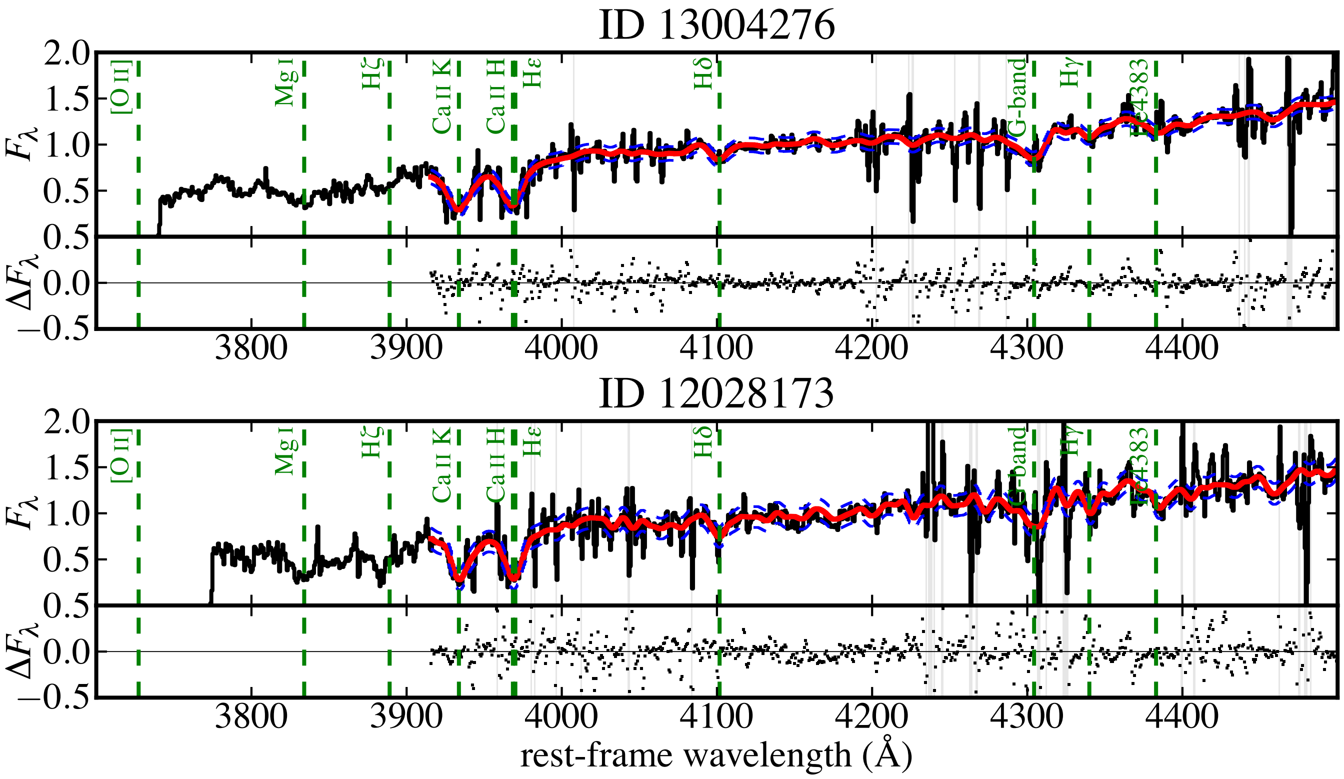

Figure C1. pPXF fitting results for the targets in the slit 1 of the observations. On top panels black thin solid lines show the spectra, red thick solid lines represent pPXF fits, and blue dashed lines are 1σ deviations from the pPXF fits. On bottom panels we have plotted the residuals with black dots. Units are arbitrary. Grey regions indicate those which were masked in the pPXF fits. We have marked some spectral features with green dashed vertical lines.

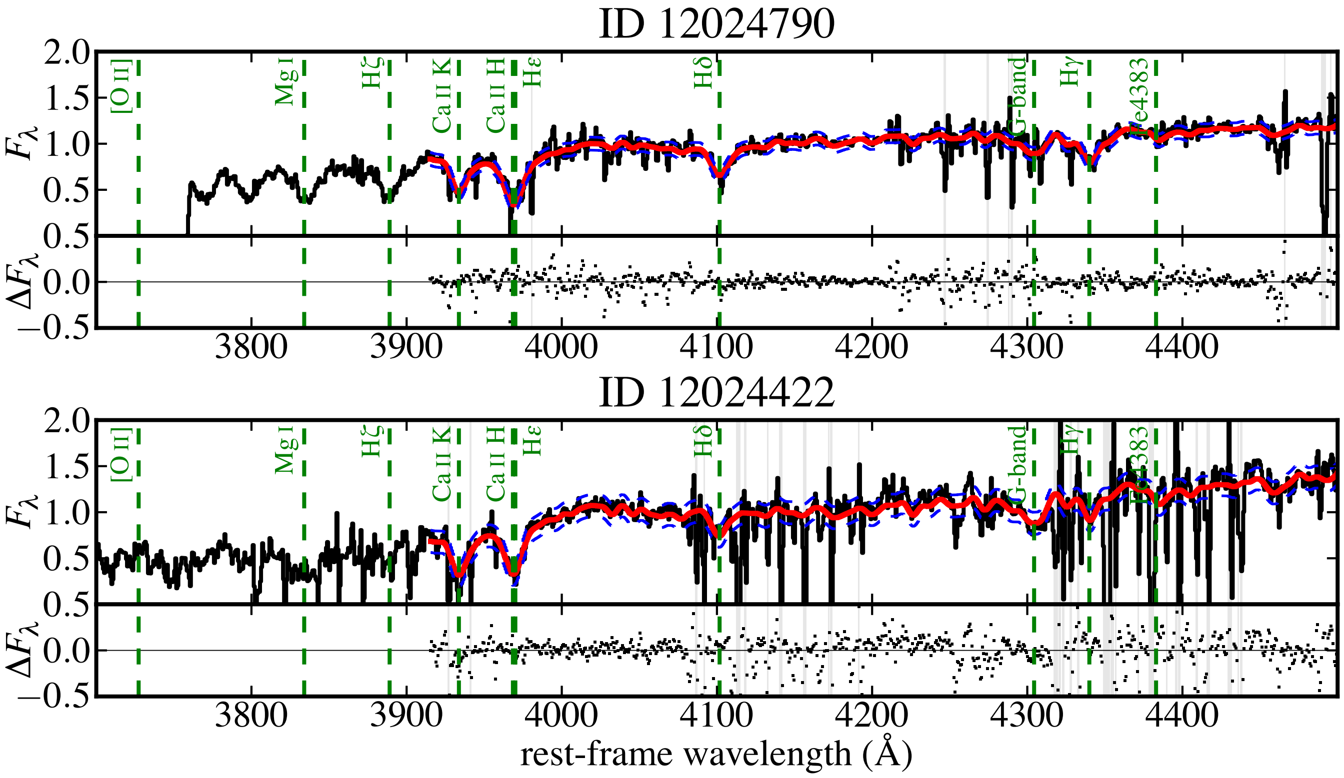

Figure C2. pPXF fitting results for the targets in the slit 2 of the observations. On top panels black thin solid lines show the spectra, red thick solid lines represent pPXF fits, and blue dashed lines are 1σ deviations from the pPXF fits. On bottom panels we have plotted the residuals with black dots. Units are arbitrary. Grey regions indicate those which were masked in the pPXF fits. We have marked some spectral features with green dashed vertical lines.

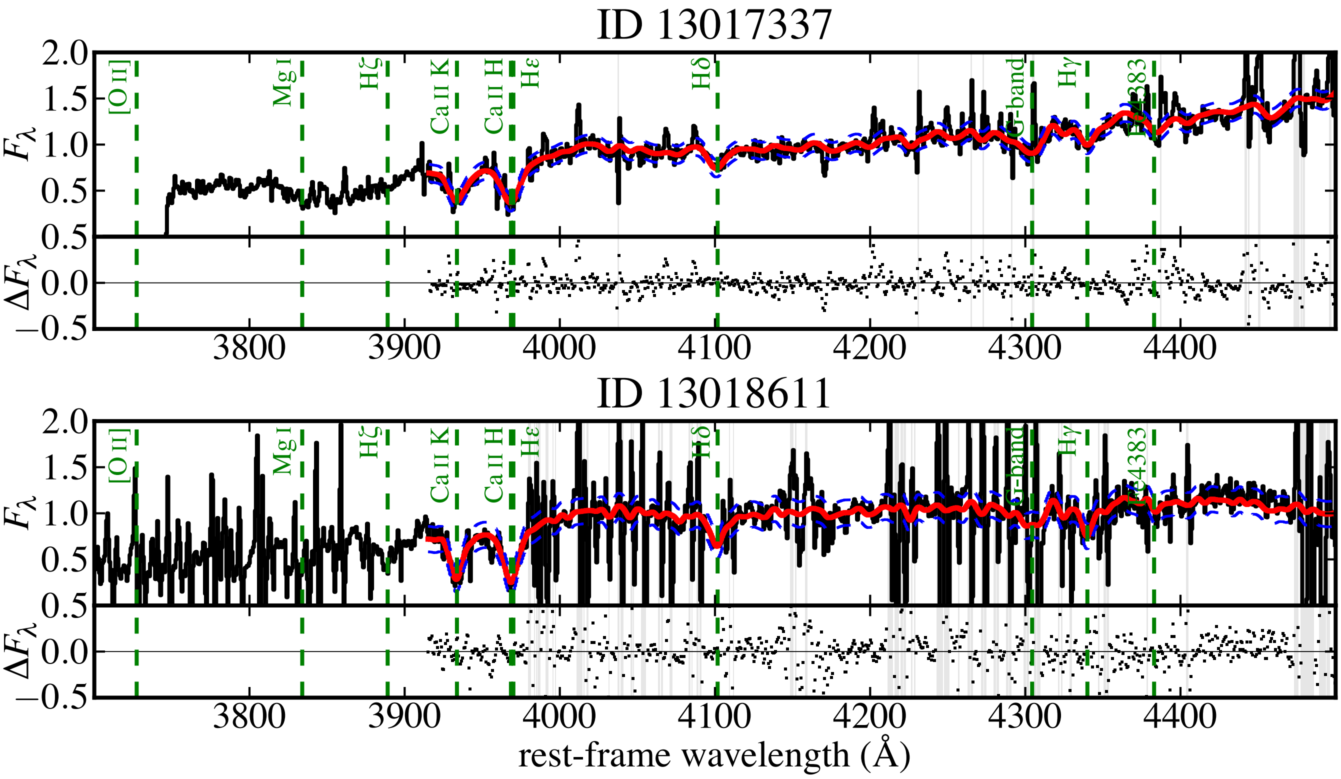

Figure C3. pPXF fitting results for the targets in the slit 3 of the observations. On top panels black thin solid lines show the spectra, red thick solid lines represent pPXF fits, and blue dashed lines are 1σ deviations from the pPXF fits. On bottom panels we have plotted the residuals with black dots. Units are arbitrary. Grey regions indicate those which were masked in the pPXF fits. We have marked some spectral features with green dashed vertical lines.

APPENDIX D: STRUCTURAL PARAMETERS FOR THE $z \sim 1$ SAMPLE

Table D1 contains a compilation of structural parameters for the sample of massive ETGs at $z \sim 1$ analysed in this paper.

Table D1. Compilation of structural parameters for the $z \sim 1$ sample. (1) References: [0] this work; [1] Martinez-Manso et al. (2011); [2] Belli et al. (2014); [3] Newman et al. (2010) (extracted from the compilation made by van de Sande et al. 2013); [4] van der Wel et al. (2008) and Blakeslee et al. (2006) (extracted from the compilation made by van de Sande et al. 2013). (2) Galaxy identifications as given in the references. (3) Spectroscopic redshifts. (4) Sérsic indices. (5) Circular effective (half-light) radii. (6) Stellar masses (adapted to Salpeter IMF). (7) Velocity dispersions within the effective (half-light) radius.

Reference (1)	ID (2)	z (3)	n (4)	r_e (kpc) (5)	$M_\star$ (10^{11} M$_\odot$) (6)	σ_e (km s^{-1}) (7)
0	13004276	0.97533	5.1	1.46	2.0	340 ± 16
0	12028173	0.95764	5.9	1.42	1.2	228 ± 17
0	12024790	0.96572	4.4	0.54	0.9	261 ± 15
0	12024422	1.02874	4.8	1.57	1.2	239 ± 18
0	13017337	0.97242	4.3	1.37	1.8	291 ± 25
0	13018611	1.07939	4.7	1.19	3.0	161 ± 16
1	12024321	0.91592	6.5	2.46	0.9	162 ± 12
1	12019899	0.93259	6.3	0.47	1.1	245 ± 18
1	12024453	0.90564	4.8	1.60	1.7	184 ± 10
2	51106	1.013	5.3	5.99	3.3	252 ± 37
2	28739	1.029	3.5	1.98	1.6	238 ± 11
2	54891	1.081	3.2	1.27	1.0	232 ± 37
2	31377	1.085	4.9	4.88	1.2	133 ± 18
2	13393	1.097	3.5	7.18	2.6	175 ± 21
2	16343	1.098	8.0	1.95	2.0	290 ± 8
3	E1	1.054	4.0	6.44	2.1	204 ± 22
4	761	1.01	4.0	3.77	6.2	377 ± 40
4	1559	0.94	4.0	1.66	1.1	179 ± 13
4	1706	0.91	4.0	2.23	2.7	217 ± 13
4	1	1.09	4.0	2.83	2.7	233 ± 17
4	2	0.96	4.0	2.30	3.5	202 ± 10
4	3	1.04	4.0	1.00	1.2	302 ± 34
4	4	0.96	4.0	6.84	7.8	337 ± 19
4	13	0.98	4.0	2.20	3.2	249 ± 11
4	14	0.98	4.0	2.80	1.4	199 ± 24
4	18	1.10	4.0	3.97	5.7	327 ± 37
4	20	1.02	4.0	2.24	2.6	201 ± 17

This paper has been typeset from a TEX/LATEX file prepared by the author.

5

Massive relic galaxies prefer dense environments

The material included in this chapter has already been published by Peralta de Arriba et al. (2016). This article has been accepted for publication in Monthly Notices of the Royal Astronomical Society ©: 2016 Luis Peralta de Arriba, Vicent Quilis, Ignacio Trujillo, María Cebrián and Marc Balcells. Published by Oxford University Press on behalf of the Royal Astronomical Society. All rights reserved.

DOI: 10.1093/mnras/stw1240

Massive relic galaxies prefer dense environments

Luis Peralta de Arriba,[1,2,3]★ Vicent Quilis,[4,5]★ Ignacio Trujillo,[2,3] María Cebrián[2,3] and Marc Balcells[1,2,3]

[1]*Isaac Newton Group of Telescopes, E-38700 Santa Cruz de La Palma, La Palma, Spain*
[2]*Universidad de La Laguna, Departamento de Astrofísica, E-38206 La Laguna, Tenerife, Spain*
[3]*Instituto de Astrofísica de Canarias (IAC), E-38205 La Laguna, Tenerife, Spain*
[4]*Departament d'Astronomia i Astrofísica, Universitat de València, E-46100 Burjassot, València, Spain*
[5]*Observatori Astronòmic, Universitat de València, E-46980 Paterna, València, Spain*

Accepted 2016 May 20. Received 2016 May 19; in original form 2016 March 17

ABSTRACT

We study the preferred environments of $z \sim 0$ massive relic galaxies ($M_\star \gtrsim 10^{10}\,\mathrm{M}_\odot$ galaxies with little or no growth from star formation or mergers since $z \sim 2$). Significantly, we carry out our analysis on both a large cosmological simulation and an observed galaxy catalogue.

Working on the Millennium I-*WMAP*7 simulation we show that the fraction of today massive objects which have grown less than 10 per cent in mass since $z \sim 2$ is ∼0.04 per cent for the whole massive galaxy population with $M_\star > 10^{10}\,\mathrm{M}_\odot$. This fraction rises to ∼0.18 per cent in galaxy clusters, confirming that clusters help massive galaxies remain unaltered. Simulations also show that massive relic galaxies tend to be closer to cluster centres than other massive galaxies.

Using the New York University Value-Added Galaxy Catalogue, and defining relics as $M_\star \gtrsim 10^{10}\,\mathrm{M}_\odot$ early-type galaxies with colours compatible with single-stellar population ages older than 10 Gyr, and which occupy the bottom 5-percentile in the stellar mass–size distribution, we find 1.11 ± 0.05 per cent of relics among massive galaxies. This fraction rises to 2.4 ± 0.4 per cent in high-density environments.

Our findings point in the same direction as the works by Poggianti et al. and Stringer et al. Our results may reflect the fact that the cores of the clusters are created very early on, hence the centres host the first cluster members. Near the centres, high-velocity dispersions and harassment help cluster core members avoid the growth of an accreted stellar envelope via mergers, while a hot intracluster medium prevents cold gas from reaching the galaxies, inhibiting star formation.

Key words: galaxies: evolution – galaxies: formation – galaxies: fundamental parameters – galaxies: haloes – galaxies: structure – dark matter.

1 INTRODUCTION

Using cosmological simulations of galaxy formation, Quilis & Trujillo (2013) show that a small fraction (∼1 per cent) of $M_\star \gtrsim 10^{11}\,\mathrm{M}_\odot$ galaxies already formed at $z > 2$ are expected to have grown in mass by less than 10 per cent since that epoch, i.e. they have remained essentially unaltered by mergers, accretion and star formation since $z \sim 2$. This number implies that, in the present-day Universe, ∼0.2 per cent of massive galaxies should be relic galaxies, with a number density of $\sim 10^{-6}\,\mathrm{Mpc}^{-3}$. The observational search for $z \sim 0$ massive relic galaxies has been inconclusive to date. Trujillo et al. (2009) and Taylor et al. (2010), using the Sloan Digital Sky Survey (SDSS), report only an upper limit of $< 10^{-7}\,\mathrm{Mpc}^{-3}$ for the number density of massive relic galaxies up to $z \approx 0.1$. In contrast, Valentinuzzi et al. (2010), looking in clusters and including lower-mass galaxies, report a large number of massive relic candidates. The latter results raise the question of whether high-density environments (where the SDSS spectroscopic incompleteness is expected to be severe) are particularly favourable for the conservation of massive relic galaxies. It is worth noting that our firmest candidate to be a genuine massive relic galaxy, NGC 1277 (Trujillo et al. 2014), inhabits the central region of the Perseus galaxy cluster. This massive cluster (with a velocity dispersion of 1282^{+95}_{-78} km s^{-1}; Danese, de Zotti & di Tullio 1980) is known for being the brightest cluster in X-ray emission of the sky (Edge, Stewart & Fabian 1992).

From the theoretical point of view, the location of massive relic galaxies as a function of the environment was explored by Stringer et al. (2015). These authors used the characteristics of the dark matter halo of NGC 1277 as a reference for studying, in the BOLSHOI simulation, where galaxies like NGC 1277 are located. They found that dark matter haloes like that of NGC 1277 are substructures of

---

★E-mail: peralta@ing.iac.es (LPdA); vicent.quilis@uv.es (VQ)

other more massive dark matter haloes. For dark matter haloes corresponding to the richest galaxy clusters, the fraction of sub-haloes similar to the dark matter halo of NGC 1277 can be as high as 30 per cent.

From the observational side, the location of old (with luminosity ages >9 Gyr) superdense galaxies as a function of the environment was explored by Poggianti et al. (2013). Using PM2GC (Calvi, Poggianti & Vulcani 2011) and WINGS (Valentinuzzi et al. 2010) samples, these authors found that nowadays a significant fraction (at least 17 per cent) of these objects should be found in clusters. They also reported that this result was in agreement with the theoretical expectations derived from their own analysis of the Millenium Simulation. For instance, they found 36 per cent of the galaxies with $M_\star > 5 \times 10^{10}$ M$_\odot$ and already passive at $z = 1.6$ are members of clusters.

Understanding whether there is any preferential location for massive relic galaxies is key to have a comprehensive picture of the mechanisms responsible of the growth of the massive galaxy population with cosmic time (e.g. Naab, Johansson & Ostriker 2009; Ferreras et al. 2014; Peralta de Arriba et al. 2015). In particular, understanding whether massive relic galaxies inhabit a particular type of environment is key to identifying the physical processes that prevented the size evolution of these objects.

In this paper we provide a new determination of which environment is most favourable for massive relic galaxies. We improve over previous works by conducting a simultaneous analysis of the predictions from numerical simulations and observational data, using the same methodology for characterizing the environment around massive galaxies. In addition, we work with baryonic galaxies instead of just dark matter haloes. Given the low number density of massive relic galaxies in the present-day Universe, we use one of the currently largest *N*-body cosmological simulation: the Millennium I-*WMAP*7 (MI7; Guo et al. 2013), and we extend the mass range of the search to lower masses ($M_\star \gtrsim 10^{10}$ M$_\odot$): there is no reason to believe relics only exist above $M_\star \gtrsim 10^{11}$ M$_\odot$, and the change improves the statistics that can be extracted from the simulations and the observational data.

The paper is structured as follows. In Section 2 we describe our numerical galaxy catalogue, we state the definition of which galaxies will be considered as relics in the simulations (Section 2.1), and how we have identified galaxy clusters into them (Section 2.2). In Section 3 we introduce our observational catalogue, and define which galaxies will be considered relics within this catalogue (Section 3.1). In Section 4 we detail the procedure that we use to characterize the environment of the galaxies in both frameworks (simulations and observations). Our results are shown in Section 5, splitting them according they come from simulations (Section 5.1) or observations (Section 5.2). In Section 6 we discuss our results, while in Section 7 we summarize our conclusions.

2 NUMERICAL GALAXY CATALOGUE

The catalogue of simulated galaxies is based on the public release of a very large *N*-body simulation (MI7; Guo et al. 2013). MI7 is a version of the original Millennium I (Springel et al. 2005) simulation run using the seven-year *WMAP* data (Komatsu et al. 2011). The cosmological parameters for MI7 simulation are: $\Omega_\mathrm{m} = 0.272$, $\Omega_\mathrm{b} = 0.045$, $\Omega_\Lambda = 0.728$, $n = 0.961$, $\sigma_8 = 0.807$, $H_0 = 70.4$ km s^{-1} Mpc^{-1}. The simulation uses 2160^3 particles in a computational box that has sides of 710 Mpc. The particle mass is 1.32×10^9 M$_\odot$.

A combination of two halo finders, a friends-of-friends (FoF) algorithm by Davis et al. (1985) and SUBFIND (Springel et al. 2001), is used in order to analyse the simulations and to build up the dark matter merger trees. The dark matter haloes found in the *N*-body simulations are transformed into galaxies according to the semi-analytical model of Guo et al. (2013), available in the Millennium data base webpage (Lemson & Virgo Consortium 2006).

Guo's model (Guo et al. 2013) implements several new features with respect to previous ones (i.e. De Lucia & Blaizot 2007): the separate evolution of sizes and orientations for gaseous and stellar discs, the size evolution of spheroids, tidal and ram-pressure stripping of satellite galaxies, and the disruption of galaxies to produce intra-cluster light. The effects of AGN feedback are also included. The stellar masses of the semi-analytical galaxies are estimated assuming a Chabrier (2003) initial-mass function (IMF), also used in the observational galaxy catalogue described later in Section 3.

We generate our parent galaxy catalogue using the Millennium data base webpage by selecting all galaxies with $z \sim 0$ stellar masses between 10^{10} and 10^{13} M$_\odot$.

2.1 Definition of a relic galaxy in the simulation

We define a $z \sim 0$ relic in the simulation as a galaxy that has barely increased its stellar mass since $z \sim 2$. In order to identify the possible candidates to relic galaxies in our numerical catalogue, we use the merger tree structures to trace backwards in time the massive galaxies identified at $z \sim 0$, together with two conditions.

(i) The galaxy must be already formed at $z \sim 2$, namely, it must be identified by the halo finder algorithm as a group of gravitationally bound particles. In our particular implementation, and in order to ensure that the galaxies are numerically well resolved, only galaxies with stellar masses larger that 10^9 M$_\odot$ are considered.

(ii) The stellar mass of the $z \sim 2$ precursor is higher than the 90 per cent of the $z \sim 0$ mass.

2.2 Identification of galaxy clusters in the simulation

The next step in our procedure uses a simplified version of the idea of the spherical over-density halo finders (see e.g. Planelles & Quilis 2009) to identify the possible candidates to be a virialized galaxy cluster in the sample. The basic concept of this technique is to find spherical regions with an average density above a certain threshold, which can be fixed according to the spherical top-hat collapse model. Therefore, we can define the virial mass of a halo (M_vir) as the mass enclosed in a spherical region of radius (r_vir) having an average density Δ_c times the critical density $\rho_\mathrm{c}(z) = 3H(z)^2/8\pi G$:

$$M_\mathrm{vir}(< r_\mathrm{vir}) = \frac{4}{3}\pi r_\mathrm{vir}^3 \Delta_\mathrm{c}\rho_\mathrm{c}. \quad (1)$$

The over-density Δ_c depends on the adopted cosmological model, and can be approximated by the following expression (Bryan & Norman 1998):

$$\Delta_\mathrm{c} = 18\pi^2 + 82x - 39x^2, \quad (2)$$

where $x = \Omega(z) - 1$ and $\Omega(z) = [\Omega_\mathrm{m}(1 + z)^3]/[\Omega_\mathrm{m}(1 + z)^3 + \Omega_\Lambda]$. Depending on the different cosmologies, typical values of Δ_c can vary between 100 and 500. For the particular choice of cosmological parameters of this paper, the value of Δ_c obtained using equation (2) is $\Delta_\mathrm{c} \simeq 350$.

In our particular implementation of a spherical over-density finder, and given the fact that we do not consider total masses but stellar masses, we use Δ_c to define a virialized region that has a stellar average density 350 times the average stellar density in the whole computational domain. For these computations, we consider the stellar masses from massive galaxies (i.e. those above $10^{10}\,\mathrm{M}_{\odot}$). With these conditions, we look for the galaxy whose spherical region has the highest average density. If this quantity divided by the average stellar density in the whole simulation is above the threshold $\Delta_c \simeq 350$, we define this region as a galaxy cluster. The procedure is repeated looking for the next galaxy whose associate sphere has an environmental density fulfilling the density threshold condition and non-overlapping with previously identified clusters. The procedure goes on until no candidates to galaxy cluster satisfying the conditions are left. Once all the galaxy clusters are identified, we characterize them by computing their velocity dispersion (σ) using the relative velocities with respect to the cluster centre of mass for all the galaxies in the cluster.

3 OBSERVATIONAL GALAXY CATALOGUE

Our sample of real galaxies is obtained from the New York University Value-Added Galaxy Catalogue (hereinafter NYU-VAGC; Blanton et al. 2005), which is based in the data release 7 of the Sloan Digital Sky Survey (hereafter SDSS-DR7; Abazajian et al. 2009). This catalogue contains about 2.5×10^6 objects with spectroscopic redshifts. In addition to photometric and spectroscopic information extracted from SDSS-DR7, the NYU-VAGC provides structural parameters, *K*-corrections and stellar mass estimates (derived using a Chabrier 2003 IMF; Blanton & Roweis 2007). Tabulated quantities that depend on the adopted cosmology were converted to the cosmology adopted in MI7 and *WMAP* (Section 2).

In order to avoid edge effects when exploring the environment of our real galaxies, we only consider the galaxies which live in the largest continuous volume of SDSS-DR7. In particular, we stay within the following region, which was originally proposed by Varela et al. (2012, cf. their section 2.2 and their fig. 2):

(i) Southern edge: $\delta > 0$.
(ii) Western edge: $\delta > 2.555\,556(-\alpha + 131^{\circ})$.
(iii) Eastern edge: $\delta > 1.709\,09(\alpha - 235^{\circ})$.
(iv) Northern edge: $\delta < \arcsin\left[\frac{0.932\,32\sin(\alpha-95.9^{\circ})}{\sqrt{1-[0.932\,32\cos(\alpha-95.9^{\circ})]^2}}\right]$.

Also, to get a mass-complete sample and guarantee that our definition of environment is homogeneous over the redshift interval of exploration, we constrain our sample to galaxies with redshifts between 0.005 and 0.060. According to equation (1) of Cebrián & Trujillo (2014, cf. also their figs 3 and 4), this redshift interval ensures that our sample will be complete for galaxies with stellar masses above $10^{10}\,\mathrm{M}_{\odot}$.

Selection biases of the SDSS spectroscopic catalogue affecting nearby, high-surface brightness galaxies have been carefully studied by Taylor et al. (2010). Specifically, they analysed the effects of the star/galaxy separation criterion, the ‘saturation’ selection limit and the ‘cross-talk’ selection limit. For the range of redshift of our sample, the most important effect is the ‘cross-talk’ selection limit. To first order, these selection biases are independent of environmental density, and consequently it is not expected that they affect our observational results. Nevertheless, and in order to show the robustness of these results, we will discuss about this issue in Section 6.

With the above restrictions, our observational catalogue is a mass-complete sample of 41 716 galaxies with $M_{\star} > 10^{10}\,\mathrm{M}_{\odot}$. From this sample, we classify 27 034 objects (65 per cent) as early-type galaxies on the basis of their Sérsic indices (i.e. $n > 2.5$), while 14 682 objects (35 per cent) are considered late-types (i.e. $n < 2.5$).

3.1 Definition of a relic galaxy in the observations

Identifying a relic galaxy in the observations is less straightforward than in simulations, as we have poor information on the merger and the star-formation histories of real galaxies. Using the criterion that a relic galaxy should not have undergone star formation since $z \sim 2$ and should not have evolved structurally since those redshifts, we require three conditions to classify a galaxy as a candidate relic:

(i) Its stellar population is old: equivalent single-stellar-population (SSP) age above 10 Gyr.
(ii) Its structure is early-type: with Sérsic index $n > 2.5$.
(iii) It is compact: its size must be close to stellar mass–size relationship of early types at $z \sim 2$.

To identify old galaxies, we select the reddest galaxies in the rest-frame colour–colour diagram $g - r$ versus $r - i$. We base our colour cut using a SSP model with age 10 Gyr and metallicity −0.25. The values adopted for this SSP were taken from the photometric predictions based on MIUSCAT spectral energy distributions (Ricciardelli et al. 2012; Vazdekis et al. 2010, 2012). Hence, we require $g - r > 0.763$ and $r - i > 0.363$. Additionally, and in order to minimize the contamination of dusty galaxies in our sample of relic galaxies, we reject the most asymmetric objects on the sky, i.e. those with a ratio between minor and major axes lower than 0.3, because they are the most probable candidates to be galaxies with dusty discs. We will expand about the contamination of dusty galaxies and the effectiveness of our rejection criteria on the discussion exposed in Section 6.

The structural requirements derive from the properties of massive galaxies at high redshift. Many works have shown that massive galaxies have grown with cosmic time (e.g. Daddi et al. 2005; Trujillo et al. 2007; Buitrago et al. 2008), being the size evolution stronger for early-type galaxies. Furthermore, stellar mass–size scaling relationship seems to have a constant slope with cosmic time. This result has been reported by van der Wel et al. (2014) up to $z \sim 3$, finding that the major-axis radius $R_{\mathrm{e,maj}}$ is proportional to $M_{\star}^{\beta}$ with $\beta \sim 0.75 \pm 0.05$ for early-type galaxies. In the nearby Universe the exponent is just slightly shallower. Shen et al. (2003) found that nearby early-type galaxies (i.e. with Sérsic index $n > 2.5$) are well described by a scaling relationship between their effective radii and stellar masses of the type $r_{\mathrm{e}} \propto M_{\star}^{\alpha}$ with $\alpha = 0.56$.

Taking advantage of the stronger global size evolution of early-type galaxies with cosmic time, we select our candidates for being relic galaxies as those objects with old stellar populations and Sérsic index n above 2.5 located in the lower region of the stellar mass–size plane. In particular, we define this lower region to contain 5 per cent of the whole sample of galaxies with the smaller sizes at each stellar mass. This means we consider as compact galaxies those with sizes below

$$r_{\mathrm{e}} = \lambda \left(\frac{M_{\star}}{10^{10}\,\mathrm{M}_{\odot}} \right)^{0.56}, \tag{3}$$

being $\lambda = 0.749$ kpc and r_{e} the effective radius in the r band.

We define a comparison sample of normal-sized galaxies by taking all galaxies between the 47.5 and 52.5 percentiles of the distribution $r_{\mathrm{e}}/M_{\star}^{0.56}$ of the whole sample (i.e. without any restriction on Sérsic-index). They are the galaxies which are between two lines in the stellar mass–size plane of the form of equation (3) with values of λ equal to $\lambda_1 = 1.502$ kpc and $\lambda_2 = 1.602$ kpc. In Fig. 1 we

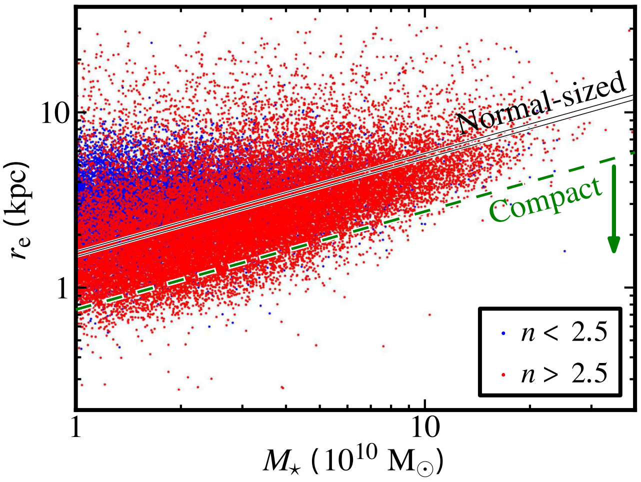

Figure 1. From the observational catalogue, distribution over the stellar mass–size plane of the galaxies. The green dashed line indicates the upper limit of the compact definition given in Section 3.1, while the two solid black lines show the region populated by the galaxies labelled as normal-sized in the same section. In addition, we have represented the galaxies with different colours depending on their Sérsic indices as indicated in the legend.

show how compact and normal-sized definitions are reflected in the stellar mass–size plane.

4 CHARACTERIZING THE DENSITY OF THE ENVIRONMENT

The same procedure is used to define environmental density in the simulations and in our real-galaxy catalogue. Following a similar prescription to that described in Cebrián & Trujillo (2014), we define the environmental density around each galaxy as follows: for each galaxy we identify all its neighbours with masses above $10^{10}\,\mathrm{M}_\odot$ within a sphere of radius $R = 0.5$ Mpc, and define the environmental density as follows:

$$\rho_i = \frac{1}{\frac{4}{3}\pi R^3}\sum_{k=1}^{N_i} M_{i,k}, \tag{4}$$

where $M_{i,k}$ is the stellar mass of the kth neighbour located at less than R of the ith galaxy of the sample (galaxy i has N_i neighbours). The selected radius of $R = 0.5$ Mpc is a compromise between having a local measurement of the density and at the same time having a volume large enough to guarantee that there is a significant number of galaxies above the stellar mass completeness limit so we can compute a sensible density around our targeted galaxy.

Although the same formal definition is used for both frameworks, density values from simulations and observations cannot be directly compared to each other. In the case of the real-galaxy catalogue, because the line-of-sight coordinate is inferred from the redshift, high-density virialized regions will be stretched along the line of sight (fingers-of-god effect) hence equation (4) provides a lower-limit to the actual physical density. However, it is worth noting that the computed densities for real galaxies have been proved to be a useful proxy to trace overdensities (e.g. Cooper et al. 2005; Haas, Schaye & Jeeson-Daniel 2012; Muldrew et al. 2012; Cebrián & Trujillo 2014). To emphasize this difference, we name the inferred quantity $\tilde{\rho}$ when it has been computed from the real-galaxy catalogue.

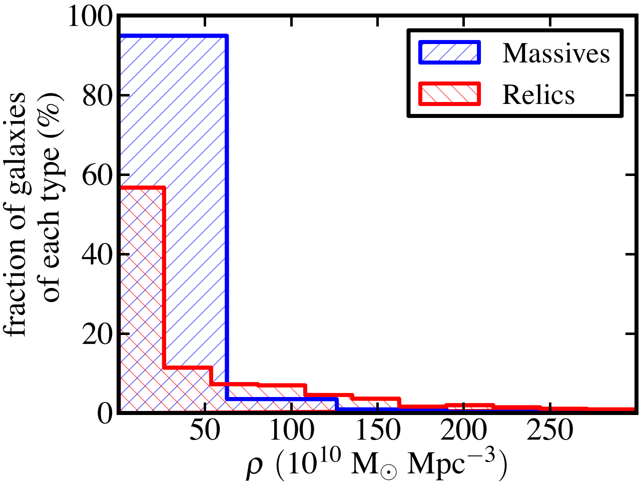

Figure 2. From the numerical catalogue, distribution of the environmental density of massive (blue) and relic (red) galaxies.

5 RESULTS

5.1 The location of relic galaxies according to the simulations

We use the catalogue of galaxies with stellar masses larger that $10^{10}\,\mathrm{M}_\odot$ extracted from the Millennium simulation. In this sample, we identify 1 850 648 massive galaxies ($M_\star > 10^{10}\,\mathrm{M}_\odot$) at $z \sim 0$. Among the subsample of massive galaxies, 742 galaxies can be labelled as relics according to the criteria described in Section 2.1. This number of relic galaxies corresponds to an extremely tiny fraction of today galaxies with $M_\star > 10^{10}\,\mathrm{M}_\odot$: 0.04 per cent. This value is lower than the measurement reported by Quilis & Trujillo (2013), where they found that the number of present-day massive relic galaxies is 0.06 per cent when they used our same catalogue (from Guo et al. 2013). We have checked that the above difference is only due to the higher mass cutoff ($M_\star > 8 \times 10^{10}\,\mathrm{M}_\odot$) of the Quilis & Trujillo (2013) sample.

We now direct our attention to the number of relic galaxies in clusters in the simulations. By using the method described in Section 2.2, we identify 672 rich galaxy clusters. Within these clusters, we find 47 646 massive galaxies and 87 relics (i.e. 0.18 per cent of them). Consequently, despite that the simulation has 8.5 times fewer relic galaxies in clusters than in the field, it follows that the probability for a massive galaxy to be a relic is 4.6 higher in clusters than in a global search of the population of massive galaxies.

5.1.1 The distribution of relic galaxies as a function of the environmental density

To make the analysis more quantitative, we explore the distribution of massive galaxies (relic and not) as a function of the environmental density as defined in equation (4). The distribution of ρ for the galaxies in the simulation is shown in Fig. 2. We see that the distribution of relics (red line) shows a more extended tail towards higher values than that of non-relic massive galaxies (blue line). This result points in the same direction as the above findings, where we report that the fraction of relics is higher in clusters.

5.1.2 Relics in clusters: velocity-dispersion distribution

In this section we explore how the massive (relic or not) galaxies are distributed according to the velocity dispersion of the clusters (i.e.

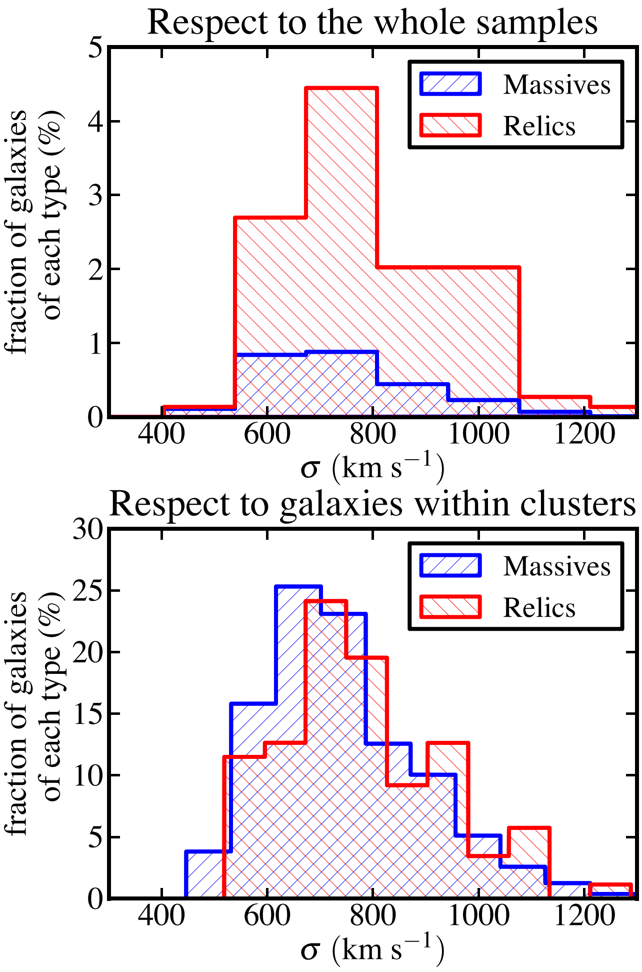

Figure 3. From the numerical catalogue, fraction of galaxies as a function of the velocity dispersion of the host galaxy cluster. Upper panel shows the fraction of each galaxy type with respect to the whole sample of massive galaxies (blue) and relics (red). Lower panel shows fractions referred to the amount of galaxies of each type which live within clusters.

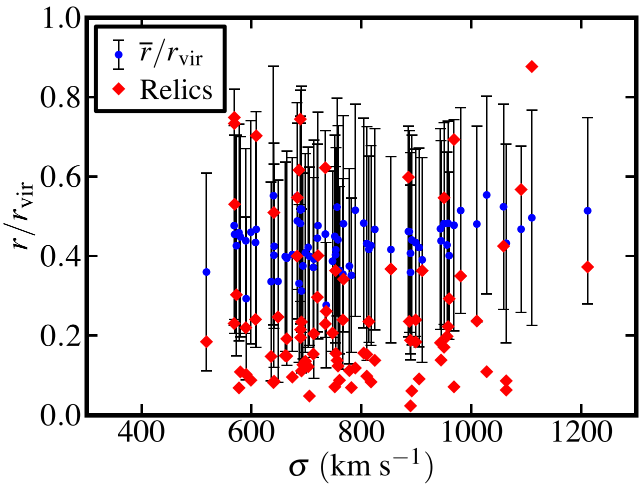

Figure 4. From the numerical catalogue, normalized radial position of relic galaxies in clusters (red diamonds) as a function of the velocity dispersion of the clusters, compared with the averaged radial positions $\bar{r}$ of all galaxies in each cluster (blue circles). Error bars represent one standard deviation for the radial distribution of the galaxies in a given cluster.

a proxy of the galaxy cluster global mass). The fraction of massive galaxies in clusters with respect to the total population of massive galaxies in our simulation is 2.6 per cent. Their distribution within the galaxy clusters is shown in upper panel of Fig. 3. Similarly, the fraction of relic galaxies in clusters with respect to the total population of relic galaxies in our simulation is 11.7 per cent and their distribution is shown in the same panel. In the upper panel of Fig. 3 the higher area from the histogram of relic galaxies reflects the higher probability for a massive galaxy to be a relic in rich clusters, while the ratio between the two histograms would give an analogue probability referred to each velocity-dispersion bin.

If we focus now our attention to the distributions considering the fractions with respect to the amount of galaxies of each type within the clusters, we can appreciate better whether there is any difference in the distribution of relic galaxies as a function of the velocity dispersion of the clusters. Bottom panel of Fig. 3 shows the result of this exercise. There is a small shift of the relic galaxies to higher velocity-dispersion values compared to the distribution of the other massive galaxies, i.e. the median in the distribution of the relics is 33 km s^{-1} higher. In order to guess if this difference is statistically significant, we performed a Kolmogorov–Smirnov test using both samples. Our result was a p-value of 0.055, which means that both distributions are marginally different.

5.1.3 Relics in clusters: radial distribution

Focusing on the subsample of galaxies in clusters, we enquire whether relic galaxies show any particular preference in their location within the cluster. Fig. 4 presents the radial location of the relics (red diamonds) in clusters against the cluster velocity dispersion. For the same clusters where the relics are located, we derive the mean $\bar{r}$ and the standard deviation of the radial distribution of all galaxies in the clusters. These are shown with blue circles with error bars. Comparing the radial location of the relics with the average position of the galaxies, we see that most of the relics are lower than the second ones, i.e. relic galaxies used to be a factor of 2 closer to the cluster centres.

5.2 The location of relic galaxies in the observed catalogue

We now shift our attention to the observational catalogue, and enquire on the abundance and environmental density distribution of relic galaxies. Out of the 41 716 massive galaxies in the catalogue, we find 463 galaxies classified as relics according to the criteria described in Section 3.1. The global relic fraction is therefore 1.11 ± 0.05 per cent. With respect to the normal-sized galaxies that we will use as reference, we find 2086 objects (5.0 per cent of the sample by definition), 1390 of them being early-type galaxies (3.3 per cent).

In Fig. 5 we show the distribution of environmental density for all massive galaxies from the observational catalogue defined in Section 3. Densities range from 0 to 72×10^{10} M$_\odot$ Mpc^{-3}. We note that this range is smaller than that found in simulated relics, which reaches values up to $\rho \lesssim 300 \times 10^{10}$ M$_\odot$ Mpc^{-3} (cf. Fig. 2). The main reason for this difference is the fingers-of-god effect, which was already expected from the reasons exposed when we presented our procedure to estimate the environmental density in Section 4. In addition, the large difference between the volumes of observational (0.011 Gpc^3) and numerical (0.358 Gpc^3) catalogues contributes to the difference in maximum densities. Also contributing must be the spectroscopic redshift incompleteness of the SDSS: the SDSS

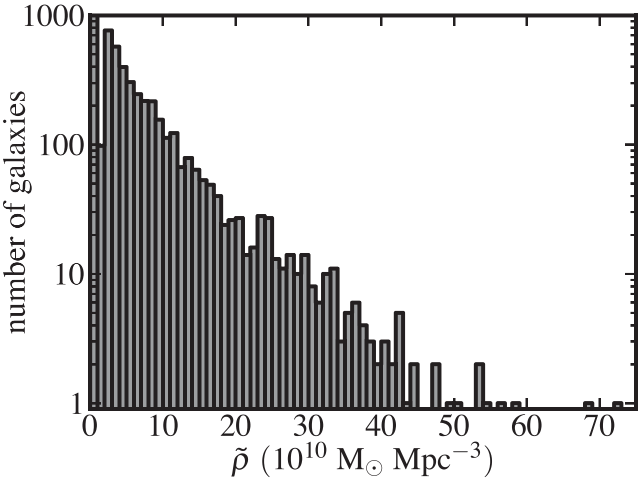

Figure 5. From the observational catalogue, distribution of the environmental density of the massive galaxies. The bin size is $10^{10}\,\mathrm{M_\odot\,Mpc^{-3}}$. The first bin has been cut in this figure, but it contains 37 847 objects and corresponds to the galaxies without neighbours in our sample.

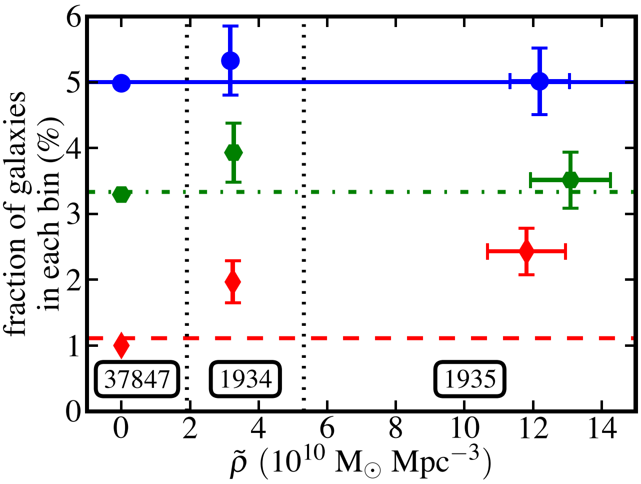

Figure 6. From the observational catalogue, fraction of normal-sized galaxies (blue circles), normal-sized early-type galaxies (green hexagons) and relics (red diamonds) in each environmental-density bin for the subsample. Horizontal blue solid, green dash–dotted and red dashed solid lines show the global fractions of galaxies (i.e. those computed neglecting any $\tilde{\rho}$ binning) which are normal-sized galaxies, normal-sized early-type galaxies and relics, respectively. Vertical black dotted lines show the limits used for binning in the $\tilde{\rho}$ axis, while the numbers within boxes indicate the number of galaxies of the whole sample which belong to each $\tilde{\rho}$ bin. The error bars with similar sizes to the symbol sizes were omitted for clarity.

spectroscopic catalogue is claimed to be ∼99-per-cent complete down to $r \sim 17.77$ mag (Strauss et al. 2002). This will turn out into having not only a smaller number of massive galaxies in the real catalogues but also an artificially smaller environmental density around them, especially in the densest regions.

Fig. 6 shows the fraction of normal-sized galaxies (blue circles), normal-sized early-type galaxies (green hexagons) and relics (red diamonds) in three $\tilde{\rho}$ bins. The first bin contains 37 847 isolated galaxies of our sample (i.e. those with $\tilde{\rho} = 0$), while the other two bins were chosen to contain a similar number of objects (1934 and 1935 galaxies). The limits between these $\tilde{\rho}$ bins are indicated with vertical dotted lines in the figure. Horizontal lines are used to show the fraction of each type of galaxy without considering any $\tilde{\rho}$ binning (in particular, solid blue/green dash–dotted/red dotted line corresponds to the fraction of normal-sized/normal-sized early-type/relic galaxies). Fig. 6 reveals that the fraction of relic galaxies is a monotonic increasing function of the environmental density. In contrast, galaxies with average sizes in the stellar mass–size relationship are equally distributed as a function of the environmental density, even when we focus only on normal-sized early-type galaxies. The increasing trend shown by the relic galaxies in Fig. 6 would be probably more accentuated if SDSS were not affected by incompleteness. The reason is that this incompleteness is more important in the centres of the galaxy clusters due to fibre collision problems (e.g. Guo, Zehavi & Zheng 2012).

The trend shown by Fig. 6 obviously depends on the size R of the fixed-aperture sphere considered in the definition of the environmental density. In this work we have considered $R = 0.5$ kpc. We checked that for radii bigger than 2 Mpc the trend disappears, while it is weaker (but still present) for 1 Mpc. As the size of the sphere for characterizing the environmental density increases our ability to describe the local conditions also decreases. Consequently, we can conclude that the physical conditions for maintaining the galaxies in their initial (relic) configuration are linked with the local (i.e. sub-cluster) scales.

6 DISCUSSION

Both the simulation and the observational data compiled in this work lead to the same conclusion: massive ($M_\star > 10^{10}\,\mathrm{M_\odot}$) relic galaxies can be found in all kind of environments; however, their relative fraction increases with the environmental density. According to the simulations the difference in the relative fraction of relic galaxies in clusters compared to the field can be as high as 4.6. The results that we find in this work suggest that the local environment plays a major role in determining when a massive galaxy formed at $z \gtrsim 2$ is not going to evolve much since its formation. It is particularly relevant for this discussion that, in the simulations, the location of relic galaxies in clusters peaks towards the central parts. The central regions of clusters are also expected to form and virialize early, indicating that the mechanism necessary for the subsequent growth of massive galaxies was slowed down very early on.

The centres of the clusters, particularly the most massive ones, are characterized for having a large velocity dispersion and also a very hot intracluster medium. These conditions prevent an effective mechanism for mass (and size) growth of the galaxies. If the picture drawn here is correct, the right places to find a significant number of massive relic galaxies are on the centre of the clusters. Observationally, to claim the detection of a genuinely relic galaxy is not easy. One has to guarantee that the stellar populations are old throughout the entire structure of the galaxy and this is observationally very demanding. So far, this study has been only conducted in NGC 1277 (Trujillo et al. 2014). Interestingly, this massive and compact galaxy is very closely located towards the centre of the very rich Perseus cluster.

The argument of the previous paragraph focused on how the clusters can help to prevent the galaxy growth and the *rejuvenation* of its stellar population through star formation. Nevertheless, due to hierarchical evolution we could also expect that relics prefer clusters. Since relic galaxies are a subset of galaxies which were formed first (by definition), they have had more time to cluster than galaxies formed later. We have to take into account that even in this scenario, the key to the survival of these relics resides in the large velocity dispersions and the hot intracluster medium.

We would like to point out that the previous interpretation includes our observational findings under the assumption that high-density environments should correspond in their majority to clusters. This is justified as several works (e.g. Haas et al. 2012; Muldrew et al. 2012) have shown that the aperture-based methods are a good proxy for the halo mass and, consequently, for selecting cluster environments.

Comparing our results with previous (observational and numerical) works, we find a nice agreement. As commented in the Introduction (Section 1), Stringer et al. (2015), simulating the dark matter component only, also obtain in the BOLSHOI simulation, an increasingly large number of relic galaxies inhabiting the most massive galaxy clusters. From the observational side, Valentinuzzi et al. (2010) find a large number of massive and compact galaxies in clusters.

The first clues indicating that relic galaxies should be searched in clusters were given by Poggianti et al. (2013). In the nearby Universe, they observed that at least 17 per cent of old (with luminosity ages >9 Gyr) superdense galaxies should be found in clusters. Using the Millenium Simulation, they found 36 per cent of today galaxies with $M_\star > 5 \times 10^{10}\,\mathrm{M}_\odot$ and already passive at $z = 1.6$ are members of clusters. In our work, 12 per cent of the relics from the simulations are part of rich clusters, while in the observations 10 per cent of the relics fall in the highest $\tilde{\rho}$ bin (cf. Fig. 6). Hence, we broadly coincide with Poggianti et al. (2013) in finding a significant fraction of relics in clusters. The quantitative differences between the fractions inferred in the two studies, and between the fractions inferred from observations and from simulations in each study, are to be expected from differences in the adopted definitions of relic and environmental density.

The reason why Trujillo et al. (2009) and Taylor et al. (2010) failed to identify relic galaxies in the SDSS appears to be the more stringent mass ($M_\star > 10^{11}\,\mathrm{M}_\odot$) and compactness constraints used in their search: the galaxy mass function drops steeply at these masses, and catalogues simply have fewer galaxies with $M_\star > 10^{11}\,\mathrm{M}_\odot$. The known spectroscopic incompleteness of SDSS towards the centre of the clusters also contributes to the negative result reported in the above two papers. In fact, when the stellar mass and size of the galaxies are a little bit relaxed, a good number of candidates for being relic galaxies based on the velocity dispersion of the objects is found (Saulder, van den Bosch & Mieske 2015).

It will be worth exploring the environment of relic galaxies at different redshifts. Many recent works have characterized the number density of massive relic galaxies against redshift (Damjanov et al. 2014; Stockton et al. 2014; Hsu, Stockton & Shih 2014; Damjanov et al. 2015a; Tortora et al. 2016). The next step in this direction is to probe whether the relative abundance of those intermediate-redshift relic galaxies is higher in denser environments. The findings in the present paper predict that they will be. A very recent work by Damjanov et al. (2015b) seems to support this prediction.

Could the dependency of the relic fraction with environmental density have been inferred from trends of the stellar mass–size relationship with density? We do not think so. The variation with environment and redshift of the stellar mass–size relationship for early-type/quiescent galaxies has been studied (e.g. Huertas-Company et al. 2013a,b; Cebrián & Trujillo 2014), and their distributions, characterized by parameters such as mean/median or standard deviation, contain insufficient information about the bottom tail of the distributions for characterizing the relic fraction.

We refer in Section 3 to the incompleteness of the SDSS spectroscopic catalogue in nearby massive galaxies studied by Taylor et al. (2010). These authors warn about biases against massive compact galaxies at low redshifts ($z \lesssim 0.05$). Here explore whether the trends outlined in this paper might be the result of such biases. To that effect, we split our sample in two redshift ranges: $z \lesssim 0.05$ where bias effects might be higher, and $z \gtrsim 0.05$ where bias effects are expected to be weaker or non-existent. From the observational volumes of each of the two sub-samples, we estimate that we could be missing approximately 140 galaxies in the low-redshift range due to these biases. The strongest source of bias comes from saturation limits and hence from high surface brightness; it must show very little dependency on environment, and hence there is no reason for expecting that the missed relics show a different environment distribution than the galaxies of our sample. This leads us to conclude that the effects of this bias on the trends of relic fraction with density must be very small. But even if all of the 140 missed galaxies would live in $\tilde{\rho} = 0$ environments, we find that the observational trend of a higher fraction of relics in higher-density environments remains. Additionally, we note that incompleteness in the SDSS spectroscopic catalogue is in fact expected to be higher in clusters due to fibre proximity limits. The effect of such biases would be to dilute, rather than strengthen, the trends found in this paper.

Additionally, we would like to comment that we also checked the dependence of our results on the method that we have used to identify clusters in the simulations. In particular, we have also extracted the list of haloes with stellar masses larger than $10^{14}\,\mathrm{M}_\odot$ using an FoF method in the Millennium simulation. In this case, the number of relic galaxies in the clusters detected by the FoF method is totally comparable to the one found by the method used in this work (described in Section 2.2).

Finally, we would like to mention that the contamination of dusty galaxies in the observational relic sample should be tiny. As it was explained in Section 3.1, due to the unavailability of infra-red data to reject the dusty galaxies, we decided to exclude from our sample the most asymmetric objects in the sky in order to avoid including galaxies which potentially could contain edge-on dusty discs. Applying this filter, we rejected 13 galaxies. Assuming a random orientation of the dusty discs in the sky, and taking into account that the ratio between minor and major axes used in our filter is 0.3, we should have rejected around 70 per cent of the dusty discs. This means that within the considered sample there should be around six face-on dusty discs, which is a small fraction of our sample of relic galaxies. It is also worth noting that this method is conservative, and therefore it overestimates the contamination. Furthermore, we would like to mention that the inclusion of the potentially edge-on dusty galaxies does not change the observational results shown in this work.

7 CONCLUSIONS

The main conclusions of this paper can be summarized as follows.

(i) Cosmological simulations predict that the fraction of present-day relic galaxies with $M_\star > 10^{10}\,\mathrm{M}_\odot$ is only 0.04 per cent. This number is 4.6 higher when the galaxies are located in cluster environments: 0.18 per cent. Moreover, it seems that this fraction could be even larger in the most massive clusters with large velocity dispersions (although the statistical significance of this last result is marginal).

(ii) The distribution of the relic galaxies in the simulation within the clusters is not homogeneous. In fact, they tend to be located a factor of 2 closer to the central parts of the clusters than the other massive galaxies. These very dense regions slow down the physical mechanisms for the mass growth of the galaxies.

(iii) Observationally, in agreement with the simulations, we also find that the fraction of relic galaxies increases as their surrounding densities rise.

These conclusions point in the same direction as previous works: the article by Poggianti et al. (2013), which reported the preference of old (with luminosity ages >9 Gyr) superdense galaxies to inhabit in clusters; and the article by Stringer et al. (2015), which found that dark matter haloes like that of the relic NGC 1277 are substructures of other more massive dark matter haloes.

ACKNOWLEDGEMENTS

The authors are grateful to the referee for his/her useful and constructive review. The authors thank A. Vazdekis and I. Martín-Navarro for their collaboration during the development of this paper. This work has been supported by the Programa Nacional de Astronomía y Astrofísica of the Spanish Ministry of Economy and Competitiveness (under the grants AYA2009-11137, AYA2013-48226-C3-1-P and AYA2013-48226-C3-2-P) and the Generalitat Valenciana (under the grant PROMETEOII/2014/069). The Millennium Simulation data bases used in this paper and the web application providing online access to them were constructed as part of the activities of the German Astrophysical Virtual Observatory. This research made use of ASTROPY, a community-developed core PYTHON package for Astronomy (Astropy Collaboration et al. 2013).

REFERENCES

Abazajian K. N. et al., 2009, ApJS, 182, 543
Astropy Collaboration et al., 2013, A&A, 558, A33
Blanton M. R., Roweis S., 2007, AJ, 133, 734
Blanton M. R. et al., 2005, AJ, 129, 2562
Bryan G. L., Norman M. L., 1998, ApJ, 495, 80
Buitrago F., Trujillo I., Conselice C. J., Bouwens R. J., Dickinson M., Yan H., 2008, ApJ, 687, L61
Calvi R., Poggianti B. M., Vulcani B., 2011, MNRAS, 416, 727
Cebrián M., Trujillo I., 2014, MNRAS, 444, 682
Chabrier G., 2003, PASP, 115, 763
Cooper M. C., Newman J. A., Madgwick D. S., Gerke B. F., Yan R., Davis M., 2005, ApJ, 634, 833
Daddi E. et al., 2005, ApJ, 626, 680
Damjanov I., Hwang H. S., Geller M. J., Chilingarian I., 2014, ApJ, 793, 39
Damjanov I., Geller M. J., Zahid H. J., Hwang H. S., 2015a, ApJ, 806, 158
Damjanov I., Zahid H. J., Geller M. J., Hwang H. S., 2015b, ApJ, 815, 104
Danese L., de Zotti G., di Tullio G., 1980, A&A, 82, 322
Davis M., Efstathiou G., Frenk C. S., White S. D. M., 1985, ApJ, 292, 371
De Lucia G., Blaizot J., 2007, MNRAS, 375, 2
Edge A. C., Stewart G. C., Fabian A. C., 1992, MNRAS, 258, 177
Ferreras I. et al., 2014, MNRAS, 444, 906
Guo H., Zehavi I., Zheng Z., 2012, ApJ, 756, 127
Guo Q., White S., Angulo R. E., Henriques B., Lemson G., Boylan-Kolchin M., Thomas P., Short C., 2013, MNRAS, 428, 1351
Haas M. R., Schaye J., Jeeson-Daniel A., 2012, MNRAS, 419, 2133
Hsu L.-Y., Stockton A., Shih H.-Y., 2014, ApJ, 796, 92
Huertas-Company M. et al., 2013a, MNRAS, 428, 1715
Huertas-Company M., Shankar F., Mei S., Bernardi M., Aguerri J. A. L., Meert A., Vikram V., 2013b, ApJ, 779, 29
Komatsu E. et al., 2011, ApJS, 192, 18
Lemson G., Virgo Consortium the, 2006, preprint (astro-ph/0608019)
Muldrew S. I. et al., 2012, MNRAS, 419, 2670
Naab T., Johansson P. H., Ostriker J. P., 2009, ApJ, 699, L178
Peralta de Arriba L. et al., 2015, MNRAS, 453, 704
Planelles S., Quilis V., 2009, MNRAS, 399, 410
Poggianti B. M. et al., 2013, ApJ, 762, 77
Quilis V., Trujillo I., 2013, ApJ, 773, L8
Ricciardelli E., Vazdekis A., Cenarro A. J., Falcón-Barroso J., 2012, MNRAS, 424, 172
Saulder C., van den Bosch R. C. E., Mieske S., 2015, A&A, 578, A134
Shen S., Mo H. J., White S. D. M., Blanton M. R., Kauffmann G., Voges W., Brinkmann J., Csabai I., 2003, MNRAS, 343, 978
Springel V., White S. D. M., Tormen G., Kauffmann G., 2001, MNRAS, 328, 726
Springel V. et al., 2005, Nature, 435, 629
Stockton A., Shih H.-Y., Larson K., Mann A. W., 2014, ApJ, 780, 134
Strauss M. A. et al., 2002, AJ, 124, 1810
Stringer M., Trujillo I., Dalla Vecchia C., Martinez-Valpuesta I., 2015, MNRAS, 449, 2396
Taylor E. N., Franx M., Glazebrook K., Brinchmann J., van der Wel A., van Dokkum P. G., 2010, ApJ, 720, 723
Tortora C. et al., 2016, MNRAS, 457, 2845
Trujillo I., Conselice C. J., Bundy K., Cooper M. C., Eisenhardt P., Ellis R. S., 2007, MNRAS, 382, 109
Trujillo I., Cenarro A. J., de Lorenzo-Cáceres A., Vazdekis A., de la Rosa I. G., Cava A., 2009, ApJ, 692, L118
Trujillo I., Ferré-Mateu A., Balcells M., Vazdekis A., Sánchez-Blázquez P., 2014, ApJ, 780, L20
Valentinuzzi T. et al., 2010, ApJ, 712, 226
van der Wel A. et al., 2014, ApJ, 788, 28
Varela J., Betancort-Rijo J., Trujillo I., Ricciardelli E., 2012, ApJ, 744, 82
Vazdekis A., Sánchez-Blázquez P., Falcón-Barroso J., Cenarro A. J., Beasley M. A., Cardiel N., Gorgas J., Peletier R. F., 2010, MNRAS, 404, 1639
Vazdekis A., Ricciardelli E., Cenarro A. J., Rivero-González J. G., Díaz-García L. A., Falcón-Barroso J., 2012, MNRAS, 424, 157

This paper has been typeset from a TEX/LATEX file prepared by the author.

6

Conclusions and future work

In this thesis we have reported observational evidence to clarify the origin of the size growth of massive galaxies and some questions which have arisen after this discovery. In particular, we have focused our work on early-type massive galaxies because they are the objects which have experienced the strongest size evolution. Our conclusions, which have already been summarized at the end of the three previous chapters, is revisited in the following (Section 6.1), while future work suggested by this thesis is described in Section 6.2.

6.1 Conclusions

In Chapter 3 (Peralta de Arriba et al. 2014) we analysed the properties of a sample of early-type galaxies with $M_\star \gtrsim 10^{11}$ $\mathrm{M}_\odot$ from redshift 0 up to 2.5, including 11 stacked spectra built by ourselves. Using this sample we learnt that:

- The degree to which the ratio of stellar to dynamical masses is unphysical ($M_\star/M_{\mathrm{dyn}} > 1$) is related to the compactness of the galaxies, not to redshift.

- For most compact galaxies, the mass discrepancy is too large to be caused by the uncertainties in the IMF, arguably the weakest point in the determination of the total mass of a stellar population. Other uncertainties in the stellar mass determination cannot lead to a reconciliation of the two mass estimators either. The disagreement is too large to be explained by a variation in the dark matter fraction. Therefore, either (i) there exists an unknown large *systematic* error in stellar masses linked to galaxy compactness, or (ii) there is a violation of the homology hypothesis in massive compact galaxies.

- When we interpret the $M_\star$–$M_{\rm dyn}$ discrepancy in terms of non-homology, namely as a variation of the coefficient K from the virial theorem (equation 6 of Chapter 3), the value of K reaches up to ~40 for several compact galaxies (eight times greater than the value found by Cappellari et al. 2006). This strong variation in K is well modelled as $K \propto (r_{\rm e}/r_{\rm Shen}(M_\star))^\alpha$ with $\alpha \simeq -0.8$.

- Owing to the dependence of K on $r_{\rm e}$ and $M_\star$, the dynamical mass scales with $\sigma_{\rm e}$ and $r_{\rm e}$ as $M_{\rm dyn} \propto \sigma_{\rm e}^{3.6} r_{\rm e}^{0.35}$, hence departing from homology and the virial theorem-based scaling $M_{\rm dyn} \propto \sigma_{\rm e}^2 r_{\rm e}$. The equation

$$M_{\rm dyn} \sim \left(\frac{\sigma_{\rm e}}{200 \text{ km s}^{-1}}\right)^{3.6} \left(\frac{r_{\rm e}}{3 \text{ kpc}}\right)^{0.35} 2.1 \times 10^{11} \text{ M}_\odot \tag{6.1}$$

  provides an approximation to estimate $M_{\rm dyn}$ for galaxies with $M_\star/M_{\rm dyn} \sim 0.7$, and is a lower limit for galaxies strongly dominated by dark matter (i.e. $M_\star/M_{\rm dyn} < 0.3$).

In Chapter 4 (Peralta de Arriba et al. 2015) we reduced the spectra of six massive compact galaxies observed with the GTC telescope. This allowed us to obtain a sample of galaxies with $M_\star \gtrsim 10^{11}$ M$_\odot$ in a narrow redshift range at $z \approx 1.0$ which covers a wide range of sizes. We studied this sample together with another sample at $z \sim 0$. These two snapshots freed us of potential redshift-dependent systematics in the mass determinations, a potential concern for the sample used in Chapter 3. From Chapter 4 we conclude that:

- Our measurements of velocity dispersions for six massive compact galaxies do not reveal the high values expected from a law $M_\star \propto \sigma_{\rm e}^2 r_{\rm e}$.

- The discrepancy between stellar and dynamical masses computed as $M_{\rm dyn} = K\sigma_{\rm e}^2 r_{\rm e}/G$ with $K = 5.0$ follows the predictions of Chapter 3, i.e. it scales with galaxy compactness. This implies a breakdown of homology.

- For our sample of massive galaxies at $z \sim 1$ which includes our six compact galaxies, we find a relationship between $M_\star$, $\sigma_{\rm e}$ and $r_{\rm e}$ compatible with the alternative scaling law proposed in Chapter 3 (equation 6.1). This result is compatible with a snapshot at $z \sim 0$ with galaxies from SDSS.

Additionally, in Chapter 4 (Peralta de Arriba et al. 2015) we interpreted the information from Chapters 3 and 4 as a constraint on the evolution of massive galaxies. In particular, we showed that:

- The relationship between $M_\star$, σ_e and r_e (that is, the plane described by these three observables) is compatible with numerical studies of the growth of massive ellipticals due to a mixture of minor and major mergers that have a cosmological framework such as that realized by Tapia et al. (2015).
- The numerical simulations of dry mergers from Hilz et al. (2012) also predict a break of homology in the same direction that our stellar mass plane constrains.

In Chapter 5 (Peralta de Arriba et al. 2016) we studied the preferred environment of relic galaxies using a catalogue of nearby galaxies. In particular, we defined observational relics as $M_\star \gtrsim 10^{10}$ $\mathrm{M}_\odot$ early-type galaxies with colours compatible with single-stellar population ages older than 10 Gyr, and which occupy the bottom 5-percentile in the stellar mass–size distribution. Our conclusions from this chapter are that:

- The fraction of relic galaxies increases as their surrounding densities rise, i.e. they prefer dense environments.
- Our observational results show the same trend as that seen in cosmological simulations, which predict a higher fraction of relics in denser environments. Furthermore, simulations also show a higher fraction of galaxies in clusters than in the field, and a trend of relics to be in the central parts of the clusters.
- Our observational results and those from the cosmological simulation which we used to compare, point in the same direction as previous works: the article by Poggianti et al. (2013a), which reported the preference of old (with luminosity ages >9 Gyr) superdense galaxies to inhabit in clusters; and the article by Stringer et al. (2015), which found that dark matter haloes like that of the relic NGC 1277 (Trujillo et al. 2014) are substructures of other more massive dark matter haloes.

Finally, we would like to finish by emphasising, as a global conclusion, that all the results in this thesis are compatible with the scenario where massive galaxies have growth through mergers (e.g. Naab et al. 2007, 2009).

6.2 Future work

The work presented in this thesis suggests various avenues of future research.

Concerning the discrepancy between dynamical and stellar masses in massive compact galaxies (Chapter 3), the natural next step is to obtain independent mass determinations for compact galaxies. Deep two-dimensional spectroscopy on nearby massive compact galaxies could be used to develop Jeans or Schwarzschild modelling for estimating dynamical masses, such as was done for normal massive ellipticals by the SAURON and ATLAS^{3D} projects (Cappellari et al. 2006, 2013). A complementary, independent approach would be to compare with mass estimates derived using gravitational lensing techniques.

Given the small dark matter fractions expected in the cores of massive ellipticals, dynamical mass determinations may be used to provide interesting constraints on stellar population modelling, in particular on the shape of the IMF.

In Chapter 4 we showed that the tilt of the stellar mass plane (and consequently the discrepancy between mass estimators) could have been anticipated from the results of dry-merger simulations. This tilt could be detected by having galaxies which depart from the nearby stellar mass–size scaling relationship. Nevertheless, the accuracy for estimating such a tilt is affected by the mixture of data from different samples. In addition, in our work we could not take advantage of the recent observational techniques for constraining the IMF (e.g. Martín-Navarro et al. 2015a,b,c,d). Therefore, to build up a new homogeneous sample covering a wide range of compactness with observational information for the initial mass function, would provide a powerful avenue for constraining the evolutionary mechanisms.

In Chapter 4 we mentioned the difficulty of comparing our observations with puffing-up simulations. The reason was that, in all of the publications where puffing-up evolution is studied, results are given in terms of quantities that cannot be directly observed. It remains a pending task for simulators to report results of the puffing-up mechanism in terms of stellar mass, effective radius and velocity dispersion within this radius (even if just to be able to rule out this mechanism, which we believe provides an unlikely explanation to size evolution in massive ellipticals).

In Chapter 5 we showed the preference of potential relic galaxies to inhabit in high-density environments. Moreover, simulations suggest to look for them in cluster centres. Therefore, we propose to continue the hunt for relic galaxies (started by Trujillo et al. 2014) using our sample of galaxies which live in high-density environments, and rejecting the objects far from cluster centres. This strategy will optimize our probabilities for finding galaxies that satisfy the ‘relic’ requirements along their whole structures. Additional observational tests of the relic hypothesis include searching for the expected subtle differences in stellar population signatures between compact and non-compact massive ellipticals in the local universe, and to explore and model population gradient signatures in these two types of galaxies.

Bibliography

Abazajian K. N. et al., 2009, ApJS, 182, 543

Abell G. O., 1958, ApJS, 3, 211

Abell G. O., Corwin Jr. H. G., Olowin R. P., 1989, ApJS, 70, 1

Alpher R. A., Bethe H., Gamow G., 1948, Physical Review, 73, 803

Astropy Collaboration et al., 2013, A&A, 558, A33

Babcock H. W., 1939, Lick Observatory Bulletin, 19, 41

Barro G. et al., 2011a, ApJS, 193, 13

Barro G. et al., 2011b, ApJS, 193, 30

Barro G. et al., 2014, ApJ, 795, 145

Belli S., Newman A. B., Ellis R. S., 2014, ApJ, 783, 117

Bertin G., Ciotti L., Del Principe M., 2002, A&A, 386, 149

Bezanson R., van Dokkum P., van de Sande J., Franx M., Kriek M., 2013, ApJ, 764, L8

Binney J., Tremaine S., 1987, Galactic dynamics. Princeton Univ. Press, Princeton

Blakeslee J. P. et al., 2006, ApJ, 644, 30

Blanton M. R., Roweis S., 2007, AJ, 133, 734

Blanton M. R. et al., 2005, AJ, 129, 2562

Bower R. G., Benson A. J., Crain R. A., 2012, MNRAS, 422, 2816

Bryan G. L., Norman M. L., 1998, ApJ, 495, 80

Buitrago F., Trujillo I., Conselice C. J., Bouwens R. J., Dickinson M., Yan H., 2008, ApJ, 687, L61

Buitrago F., Trujillo I., Conselice C. J., Häußler B., 2013, MNRAS, 428, 1460

Buitrago F., Conselice C. J., Epinat B., Bedregal A. G., Grützbauch R., Weiner B. J., 2014, MNRAS, 439, 1494

Bundy K. et al., 2006, ApJ, 651, 120

Bundy K., Fukugita M., Ellis R. S., Targett T. A., Belli S., Kodama T., 2009, ApJ, 697, 1369

Calvi R., Poggianti B. M., Vulcani B., 2011, MNRAS, 416, 727

Calzetti D., Armus L., Bohlin R. C., Kinney A. L., Koornneef J., Storchi-Bergmann T., 2000, ApJ, 533, 682

Calzetti D. et al., 2007, ApJ, 666, 870

Cappellari M., Emsellem E., 2004, PASP, 116, 138

Cappellari M. et al., 2006, MNRAS, 366, 1126

Cappellari M. et al., 2009, ApJ, 704, L34

Cappellari M. et al., 2012, Nature, 484, 485

Cappellari M. et al., 2013, MNRAS, 432, 1709

Cardiel N., 1999, PhD thesis, Univ. Complutense de Madrid, Spain

Cebrián M., Trujillo I., 2014, MNRAS, 444, 682

Cenarro A. J., Trujillo I., 2009, ApJ, 696, L43

Chabrier G., 2003, PASP, 115, 763

Cimatti A. et al., 2008, A&A, 482, 21

Coil A. L., Newman J. A., Kaiser N., Davis M., Ma C.-P., Kocevski D. D., Koo D. C., 2004, ApJ, 617, 765

Conroy C., van Dokkum P. G., 2012, ApJ, 760, 71

Conroy C., Gunn J. E., White M., 2009, ApJ, 699, 486

Conselice C. J. et al., 2007, MNRAS, 381, 962

Cooper M. C., Newman J. A., Madgwick D. S., Gerke B. F., Yan R., Davis M., 2005, ApJ, 634, 833

Courteau S. et al., 2014, Reviews of Modern Physics, 86, 47

Cowie L. L., Songaila A., Hu E. M., Cohen J. G., 1996, AJ, 112, 839

Daddi E. et al., 2005, ApJ, 626, 680

Damjanov I. et al., 2009, ApJ, 695, 101

Damjanov I., Hwang H. S., Geller M. J., Chilingarian I., 2014, ApJ, 793, 39

Damjanov I., Geller M. J., Zahid H. J., Hwang H. S., 2015a, ApJ, 806, 158

Damjanov I., Zahid H. J., Geller M. J., Hwang H. S., 2015b, ApJ, 815, 104

Danese L., de Zotti G., di Tullio G., 1980, A&A, 82, 322

Davis M., Efstathiou G., Frenk C. S., White S. D. M., 1985, ApJ, 292, 371

Davis M. et al., 2003, Proc. SPIE, 4834, 161

Davis M. et al., 2007, ApJ, 660, L1

de Bruyne V., Vauterin P., de Rijcke S., Dejonghe H., 2003, MNRAS, 339, 215

De Lucia G., Blaizot J., 2007, MNRAS, 375, 2

de Vaucouleurs G., 1948, Annales d'Astrophysique, 11, 247

de Vaucouleurs G., 1953, MNRAS, 113, 134

de Vaucouleurs G., 1959a, Handbuch der Physik, 53, 275

de Vaucouleurs G., 1959b, Handbuch der Physik, 53, 311

de Vaucouleurs G., 1977, in Tinsley B. M., Larson R. B., Gehret D. C., eds, Evolution of Galaxies and Stellar Populations. Yale University Observatory, New Haven, p. 43

Dekel A., Ostriker J. P., eds, 1999, Formation of Structure in the Universe. Cambridge Univ. Press, Cambridge

di Serego Alighieri S. et al., 2005, A&A, 442, 125

Djorgovski S., de Carvalho R., Han M.-S., 1988, in Pritchet C. J., van den Bergh S., eds, ASP Conf. Ser. Vol. 4, The extragalactic distance scale. Astron. Soc. Pac., San Francisco, p. 329

Donas J., Deharveng J. M., 1984, A&A, 140, 325

Doppler C., Studnica F. J., 1903, Ueber das farbige licht der doppelsterne und einiger anderer gestirne des himmels. K. Bohm gesellschaft der wissenschaften, Prag

Dressler A., 1980, ApJ, 236, 351

Drory N., Bender R., Hopp U., 2004, ApJ, 616, L103

Eddington A. S., 1926, The Internal Constitution of the Stars. Cambridge Univ. Press, Cambridge

Edge A. C., Stewart G. C., Fabian A. C., 1992, MNRAS, 258, 177

Eggen O. J., Lynden-Bell D., Sandage A. R., 1962, ApJ, 136, 748

Eisenstein D. J. et al., 2005, ApJ, 633, 560

Emsellem E. et al., 2004, MNRAS, 352, 721

Emsellem E. et al., 2007, MNRAS, 379, 401

Faber S. M. et al., 2003, Proc. SPIE, 4841, 1657

Falcón-Barroso J. et al., 2011, MNRAS, 417, 1787

Fan L., Lapi A., De Zotti G., Danese L., 2008, ApJ, 689, L101

Fernández Lorenzo M., Cepa J., Bongiovanni A., Pérez García A. M., Ederoclite A., Lara-López M. A., Pović M., Sánchez-Portal M., 2011, A&A, 526, A72

Ferré-Mateu A., Vazdekis A., Trujillo I., Sánchez-Blázquez P., Ricciardelli E., de la Rosa I. G., 2012, MNRAS, 423, 632

Ferreras I., La Barbera F., de la Rosa I. G., Vazdekis A., de Carvalho R. R., Falcón-Barroso J., Ricciardelli E., 2013, MNRAS, 429, L15

Ferreras I. et al., 2014, MNRAS, 444, 906

Fioc M., Rocca-Volmerange B., 1997, A&A, 326, 950

Fontanot F., De Lucia G., Monaco P., Somerville R. S., Santini P., 2009, MNRAS, 397, 1776

Fraser C. W., 1972, The Observatory, 92, 51

Gallagher J. S., Hunter D. A., Bushouse H., 1989, AJ, 97, 700

Gamow G., 1948a, Physical Review, 74, 505

Gamow G., 1948b, Nature, 162, 680

Gavazzi R., Treu T., Rhodes J. D., Koopmans L. V. E., Bolton A. S., Burles S., Massey R. J., Moustakas L. A., 2007, ApJ, 667, 176

Gebhardt K. et al., 2003, ApJ, 597, 239

Guo H., Zehavi I., Zheng Z., 2012, ApJ, 756, 127

Guo Q., White S., Angulo R. E., Henriques B., Lemson G., Boylan-Kolchin M., Thomas P., Short C., 2013, MNRAS, 428, 1351

Haas M. R., Schaye J., Jeeson-Daniel A., 2012, MNRAS, 419, 2133

Hilz M., Naab T., Ostriker J. P., Thomas J., Burkert A., Jesseit R., 2012, MNRAS, 425, 3119

Hopkins P. F., Bundy K., Murray N., Quataert E., Lauer T. R., Ma C.-P., 2009, MNRAS, 398, 898

Hopkins P. F., Bundy K., Hernquist L., Wuyts S., Cox T. J., 2010, MNRAS, 401, 1099

Hsu L.-Y., Stockton A., Shih H.-Y., 2014, ApJ, 796, 92

Hubble E. P., 1925, Popular Astronomy, 33, 252

Hubble E. P., 1926, ApJ, 64, 321

Hubble E. P., 1930, ApJ, 71, 231

Hubble E. P., 1936, Realm of the Nebulae. Yale Univ. Press, New Haven

Huertas-Company M. et al., 2013a, MNRAS, 428, 1715

Huertas-Company M., Shankar F., Mei S., Bernardi M., Aguerri J. A. L., Meert A., Vikram V., 2013b, ApJ, 779, 29

Jorgensen I., Franx M., Kjaergaard P., 1995, MNRAS, 276, 1341

Kauffmann G. et al., 2003, MNRAS, 341, 33

Kaviraj S., Peirani S., Khochfar S., Silk J., Kay S., 2009, MNRAS, 394, 1713

Kelson D. D., 2003, PASP, 115, 688

Kennicutt Jr. R. C., 1979, ApJ, 228, 394

Kennicutt Jr. R. C., 1983, ApJ, 272, 54

Khochfar S., Silk J., 2006, ApJ, 648, L21

Komatsu E. et al., 2011, ApJS, 192, 18

Kroupa P., 2002, Science, 295, 82

Le Borgne D., Rocca-Volmerange B., Prugniel P., Lançon A., Fioc M., Soubiran C., 2004, A&A, 425, 881

Lemson G., Virgo Consortium the, 2006, preprint (astro-ph/0608019)

Longhetti M., Saracco P., 2009, MNRAS, 394, 774

Longhetti M. et al., 2007, MNRAS, 374, 614

López-Sanjuan C., Balcells M., Pérez-González P. G., Barro G., García-Dabó C. E., Gallego J., Zamorano J., 2010, ApJ, 710, 1170

Markwardt C. B., 2009, in Bohlender D. A., Durand D., Dowler P., eds, ASP Conf. Ser. Vol. 411, Astronomical Data Analysis Software and Systems XVIII. Astron. Soc. Pac., San Francisco, p. 251

Martín-Navarro I., Barbera F. L., Vazdekis A., Falcón-Barroso J., Ferreras I., 2015a, MNRAS, 447, 1033

Martín-Navarro I., La Barbera F., Vazdekis A., Ferré-Mateu A., Trujillo I., Beasley M. A., 2015b, MNRAS, 451, 1081

Martín-Navarro I. et al., 2015c, ApJ, 798, L4

Martín-Navarro I. et al., 2015d, ApJ, 806, L31

Martinez-Manso J. et al., 2011, ApJ, 738, L22 (MM11)

Mayall N. U., 1958, in Roman N. G., ed., IAU Symposium Vol. 5, Comparison of the Large-Scale Structure of the Galactic System with that of Other Stellar Systems. Cambridge Univ. Press, Cambridge, p. 23

Muldrew S. I. et al., 2012, MNRAS, 419, 2670

Muzzin A., Marchesini D., van Dokkum P. G., Labbé I., Kriek M., Franx M., 2009, ApJ, 701, 1839

Naab T., Johansson P. H., Ostriker J. P., Efstathiou G., 2007, ApJ, 658, 710

Naab T., Johansson P. H., Ostriker J. P., 2009, ApJ, 699, L178

Newman A. B., Ellis R. S., Treu T., Bundy K., 2010, ApJ, 717, L103

Newman J. A. et al., 2013, ApJS, 208, 5

Onodera M. et al., 2012, ApJ, 755, 26

Patterson F. S., 1940, Harvard College Observatory Bulletin, 914, 9

Peletier R. F., Davies R. L., Illingworth G. D., Davis L. E., Cawson M., 1990, AJ, 100, 1091

Penzias A. A., Wilson R. W., 1965, ApJ, 142, 419

Peralta de Arriba L., Balcells M., Falcón-Barroso J., Trujillo I., 2014, MNRAS, 440, 1634 (PdA14)

Peralta de Arriba L. et al., 2015, MNRAS, 453, 704

Peralta de Arriba L., Quilis V., Trujillo I., Cebrián M., Balcells M., 2016, MNRAS, 461, 156

Pérez-González P. G. et al., 2008, ApJ, 675, 234

Perlmutter S. et al., 1999, ApJ, 517, 565

Petrosian V., 1976, ApJ, 209, L1

Planelles S., Quilis V., 2009, MNRAS, 399, 410

Poggianti B. M. et al., 2013a, ApJ, 762, 77

Poggianti B. M., Moretti A., Calvi R., D'Onofrio M., Valentinuzzi T., Fritz J., Renzini A., 2013b, ApJ, 777, 125

Prieto M., Campos-Aguilar A., Garcia C., 1989, Ap&SS, 157, 321

Prugniel P., Soubiran C., Koleva M., Le Borgne D., 2007, preprint (astro-ph/0703658)

Quilis V., Trujillo I., 2013, ApJ, 773, L8

Ragone-Figueroa C., Granato G. L., 2011, MNRAS, 414, 3690

Ravindranath S. et al., 2004, ApJ, 604, L9

Renzini A., 2006, ARA&A, 44, 141

Reynolds J. H., 1913, MNRAS, 74, 132

Ricciardelli E., Vazdekis A., Cenarro A. J., Falcón-Barroso J., 2012, MNRAS, 424, 172

Riess A. G. et al., 1998, AJ, 116, 1009

Rubin V. C., Ford Jr. W. K., 1970, ApJ, 159, 379

Ruiz P., Trujillo I., Mármol-Queraltó E., 2014, MNRAS, 442, 347

Salaris M., Cassisi S., 2006, Evolution of Stars and Stellar Populations. Wiley, Chichester

Salpeter E. E., 1955, ApJ, 121, 161

Satoh C., 1980, PASJ, 32, 41

Saulder C., van den Bosch R. C. E., Mieske S., 2015, A&A, 578, A134

Schiavon R. P. et al., 2006, ApJ, 651, L93

Schwarzschild M., 1979, ApJ, 232, 236

Sérsic J. L., 1963, Boletín de la Asociación Argentina de Astronomía, 6, 41

Sérsic J. L., 1968, Atlas de galaxias australes. Observatorio Astronómico, Córdoba

Shankar F., Marulli F., Bernardi M., Dai X., Hyde J. B., Sheth R. K., 2010, MNRAS, 403, 117

Shapley H., Curtis H. D., 1921, Bulletin of the National Research Council, 2, 171

Shen S., Mo H. J., White S. D. M., Blanton M. R., Kauffmann G., Voges W., Brinkmann J., Csabai I., 2003, MNRAS, 343, 978

Smoot G. F. et al., 1992, ApJ, 396, L1

Springel V., White S. D. M., Tormen G., Kauffmann G., 2001, MNRAS, 328, 726

Springel V. et al., 2005, Nature, 435, 629

Stark A. A., Gammie C. F., Wilson R. W., Bally J., Linke R. A., Heiles C., Hurwitz M., 1992, ApJS, 79, 77

Stevenson C. C., 1994, MNRAS, 267, 904

Stockton A., Shih H.-Y., Larson K., 2010, ApJ, 709, L58

Stockton A., Shih H.-Y., Larson K., Mann A. W., 2014, ApJ, 780, 134

Strauss M. A. et al., 2002, AJ, 124, 1810

Stringer M., Trujillo I., Dalla Vecchia C., Martinez-Valpuesta I., 2015, MNRAS, 449, 2396

Tapia T. et al., 2015, submitted

Taylor E. N., Franx M., Glazebrook K., Brinchmann J., van der Wel A., van Dokkum P. G., 2010a, ApJ, 720, 723

Taylor E. N., Franx M., Brinchmann J., van der Wel A., van Dokkum P. G., 2010b, ApJ, 722, 1

Toft S. et al., 2007, ApJ, 671, 285

Toft S., Gallazzi A., Zirm A., Wold M., Zibetti S., Grillo C., Man A., 2012, ApJ, 754, 3

Toloba E. et al., 2015, ApJ, 799, 172

Tortora C. et al., 2016, MNRAS, 457, 2845

Treu T., Auger M. W., Koopmans L. V. E., Gavazzi R., Marshall P. J., Bolton A. S., 2010, ApJ, 709, 1195

Trujillo I., Burkert A., Bell E. F., 2004, ApJ, 600, L39

Trujillo I. et al., 2006, MNRAS, 373, L36

Trujillo I., Conselice C. J., Bundy K., Cooper M. C., Eisenhardt P., Ellis R. S., 2007, MNRAS, 382, 109 (T07)

Trujillo I., Cenarro A. J., de Lorenzo-Cáceres A., Vazdekis A., de la Rosa I. G., Cava A., 2009, ApJ, 692, L118

Trujillo I., Ferreras I., de La Rosa I. G., 2011, MNRAS, 415, 3903

Trujillo I., Ferré-Mateu A., Balcells M., Vazdekis A., Sánchez-Blázquez P., 2014, ApJ, 780, L20

Valdes F., Gupta R., Rose J. A., Singh H. P., Bell D. J., 2004, ApJS, 152, 251

Valentinuzzi T. et al., 2010, ApJ, 712, 226

Valls-Gabaud D., 2006, in Alimi J.-M., Füzfa A., eds, American Institute of Physics Conference Series Vol. 861, Albert Einstein Century International Conference. American Institute of Physics, New York, p. 1163

van de Sande J. et al., 2013, ApJ, 771, 85

van den Bosch R. C. E., Gebhardt K., Gültekin K., van de Ven G., van der Wel A., Walsh J. L., 2012, Nature, 491, 729

van der Marel R. P., Franx M., 1993, ApJ, 407, 525

van der Wel A., Franx M., van Dokkum P. G., Rix H.-W., Illingworth G. D., Rosati P., 2005, ApJ, 631, 145

van der Wel A., Holden B. P., Zirm A. W., Franx M., Rettura A., Illingworth G. D., Ford H. C., 2008, ApJ, 688, 48

van der Wel A. et al., 2012, ApJS, 203, 24

van der Wel A. et al., 2014, ApJ, 788, 28

van Dokkum P. G., Kriek M., Franx M., 2009, Nature, 460, 717

Varela J., Betancort-Rijo J., Trujillo I., Ricciardelli E., 2012, ApJ, 744, 82

Vazdekis A., Sánchez-Blázquez P., Falcón-Barroso J., Cenarro A. J., Beasley M. A., Cardiel N., Gorgas J., Peletier R. F., 2010, MNRAS, 404, 1639

Vazdekis A., Ricciardelli E., Cenarro A. J., Rivero-González J. G., Díaz-García L. A., Falcón-Barroso J., 2012, MNRAS, 424, 157

Vikhlinin A., Kravtsov A., Forman W., Jones C., Markevitch M., Murray S. S., Van Speybroeck L., 2006, ApJ, 640, 691

Visvanathan N., Sandage A., 1977, ApJ, 216, 214

Will C. M., 1988, American Journal of Physics, 56, 413

York D. G. et al., 2000, AJ, 120, 1579

Zirm A. W. et al., 2007, ApJ, 656, 66

Zwicky F., 1933, Helvetica Physica Acta, 6, 110

Agradecimientos (Acknowledgments in Spanish)

> Las estrellas para quien las trabaja.
>
> JUAN CARLOS MESTRE

Esta tesis ha sido fruto del trabajo realizado por mis directores, por los autores de los artículos que en ella aparecen, por las personas que se nombran en los agradecimientos de éstos y por muchos compañeros que me han ayudado en proyectos que no llegaron a buen término (M. Ramón-Pérez, J. Zaragoza-Cardiel, B. A. Laken y los que seguro que me dejo en el tintero). A todos ellos espero haberles recompensado por sus esfuerzos, o en su defecto, haberles mostrado mi agradecimiento con algo más que una frase al final de este documento.

Pero en lugar de repetir aquí sus nombres (si queréis saber quienes son, ¡ojead la tesis!), me gustaría ser breve y dedicar este espacio para reconocer la extremada generosidad que algunas personas tuvieron en los momentos que había que achicar agua cuando el barco se hundía: Ignacio Martín Navarro, Jesús Falcón Barroso, Vicent Quilis, María Cebrián, Michael A. Beasley, Fiona Charlton y Laura Toribio San Cipriano.

¡Muchas gracias a todos!

Luis Peralta de Arriba
Salamanca, julio de 2016